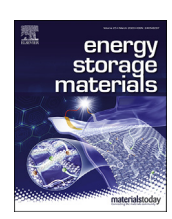
ELSEVIER

Contents lists available at ScienceDirect

Energy Storage Materials

journal homepage: www.elsevier.com/locate/ensm



Dual-ion batteries: The emerging alternative rechargeable batteries



Yiming Sui ^{a,1}, Chaofeng Liu ^{a,1}, Robert C. Masse ^a, Zachary G. Neale ^a, Muhammad Atif ^b, Mohamad AlSalhi ^b, Guozhong Cao ^{a,*}

- ^a Department of Materials Science and Engineering, University of Washington, Seattle, WA, 98195, USA
- b Physics and Astronomy Department, College of Science, King Saud University, Riyadh, 11451, Saudi Arabia

ARTICLE INFO

Keywords: Dual-ion batteries Anion intercalation Graphite Electrodes Electrolytes Energy storage

ABSTRACT

Development of energy storage technologies is thriving because of the increasing demand for renewable and sustainable energy sources. Although lithium-ion batteries (LIBs) are already mature technologies that play important roles in modern society, the scarcity of cobalt and lithium sources in the Earth's crust limits their future deployment at the scale required to supplant fossil fuels. Dual-ion batteries (DIBs) based on a different combination of chemistries are emerging-energy storage-systems. Conventional DIBs apply the graphite as both electrodes and a combination of organic solvents and lithium salts as electrolytes. This configuration is fascinating because of its high working potential (>4.5 V vs. Li/Li⁺), potentially high energy density, high safety and low cost. But it also accompanies some negative issues like limited capacity of intercalation-type graphite electrodes, cyclic stability endangered by large anions intercalation and solvent co-intercalation and electrolyte decomposition under high voltage. This review aims at pointing out the challenges in the current work on DIBs with subcategories of positive and negative electrodes (cathode and anode), and electrolytes and comparing the strategies for improvements with better fundamental understanding of DIBs.

1. Introduction

1.1. Background

Fossil fuel (e.g. coal, natural gas) combustion has supported the development of modern civilization, but the environmental concerns, especially air pollution and greenhouse gas emissions, have given rise to anxieties among governments and scientific organizations (Fig. 1a) [1,2]. The International Energy Outlook (IEO) released by the U.S. Energy Information Administration (EIA) in 2017 forecasts that global energy consumption will rise to 663 quadrillion British thermal units (Btu) by 2030 and then to 736 quadrillion Btu by 2040 (Fig. 1b) [3]. At the same time, the world population is predicted to grow to 9.7 billion by 2050 and then to 11.2 billion by 2080 (Fig. 1c) [4], which will intensify the energy demand. With the depletion of non-renewable fossil fuels, harvesting energy from eco-friendly sources like sunlight, wind, biomass, and mechanical resistance becomes an important and fruitful topic of on-going research [5-18]. Since renewable resources like wind and solar are intermittent energy sources, they must be coupled with energy storage systems to balance the energy use. Additionally, the rapid development of electric vehicles and consumer electronics also requires energy storage systems to provide energy over long driving distances or long operating time. Because of these surging demands, energy storage systems have been constantly improving over the past decades, particularly rechargeable batteries [19–40]. The lithium-ion batteries (abbreviated as LIBs) breakthrough by Sony Corp. in 1991 pushed energy storage technology forward and reshaped the market for portable electronics, and electric vehicles, power tools as well [41–46].

LIBs store energy in electrode materials by reversibly converting chemical and electrical energy. Positive and negative electrode materials are energy carriers or energy storage hosts, in which lithium ions and electrons are inserted in their crystal lattices and electronic orbitals [47, 48]. Most important advantages of the lithium ions are i) lowest reduction potential (-3.04 V vs. Standard Hydrogen Electrode, SHE) and ii) relatively small ionic radius (76 pm) among metal ions, and iii) lightest metal in the periodic table (6.94 g/mol), which enable LIBs to possess high cell voltage by applying low-working-potential negative electrodes like graphite, high capacity, long cyclic stability and high energy/power density [46,48–57]. Notably, LIBs with intercalation-type positive electrodes and graphite negative electrodes are still the most commonly used

E-mail address: gzcao@uw.edu (G. Cao).

^{*} Corresponding author.

¹ Y. Sui and C. Liu contribute equally.

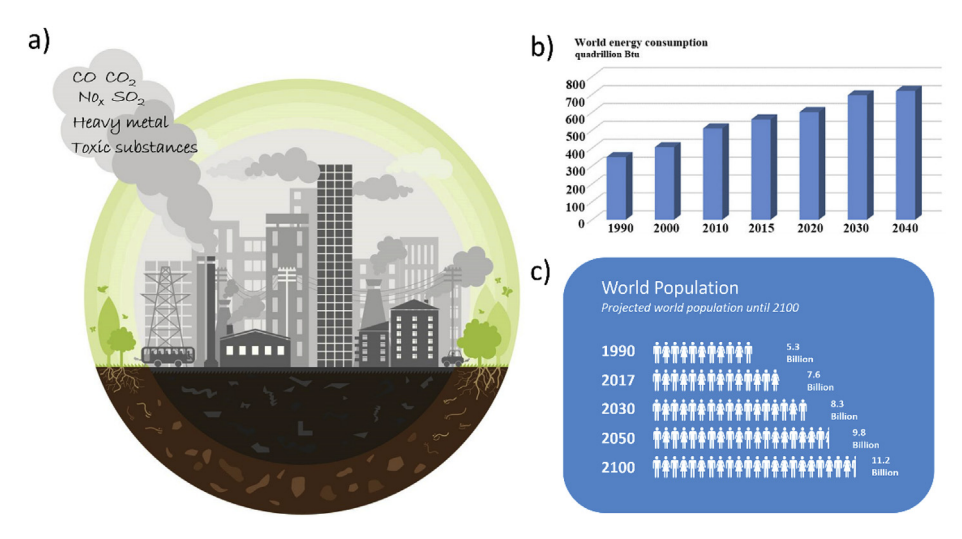


Fig. 1. a) Schematic illustration of the air pollution brought by combusting the fossil fuels (https://helpsavenature.com/lists-of-environmental-problems). b) The prediction of global energy consumption [3] and c) world population growth trend (https://ourworldindata.org/world-population-growth).

commercial rechargeable batteries even 27 years after its first development (Fig. 2a) [50,58]. However, those traditional host materials powered by intercalation mechanism commonly have limited active crystallographic sites for storing charge carriers, in turn, restricting their specific capacity and power density. In addition, transition metals in the positive electrode materials of LIBs account for a large fraction of the overall battery cost [59–62]. Metal oxide positive electrodes are also susceptible to release oxygen and undergo irreversible phase changes when overcharged [63–65]. Therefore, their working capacity is restricted (to barely 30% of theoretical value) for safety and performance reasons [66,67]. Under the circumstance, a series of new energy storage systems (e.g. lithium-metal batteries [68,69], DIBs [70–74], high-voltage

LIBs [75,76], lithium-oxygen batteries [77,78], lithium-sulfur batteries [78,79], see Fig. 2), partially working with new chemistries beyond conventional LIBs, are proposed and developed in the past decades to meet the market demands on high power density. But they share the same problem of inferior reversibility/stability due to the instabilities of host materials during redox reactions and some negative side reactions happened on the electrolyte/electrode interface [78,80]. Among them, DIBs are considered promising alternative rechargeable batteries as they avoid all above shortcomings of the conventional LIBs [81]. In contrast to conventional rocking-chair batteries, DIBs support the simultaneous intercalation of anions into the positive electrode and cations into the negative electrode upon charging, and in the discharging process, anions

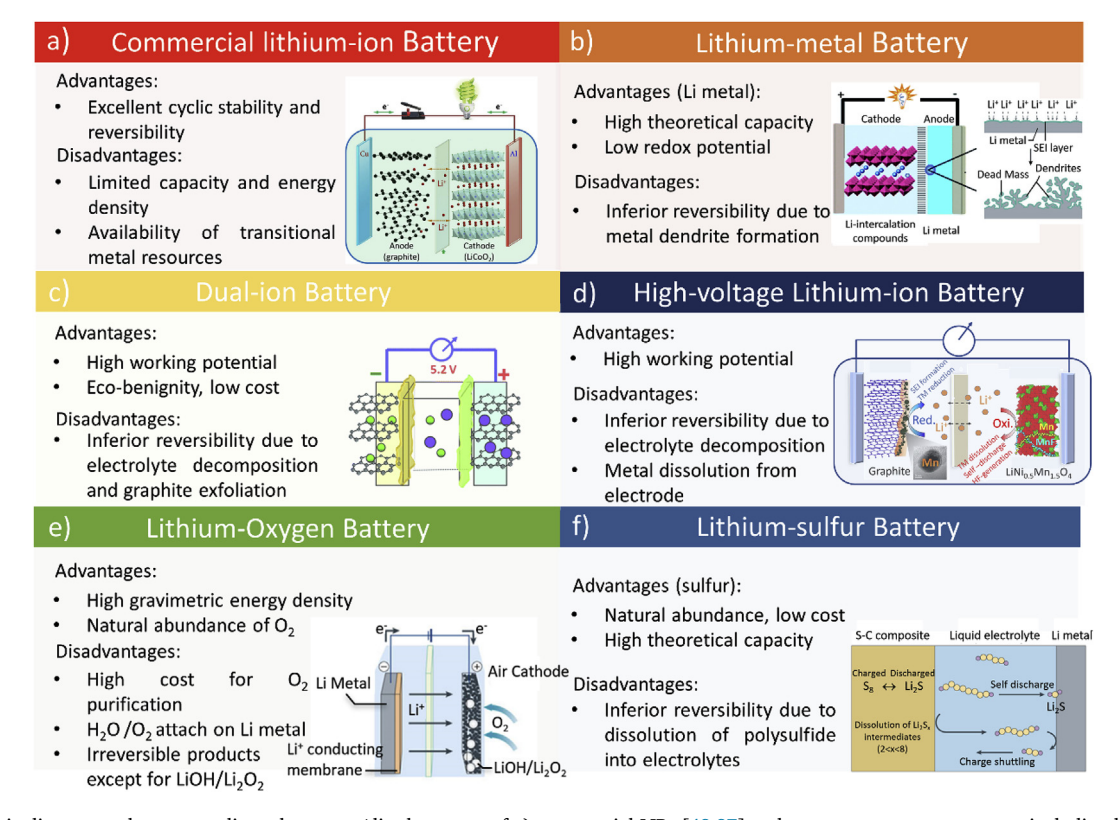


Fig. 2. Schematic diagram and corresponding advantages/disadvantages of a) commercial LIBs [48,87] and new energy storage systems including b) Lithium-metal batteries [68,69], c) DIBs [70–74], d) High-voltage LIBs [75,76], e) Lithium-oxygen batteries [77,78] and f) Lithium-sulfur batteries [78,79].

and cations are extracted from positive and negative electrodes to return to the electrolyte. Inherently high working potential (>4.5 V) endows DIBs good potential for high energy density [82]. In addition, positive electrode materials in DIBs mainly include carbon materials and several p-type organics, which are all made from cheap, abundant and environmentally benign elements such as carbon, nitrogen, sulfur [83,84]. Simultaneously, more sustainable cation-based DIBs (e.g. Na $^+$, K $^+$, Ca $^{2+}$, Al $^{3+}$) are emerging to replace the conventional lithium-ion-based DIBs to deal with the draining lithium resources in nature. In addition, DIBs are proven to have great safety as they could still safely and regularly work during the nail test and when electrodes in damaged cells are directly exposed to the air without the appearance of smoke, fire or explosion [85]. DIBs satisfy key requests for future energy storage devices including low cost, sustainability, materials abundance and high safety [86].

The terms "anode and cathode" and "positive and negative electrodes" are commonly used in different research fields, and often causing confusion and misunderstanding. Terms "anode and cathode" are defined by the oxidizing or reducing reaction happened on the electrode. Anode always loses electrons and is oxidized in the chemical reaction and cathode gains electrons to reduce the electroactive species inside. Positive and negative electrodes are defined by the outflow directions of current in the circuit. For a full battery, the current flows out from the positive electrode in the discharging process. It means the gain of electrons on the positive side and reducing reaction happens. In this case, the positive electrode is the cathode and the negative electrode is anode. However, in rechargeable batteries, the flow of current is reversed and the oxidation and reduction reactions are also reversed during the charging process [61]. In this review, the cathode is referred to as the positive electrode and the anode as the negative electrode regardless of the battery operation.

1.2. Development history

The history of DIBs began with the discovery of acceptor-type graphite intercalation compounds (GICs) [82]. In 1938, Rüdorff and Hofmann first recorded the phenomenon by intercalating HSO₄ anions into positive electrode material from the aqueous electrolyte [88]. Then in the 1970s, Armand and Touzain systematically studied the electrochemical properties of acceptor-type GICs which paved the way for their later application in DIBs [89]. In the same year, reversible intercalation of other anions like ClO₄ BF₄, and CF₃SO₃ into graphite was achieved by Dunning et al. with a Li/graphite cell [90]. The first formal DIBs with carbonaceous materials as electrodes and non-aqueous electrolytes was reported by McCullough [91] et al. in 1989. Specifically, the cells in their patents used binder-free pyrolyzed polyacrylonitrile (PAN) electrodes with approximately 90% carbonization as both electrodes and electrolytes with the LiClO₄/LiPF₆ salt dissolved in propylene carbonate (PC). Pyrolyzed PAN, from the current view, is a typical disordered carbon and tends to be a poor candidate for an anion intercalation electrode because the PC molecules easily co-intercalate with the charge carriers and exfoliate the electrode, which hurts the stability and reversibility of the cell [70,92]. The study by Carlin et al. in 1994 provided more options on the electrolyte selection. In their work, multiple room temperature pure ionic liquids (ILs) composed of cations like 1-ethyl-3 methylimidazolium (EMI⁺) and 1,2-dimethyl-3-propylimidazolium (DMPI⁺) and anions like CF₃SO₃, AlCl₄, C₆H₅CO₂, PF₆ and BF₄ were studied as electrolytes [93]. In 2000, Seel and Dahn first discussed the staging process of PF₆ intercalation into graphite positive electrode via in-situ XRD and achieved stage II of GICs, corresponding to structure of PF₆C₁₆ and specific capacity of 140 mA h·g⁻¹ for graphite/Li cells in 2 M LiPF₆/ethyl methyl sulfone (EMS) electrolytes when cycled to 5.5 V [74,94]. After this landmark work, increasing focus has been moved on to the electrochemical insertion/de-insertion of anions within graphite positive electrodes and further application in graphite-based DIBs. In 2012, Placke et al. first introduced the definition "dual-ion batteries" for the type of batteries and the name is used till today.

To note, earlier DIBs typically applied graphite as both electrodes, liquid organic solvents and lithium salts as electrolytes. That is why the earlier DIBs are also called dual-graphite batteries (DGBs) or dual-carbon batteries (DCBs) [82]. However, the DIBs suffered from several fatal problems including: i) electrolyte decomposition at high working voltage (>4.5 V) [72], ii) graphite exfoliation induced by large anion and solvents co-intercalation [72], iii) moderate capacity due to limited active crystallographic sites in graphite electrodes [78], iv) draining lithium resources brought by booming electric vehicle (EV) markets [95]. Hence, researches in recent years put a lot of focus on the exploration and development of new materials (e.g. electrodes, electrolytes, separators and current collectors) to solve the corresponding problems. As a replacement for conventional organic solvents, ionic liquid solvents, some of which serve the charge carriers simultaneously, are considered promising alternatives in DIBs. In 2012, Placke et al. applied LiTFSI salt and Pyr₁₄TFSI ionic liquid as electrolyte and graphite/Li metal as positive electrode/counter electrode. An over 99% Coulombic efficiency was achieved at a cut-off voltage of 5.0 V and nearly 99% capacity was preserved after 500 cycles [96]. In 2014, Read et al. brought fluorinated solvents/additives into DIBs system, which allowed graphite as both electrodes-based cells reversibly working at 5.2 V with Coulombic efficiency of 97% [70]. In 2015, a series of organic positive electrodes including Fe₂(dobpdc) [97] and thianthrene polymer [98] were applied in DIBs as alternatives for conventional graphite positive electrode and both of them supported the reversible insertion/de-insertion of anions. The success of organic positive electrodes as anions host opened the door of study on novel DIBs in addition to graphite-based ones. To deal with the upcoming shortage of lithium resources in nature, using more abundant elements as charge carriers in DIBs becomes attractive and promising. The first sodium-ion-based DIBs (denote as Na-DIBs) were reported by Bordet et al. but only the half-cell performance was studied in their work [99]. In the same year, Dai et al. reported the aluminum-ion-based DIBs (denote as Al-DIBs) with good rate performance and reversibility [100]. Thereafter, Ca²⁺ [101], K⁺ [102], Zn²⁺ [103] -based DIBs were successfully realized. Considering the delivered capacity and compatibility with alkali metal ions, metal negative electrodes powered by alloying mechanism are expected to be promising options for DIBs [104]. Besides, metal negative electrodes that serve as both current collector and host material could effectively cut the inactive mass, in turn, increasing the energy density of full cells [105-107]. In 2018, Zhang et al. applied BiF3 as anion-hosting materials and first realized the aqueous-solvent-based DIBs [108]. This breakthrough paves a new revenue for studying DIBs and many recent works push the idea forward [109-114].

In spite of the rapid development of DIBs, only a few review papers have been published [81,82,104,115,116]. In 2017, Ji et al. first summarized and categorized the positive electrode materials in DIBs. However, a lot of essential progress has been made afterwards, so the information offered in the work is limited from today's perspective [82]. Thereafter, several review papers were published with major focus on one or several aspects of DIBs like the energy storage mechanisms [81, 117], electrolytes [118], alternative cation-based DIBs for Li-based DIBs [117,119], electrode materials [81] and the practical issues of DIBs and their potential for large-scale use in comparison to LIBs [115]. In comparison, Tang et al. [104] and Guo et al. [116] had review papers separately which gave more comprehensive introduction of the progress made in DIBs, but both works merely covered part of the problems existing in DIBs. Under the circumstances, this review intends to fill the gap of fundamental and comprehensive discussion of problems in DIBs from the perspectives of electrodes including both positive and negative electrodes and electrolytes including solvents and salts, and provides a comprehensive coverage of the solutions corresponding to the problems. Besides, some fundamental and technical similarities and differences between DIBs and conventional LIBs are introduced and discussed before the summary of problems DIBs have and possible solutions in order to help better understand the configuration and principle of DIBs. And in

the last part, the challenges remaining in the current stage of DIBs and some potentially feasible routes of improvement are discussed as the guidance of future development and large-scale use.

2. Principle and configuration

The device configuration of DIBs is the same as that of conventional rocking-chair batteries: negative and positive electrodes separated by a polymer membrane and electrolyte. The differences between rockingchair batteries like LIBs (the schematic diagram shown in Fig. 3a) and DIBs (Fig. 3b) originate from the insertion mechanism and types of charge carriers. In rocking-chair batteries, only the cations participate in electrochemical reactions at both positive electrode-electrolyte and negative electrode-electrolyte interfaces. The active charge carriers are initially stored commonly in positive electrode materials such as LiCoO₂ and LiFePO₄, so the concentration of cations in the electrolyte remains constant regardless of the degree of charge or discharge (unless they are consumed during the solid electrolyte interphase (SEI) formation) [120, 121]. In contrast, DIBs proceed simultaneous intercalation of anions into the positive electrode and cations into the negative electrode during charging process and conversely de-intercalation of ions into electrolytes during discharging process; both anions and cations are being taken from and released to the electrolyte. The concentrations of both cations and anions in the electrolyte vary within the charging/discharging processes. Since the electrolyte provides charge carriers within DIBs, the storage capacity, energy density, power density could be limited by the electrolyte. That is why the electrolyte layer including the electrolyte and the separator in rocking-chair batteries could be made very thin (10-30 µm) in order to improve the overall energy density, while the electrolyte layer within DIBs has to be relatively thicker (>100 µm depending on the type of electrolyte) to ensure sufficient amount of charge carriers [115, 122-124]. This peculiar characteristic of DIBs demands holistic improvement and optimization of all active constitution materials including electrolyte, separator and electrodes to attain high energy density and device performance. Obviously, separator with high porosity (60%-80%) and electrolytes with highly concentrated intercalation cations and anions are needed.

The working potential or called open circuit potential (V_{OC}) of DIBs, similar to LIBs, is collectively determined by the differential chemical potential of positive electrode(μ_P) and negative electrode (μ_N) as

expressed in Equation (1) [48,125].

$$neV_{OC} = n(\mu_N - \mu_P) \tag{1}$$

When connected with the external circuit, the electrons will flow outside the cells while ions transfer between electrolytes and electrodes to neutralize the charges. The reactions happened within DIBs and LIBs are presented in respective Equation (2) and Equation (3), where E_A and E_C stand for negative and positive electrodes materials separately.

$$xLi^{+} + xA^{-} + E_{P} + E_{N} \Leftrightarrow Li_{x}E_{N} + E_{P}A_{x}$$
(2)

$$Li_x E_P + E_N + xLi^+ \Leftrightarrow xLi^+ + E_P + Li_x E_N \tag{3}$$

The changes in chemical potential of both electrodes can be simplified as the difference between chemical potential of charge carriers inserted into electrodes and chemical potential of ionic-state charge carriers within electrolyte, in which chemical potential of charge carriers inserted into electrodes is seen as the chemical potential difference between the formed graphite intercalation compound (GIC) and the pristine graphite cathode. The distinction between derived potential changes of DIBs and LIBs becomes noticeable (see Equation (4), Equation (5) separately) as anions within DIBs and lithium ions within LIBs on cathode side transfer towards opposite directions [74].

$$\Delta V = \frac{(\mu_{N(Li^+)} - \mu_{N(Li)}) + (\mu_{P(A^-)} - \mu_{P(A)})}{e}$$
 (4)

$$\Delta V = \frac{(\mu_{N(Li^+)} - \mu_{N(Li)}) - (\mu_{P(Li^+)} - \mu_{P(Li)})}{e}$$
 (5)

where $\mu_{N(Li^+)}$ and $\mu_{P(Li^+)}$ represent the chemical potentials of free lithium ions in electrolyte on negative and positive electrode sides respectively. $\mu_{N(Li)}$ and $\mu_{P(Li)}$ stand for the chemical potential of lithium inserted into negative and positive electrodes, respectively, and $\mu_{P(A^-)}$ is short for the chemical potential of free A anions in electrolyte on positive electrode side, $\mu_{P(A)}$ refers to the chemical potential of A inserted into positive electrode. As the chemical potential of lithium ions is constant within electrolyte, $\mu_{N(Li^+)}$ and $\mu_{P(Li^+)}$ can offset each other. For DIBs, the Nernst equation is applied to derive the $\mu_{N(Li^+)}$ and $\mu_{P(A^-)}$ to Equation (6) and Equation (7) with the consideration of electrolyte limit [74].

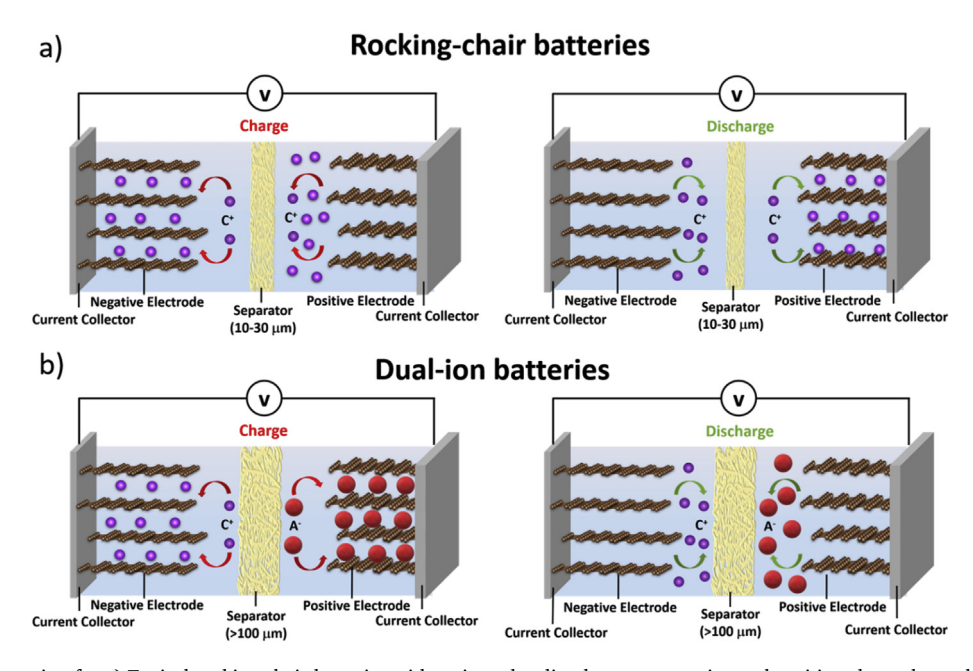


Fig. 3. Schematic configuration for a) Typical rocking-chair batteries with cations shuttling between negative and positive electrodes and b) DIBs with anions and cations working as charge carriers simultaneously.

$$\mu_{N(Li)^{+}} = \mu_{N(Li^{+})}^{0} + kTln[Li^{+}]$$
(6)

$$\mu_{P(A^{-})} = \mu_{P(A^{-})}^{0} + kT \ln[A^{-}]$$
(7)

in which $\mu^0_{N(Li^+)}$ and $\mu^0_{P(A^-)}$ stand for the chemical potential of Li⁺ and A⁻ in 1 M solution separately. Finally, the working potential of DIBs and LIBs are separately converted to Equation (8) and Equation (9) [74].

$$\Delta V = \frac{\mu_{N(Li)} + \mu_{P(A)} - \mu_{N(Li^{+})}^{0} - \mu_{P(A^{-})}^{0} - kT \ln[Li^{+}] - kT \ln[A^{-}]}{e}$$
 (8)

$$\Delta V = \frac{\mu_{P(Li)} - \mu_{N(Li)}}{e} \tag{9}$$

As noticed, $\mu^0_{N(Li^+)}$, $\mu^0_{P(A^-)}$, $kT \ln[Li^+]$ and $kT \ln[A^-]$ terms in Equation (8) are all closely related to the composition of electrolytes, like salt concentration. In contrast, there are no terms in Equation (9) that correlates the electrolytes. Concerned that the insertion charge carriers are fully from the electrolytes in DIBs, electrolytes should also be counted as active mass for calculating the specific capacity, energy density and so forth [104].

Remarkably, the average discharge voltage for typical DGBs can reach over 4.5 V vs. Li/Li⁺ (shown in Fig. 4a), which is far higher than that of conventional LIBs (e.g. ~3.3 V for the LiFePO₄//graphite cells and \sim 3.6 V for the LiCoO₂//graphite cells) [70,126–131]. The high working potential endows DIBs very bright future to achieve high energy density. Nevertheless, this attractive feature of DIBs also brings some challenges. As known, the working potential should be limited within the stable electrochemical window of electrolytes for stable/reversible cycling, specifically, μ_A lying below the lowest unoccupied molecular orbital (LUMO) and μ_C lying above highest occupied molecular orbital (HOMO) of electrolytes which is demonstrated by Fig. 4b [47,125]. As chemical potential of positive electrode lies below HOMO of electrolyte, the electrolyte will get oxidized on the surface of positive electrode to form cathode electrolyte interphase (CEI) layer, leading to the loss of Coulombic efficiency or the direct death of whole battery in a worth situation [132,133]. Furthermore, in a realistic situation, the charge carriers including anions and cations dissolved in organic-based electrolytes are solvated. Co-intercalation of solvents with charge carriers has been well reported and the enlarged size is easy to induce the exfoliation of graphite electrodes [134,135]. When effective SEI and CEI are formed on surface of negative and positive electrodes, the de-solvation process will happen as charge carriers insert into hosting materials, which also correlates with the working potential of DIBs. Specifically, higher enthalpy brought by de-solvation process may contribute to a lower working potential according to the thermodynamics calculation done by

Ji et al. [82].

3. Positive electrodes

In LIBs, the positive electrode material is considered one limiting factor in determining the performance of full cells since the negative electrode materials usually offer more Li-storage sites than the positive electrode counterparts [48,54,136]. Similarly, development of high capacity and energy density DIBs are also restricted by the positive electrode materials. For intercalation-type graphite positive electrode, most of the anions (i.e. PF₆, TFSI⁻) possess larger sizes and lower diffusivity than alkali metal cation counterparts, which hurt the cyclic stability and rate capability [81]. Limited active sites for accommodating anions in graphite, namely low theoretical capacity, genuinely overshadows graphite future development and application. And they suffer from the low cyclic stability due to solvent co-intercalation with anions [134,135]. In the development history of graphite-positive electrode-based DIBs, factors and strategies are well-studied. Meanwhile, some alternative positive electrode emerged, part of which possessed attractive advantages and displayed outstanding performance compared to graphite-based DIBs and were even comparable to LIBs performance. In the following section, fundamental issues in graphite positive electrodes, intrinsic drawbacks of graphite positive electrodes in DIBs and corresponding solutions to improve their performances, novel positive electrode materials are separately categorized and discussed.

3.1. Conventional graphite electrodes

3.1.1. Fundamentals in graphite

To date, graphite has been well-studied in LIBs as negative electrode materials and is also the most common material for the positive electrode in DIBs because of its attractive properties [46,82]. As known, an ideal graphite crystal lattice consists of graphene sheets stacked in ABAB sequence separated by 0.335 nm and held together with weak van der Waals forces (shown in Fig. 5) [137]. The well-arranged structure allows for the reversible intercalation/de-intercalation of charge carriers [138, 139]. Within a single sheet, sp² hybridized carbon atoms are tightly bonded in standard hexagonal rings through strong co-valent bonds, which accounts for the superior mechanical strength (~130 GPa) and large Young's modulus (1 TPa) of graphene sheets [140-142]. Perpendicular to the graphene plane are the remaining "2pz" orbitals, which hybridize to form the partially filled, delocalized band structure that allows for high electron mobility (~200000 cm² V⁻¹ s⁻¹) [137, 143-145]. This property also accounts for its redox amphotericity, enabling graphite to act as both the negative and positive electrodes in DIBs. Specifically, its 2D zero-gap semi-metallic electronic structure

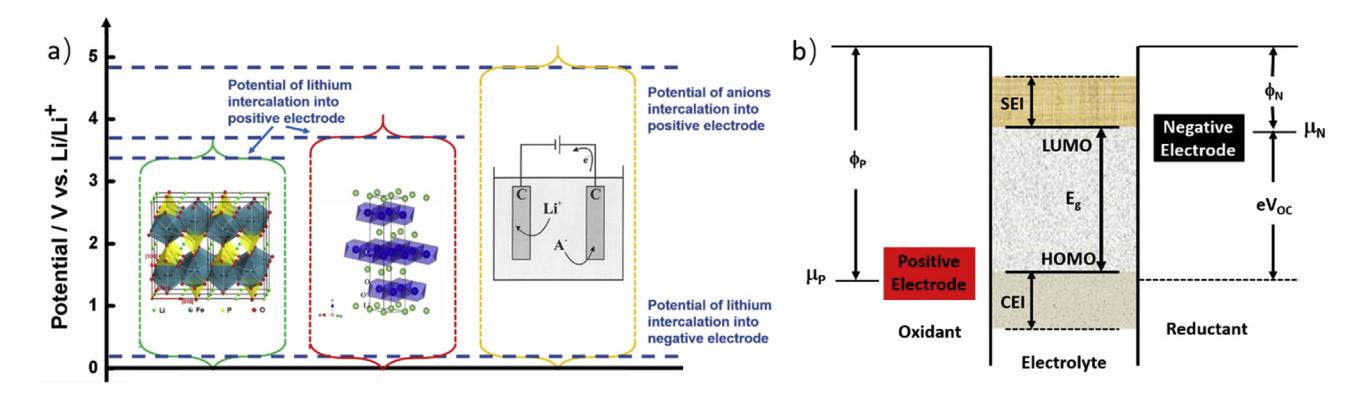


Fig. 4. a) The potential range of three types of batteries with reference to lithium metal, in which commercial LiFePO₄//graphite LIBs (in green) possess the average discharge voltage of $3.3 \, \text{V}$, commercial LiCoO₂//graphite LIBs (in red) possess the average discharge voltage of $3.6 \, \text{V}$ and DGBs (in yellow) have average discharge voltage exceeding $4.5 \, \text{V}$ [126,129-131]. b) The originality of open circuit potential (V_{OC}) and energy states of electrodes and electrolytes enabling a healthy operation [47,125]. (For interpretation of the references to colour in this figure legend, the reader is referred to the Web version of this article.)

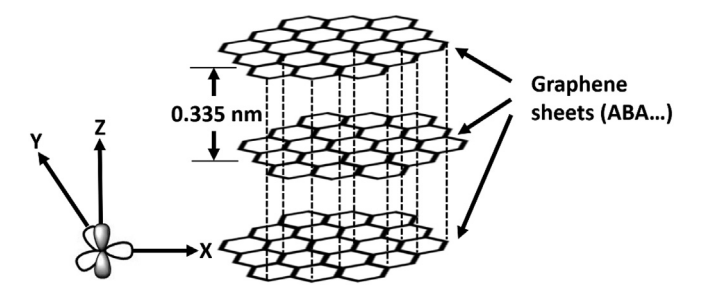


Fig. 5. Crystal structure of the graphite with a layered structure [137].

allows it to form donor-type GICs by stabilizing excess electrons in its antibonding π^* -band, or acceptor-type GICs by stabilizing extra holes in its bonding π -band through delocalization [82]. Hence, when charged to certain potentials, the driving force will be great enough for many types of cations and anions to overcome the weak van-der-Waals forces between graphene sheets. These include metallic cations like Al³⁺ [100], Na⁺ [99], and Li⁺ [74]; cations from molten salts like Pyr $_{14}^{+}$ [96]; fluoride anions such as PF $_{6}^{-}$ [74], BF $_{4}^{-}$ [146]; chloride-based anions like AlCl $_{4}^{-}$ [100]; oxide based guests like ClO $_{4}^{-}$ [106]; carbon-based anions like TFSI $_{4}^{-}$ [147] and so forth.

Because of the ABAB structure of graphite, anions insert into the layers in certain sequences, rather than simultaneously. The process is known as staging, first described by Rüdorff and Hofmann in 1940 [148]. It is proposed that the intercalant sequentially fills up graphene interlayer spaces, inducing no structural distortions on the graphene layer, as presented in Fig. 6a [148]. The stage number indicates the number of interjacent graphene layers between layers accommodating intercalants. However, this model oversimplifies the process. As a matter of fact, the graphene layers in graphite are flexible. Phonon dispersion experiments have measured the bending modulus to be 9.93×10^{-20} J [149]. Later in 1969, Daumas and Herold proposed a more realistic model, in which ions inserted into graphene layers simultaneously, then deforming the layers around them as illustrated in Fig. 6b [150,151]. The staging phenomenon is allowed by subsequent diffusion of the intercalant ions which is more accessible compared to diffusion along the c-axis in the Rüdorff model. Additionally, this model more readily explains the coexistence of domains with different stages in the same crystallite [150,151].

The structural changes of graphite indicate the so-called "staging" process [102,152]. The most direct and clearest methods to observe the "staging" process are galvanostatic charging/discharging [102] (Fig. 7a), cyclic voltammetry (CV) [152] (Fig. 7b) and derived differential capacity (dQ/dV) [102] (Fig. 7c). As known, the intercalation and de-intercalation processes occur at certain potentials, corresponding to the peaks in CV,

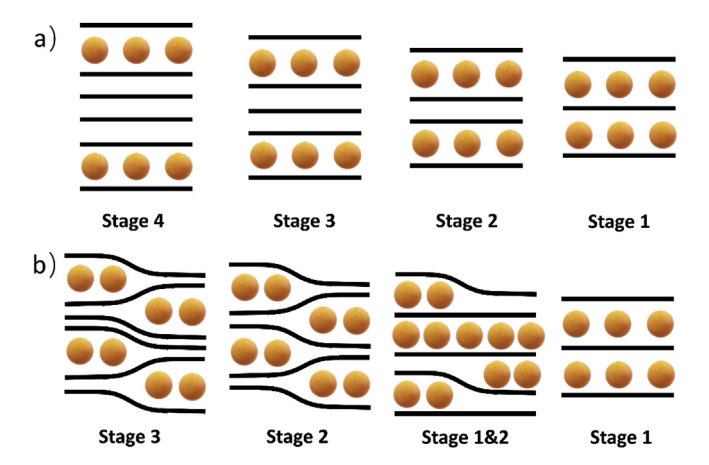


Fig. 6. a) Schematic diagram of the conventional Rüdorff staging model with no structural distortion of the graphene layer [148] and b) The Daumas-Herold model with graphene layers bent during the staging process [151].

dQ/dV profiles and plateaus in the charging/discharging curves. However, these methods are hard to quantify the stages. As a comparison, X-ray diffraction (XRD) and Raman spectroscopy are more explicit in marking the stage value of GICs.

In typical X-ray diffraction patterns for graphite electrodes [152], the initial independent (002) diffraction peak located at 26.5° belongs to highly pristine graphite [126]. After anion intercalation, this peak will completely disappear and new peaks arise at a lower angle for (00(n+1))reflections and a higher angle for (00(n+2)) reflections, in which n stands for the dominant stage number. The observed intensity commonly follows the order I(00n + 1) > I(00n + 2) > I (all the other reflections) [152,153]. The new peaks' appearance indicates anions succeeding in intercalation into the graphene sheets due to the lattice expansion of graphite. Schmuelling et al. investigated this phenomenon for TFSIintercalation, whereby they determined the dominant stage and the gallery height, and also correlated experimentally obtained capacity with theoretical specific discharge capacities for different graphite stages [147]. The general method to derive the spacing of (00n) planes (d_{00n}) is shown in Equation (10) [154]. Furthermore, in the case of graphite, the general equation can be further derived to relate more parameters like the periodic repeating distance (I_c) , the gallery expansion (Δd) and the intercalant gallery height (d_i) in addition to the dominant stage number (n) through Equation (11a) in which l represents for the index of (00l) planes in the stacking direction while d_{obs} is the observed distance between two adjacent graphene planes [147,152,153,155].

$$d_{00n} = \frac{I_c}{n} = \frac{\lambda}{2\sin\theta_{00}} \tag{10}$$

$$I_c = d_i + 3.35 \text{Å} \cdot (n-1) = \Delta d + 3.35 \text{Å} \cdot n = l \cdot d_{obs}$$
 (11a)

When charged to consistently higher voltages, the peak at the lower angle continues to shift left while the peak at the higher angle will shift right. When anion de-intercalation begins, the shift of the (00(n+2)) peak to lower 2θ values and (00(n+1)) peak to higher 2θ values can be observed in Fig. 8 [146]. By discharging to a certain potential, the later emerged peak do not fully disappear while the pristine peak decreases in intensity and becomes wider which result from the remaining of anions between the graphene sheets, leading to a decreased long-range order and a broader peak [146,152,154].

For Raman spectroscopy, the G (graphite) band at $1582\,\mathrm{cm}^{-1}$ in Fig. 9a is supposed to be the only peak appearing in the spectrum for highly crystallized graphite since it is associated with the motion of sp²hybridized carbon atoms [151]. However, carbonaceous materials are usually composed of polycrystalline particles and defects within their graphene sheets, which leads to the emergence of peaks at \sim 1350 cm⁻¹ corresponding to the D (defect) band. Additionally, the so-called 2D band has peaks at $2682 \, \text{cm}^{-1}$ and $2722 \, \text{cm}^{-1}$ which is assumed the overtone of the D peak and can be observed even in the spectrum of a perfect crystal [151,156-158]. As the intercalation process begins, the G peak disappears immediately and two peaks at higher wave number emerge, where lower wave number peak and higher wave number peak correspond to the vibrational mode of the inner graphene layers (E2g(i)) adjacent to other graphene layers and vibrational mode of the boundary graphene layers ($E_{20}(b)$) adjacent to intercalant layers separately [151]. The new peaks are blue shifted as the intercalation process continues, partially due to the increasing charges within graphene layers (see Fig. 9b) [159,160]. Because the transferred charges mainly remain at the outer surface $(E_{2g}(b))$ rather than the inner layer $(E_{2g}(i))$, the peak corresponding to surface graphene has a more pronounced shift (~20 cm⁻¹) over its counterpart (<10 cm⁻¹) [161]. The shift during charging is an evidence for transitions to progressively lower stage numbers $(5 \rightarrow 4 \rightarrow 3 \rightarrow 2 \rightarrow 1)$ [151,162]. As potential decreases, the $E_{2g}(b)$ mode shows a gradual red shift but sometimes there are sudden red shifts of the boundary layer mode and of the inner-layer mode which match with the de-intercalation peak visible in the differential capacity curve (see Fig. 9c) [160]. Stage

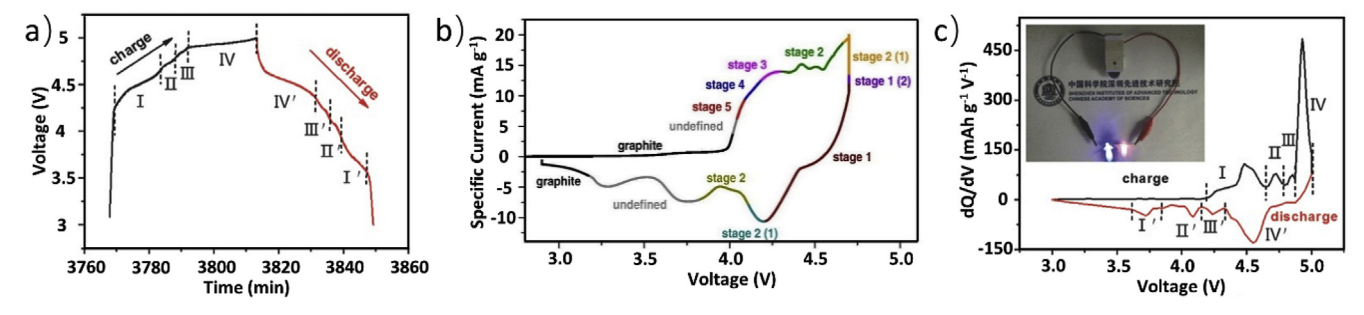


Fig. 7. a) A complete galvanostatic charge-discharge cycle of the Al-expanded graphite K-DIBs [102]. b) CV curve for intercalation of FTFSI⁻ into graphite [152]. c) dQ/dV curve which describes the dominant stages [102].

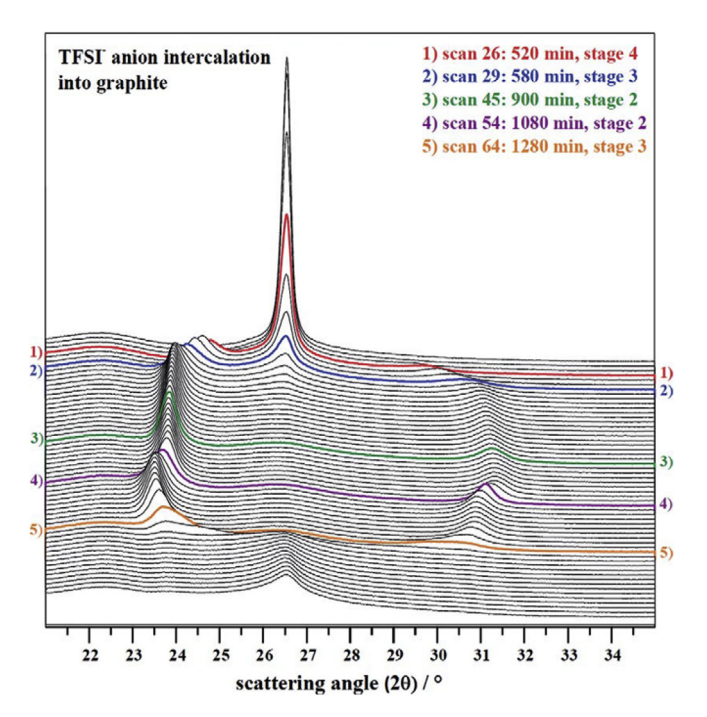


Fig. 8. In-situ XRD pattern for TFSI⁻ anion insertion/de-insertion within KS6L graphite and electrolytes of 1 M LiTFSI/Pyr₁₄TFSI [146].

numbers for the GICs can be calculated using the intensity ratio R of the $E_{2g}(i)$ mode and the $E_{2g}(b)$ mode. In Equation (11b), I_i and I_b denote the peak intensities of the $E_{2g}(i)$ mode and the $E_{2g}(b)$ mode respectively and the term σ_i/σ_b represents the ratio of the cross-sectional area for Raman scattering between the inner layers and the boundary layers [151,163].

$$R = \frac{I_i}{I_b} = \frac{\sigma_i}{\sigma_b} \frac{n-2}{n}$$
 (11b)

3.1.2. Graphite positive electrode: intrinsic drawbacks

For graphite positive electrodes, limited specific capacity and cyclic stability are primary issues to consider and may negatively influence their practicality. Typically, anions possess larger radii than cations (Fig. 10) [37,81,146,164]. As the space for holding charge carriers within the positive electrode is limited, fewer anions can intercalate into the positive electrode, leading to much lower capacity compared to its single-ion counterpart. For example, the intercalation of lithium ions in graphite to form LiC₆ has a theoretical capacity of 372 mA h·g $^{-1}$ with merely 10% volume change [165–167]. In contrast, intercalation of PF $_6$ anions results in approximately a 136% volume change, forming C₂₄PF $_6$, the specific capacity of which is only 93 mA h·g $^{-1}$ (Fig. 11) [146]. Furthermore, in organic electrolytes, some solvents (i.e. PC) are reported co-intercalating with PF $_6$ and BF $_4$ into graphite positive electrode in DIBs. As further evidence, BF $_4$ intercalated from acetonitrile and PC

display different gallery heights of $5\pm0.3\,\text{Å}$ and $8\pm2\,\text{Å}$ [168]. This is also a common phenomenon in the negative electrode side of LIBs which is related to the solvation of charge carriers [136,169]. Ideally, GICs are binary phases of M⁺ Cⁿ⁻ and Cⁿ⁺ X⁻, without the co-intercalation of solvents. However, solvated ions M⁺ (solv)_y and (solv)_y X⁻ with much larger sizes are sure to induce greater expansion along z axis and increase the intercalation potential [146,170]. Later contributions provide deeper insights into the negative effects of charge carrier solvation in DIBs. Graphite exfoliation from dramatic volume expansion and contraction only partially accounts for performance loss [134,135].

In addition, rate performance is also a very important factor to evaluate batteries. It is closely related to the transfer rate of charges and ions in both electrolytes and electrodes [171]. Taking PF₆ anion as an example, the activation energy for inserting PF₆ into graphite in a LiPF₆/dimethyl carbonate (DMC) electrolyte is estimated to be 0.37 eV $(35.7\,\mathrm{kJ~mol}^{-1})$, corresponding to diffusion coefficient of 10^{-12} to $10^{-11} \,\mathrm{cm^2 \, s^{-1}}$ at room temperature. As a supporting information, the activation energy is also calculated based on density functional theory (DFT) assuming the tilted structure in stage 1 (the optimized geometry for GICs formed by anion intercalation, diffusion route and corresponding energy state are displayed in (Fig. 12a and b), with the lowest value of $0.23 \,\mathrm{eV} \, (22.1 \,\mathrm{kJ} \,\mathrm{mol}^{-1})$ when migrating along the <100> families of directions [172]. It is even comparable to the diffusion coefficient of Li⁺ ion in common positive electrode materials of LIBs (i.e. $3\times10^{-15}\,\text{cm}^2\,\text{s}^{-1}$ for LiCoO₂ [172] and $1.8 \times 10^{-14} \, \text{cm}^2 \, \text{s}^{-1}$ for LiFePO₄ [173]) but far inferior to Li^+ ion diffusion coefficient in graphite $(4.4 \times 10^{-6} \, \text{cm}^2 \, \text{s}^{-1}$ along the graphene sheets) [174] The result is acceptable considering the large molecular size of PF₆ but the improvements of graphite-positive electrode-based DIBs is still needed in order to meet the demand of fast charging and high power delivery [171,175].

3.1.3. Influencing factors and strategies

As a matter of fact, performances of graphite are co-determined by various factors like graphitization extent, particle size, surface area, surface modification and so forth. In the following part, we will discuss the specific influence of these factors on graphite performance and some derived strategies to ameliorate the above drawbacks brought by graphite positive electrode in DIBs.

Firstly, the degree of graphitization or crystallinity of the carbon is of great importance to the discharge capacity and reversibility. Within a range, higher crystallinity/graphitization will lead to higher discharge capacity. For non-graphite carbons, heat treatment is a suitable way for them to improve the degree of graphitization. The degree of graphitization reaches 90% percent when heated to 2800 °C and leads to a discharge capacity of 100 mA h·g $^{-1}$ (Fig. 13a). Besides, a higher degree of graphitization is also reported to shorten the voltage hysteresis between charging and discharging process, in turn, increasing the voltage efficiency of cycling [176]. Meanwhile, the degree of graphitization influences the interplanar distance between (002) planes in carbon and the highest performance could be achieved when the (002) interplanar distance was 0.334 nm (Fig. 13b) [92].

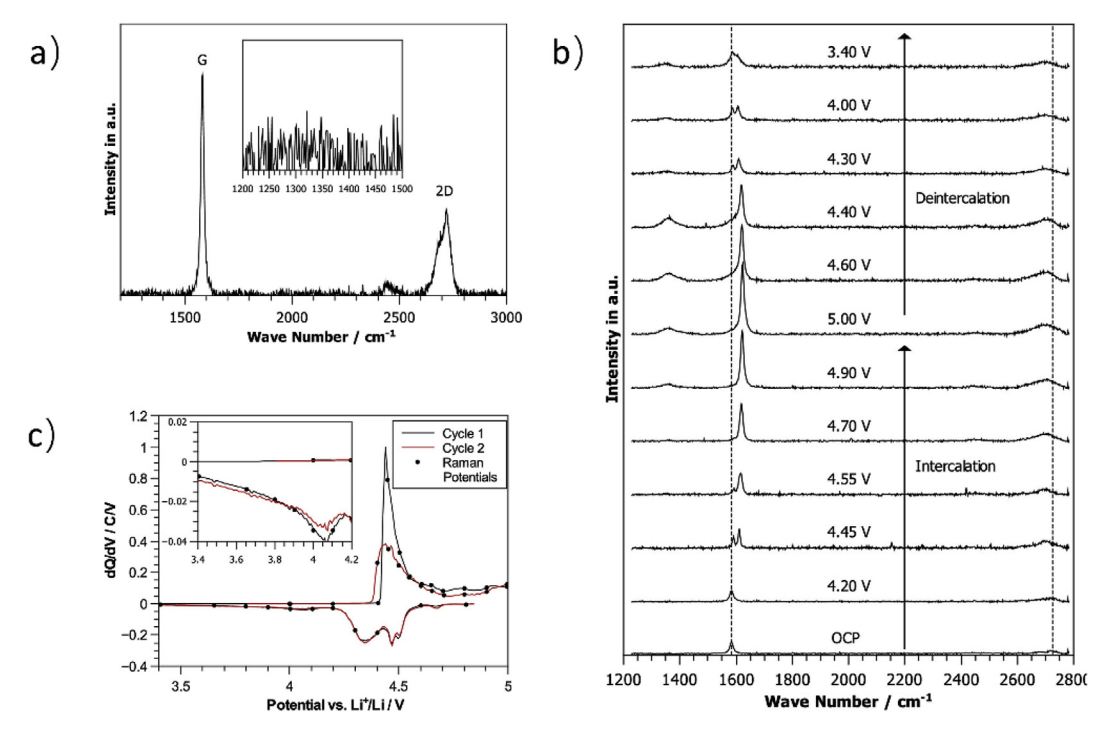


Fig. 9. a) Raman spectra of pristine graphite before experiment, b) Raman spectra changes in the first cycle with TFSI⁻ as the intercalating ion and a LiTFSI/Pyr₁₄TFSI-based electrolyte cycled between 3.4 and 5.0 V and c) differential capacity pattern of the first two cycles [151].

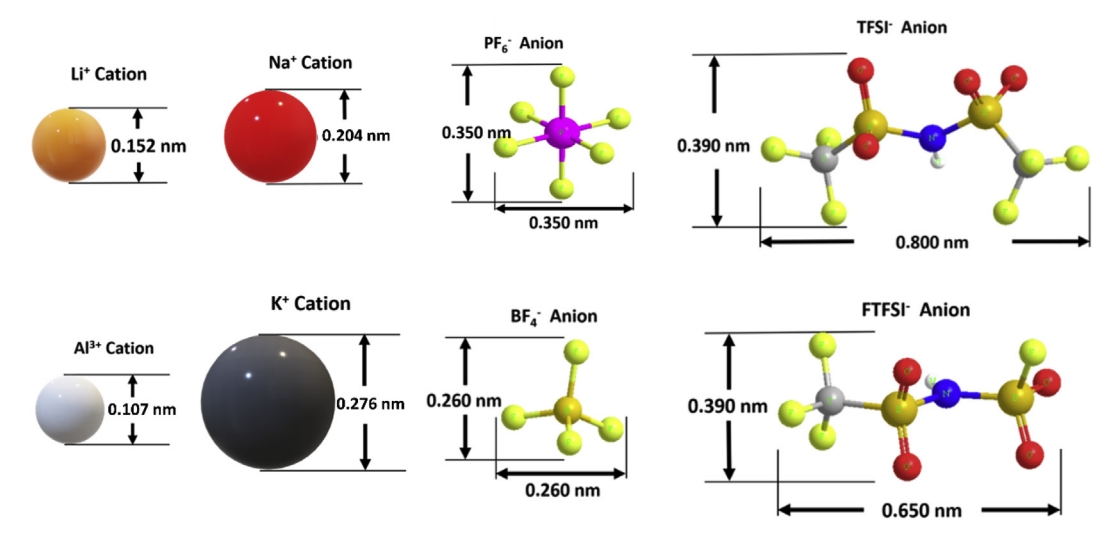


Fig. 10. Schematic structure and estimated size of simple metal cations like lithium ion (Li⁺), sodium ion (Na⁺), aluminum ion (Al³⁺) and potassium ion (K⁺), and complexed anions like hexafluorophosphate (PF₆), bis(trifluoromethanesulfonyl) imide (TFSI⁻), tetrafluoroborate (BF₄) and fluorosulfonyl-(trifluoromethanesulfonyl) imide (FTFSI⁻) anions, in which light green, yellow, red, blue, grey, white balls stand for fluorine (F), sulfur (S), oxygen (O), nitrogen (N), carbon (C), hydrogen (H) atoms respectively [37,81,146,164]. (For interpretation of the references to colour in this figure legend, the reader is referred to the Web version of this article.)

Secondly, defects and dopants (functional group) in graphite directly influence its electrochemical properties. For instance, graphite production usually accompanies with partial oxidation and brings in the oxygen-based groups like carbonyl, hydroxyl group. Unfortunately, this type of groups does harm to the mobility of ions and electrons in graphite. The worse thing is that these groups will bring more defects which further deteriorates the electric conductivity and decreases the crystallinity of graphite [177]. As reported, defect-free graphite (GA3000) is synthesized by annealing reduced graphite oxide (rGO) at 3000 °C and defect-containing graphites including defect-few GA2000 and GA2500 annealed at lower temperature are also synthesized as comparison (Fig. 13c). Consequently, GA3000 presents a capacity of 100 mA h·g $^{-1}$ at 50C for storing AlCl $^{-1}$ anions with 97% capacity remaining and 98%

Coulombic efficiency after over 25000 cycles, which overpasses the defect or functional groups -containing counterparts (Fig. 13d,e) [178].

In addition, particle size also affects the discharge capacity, specifically, smaller particles perform better than larger particles (shown in Fig. 14a), which is clear when employing PC/ethyl methyl carbonate (EMC) as electrolyte [72]. This trend can be attributed to the relative area of two different surfaces. To be specific, it is well known that graphite is composed of two types of surfaces: basal planes that are free of defects and prismatic (edge/surface) planes that contain one atom-thick carbon with unpaired bond and various capping groups like carbonyl, hydroxyl [179–181]. Due to the existence of edge defects, edge plains are reported to contribute several orders of magnitudes better electron conductivities and specific current density in CV curve than basal plains (Fig. 14b and c)

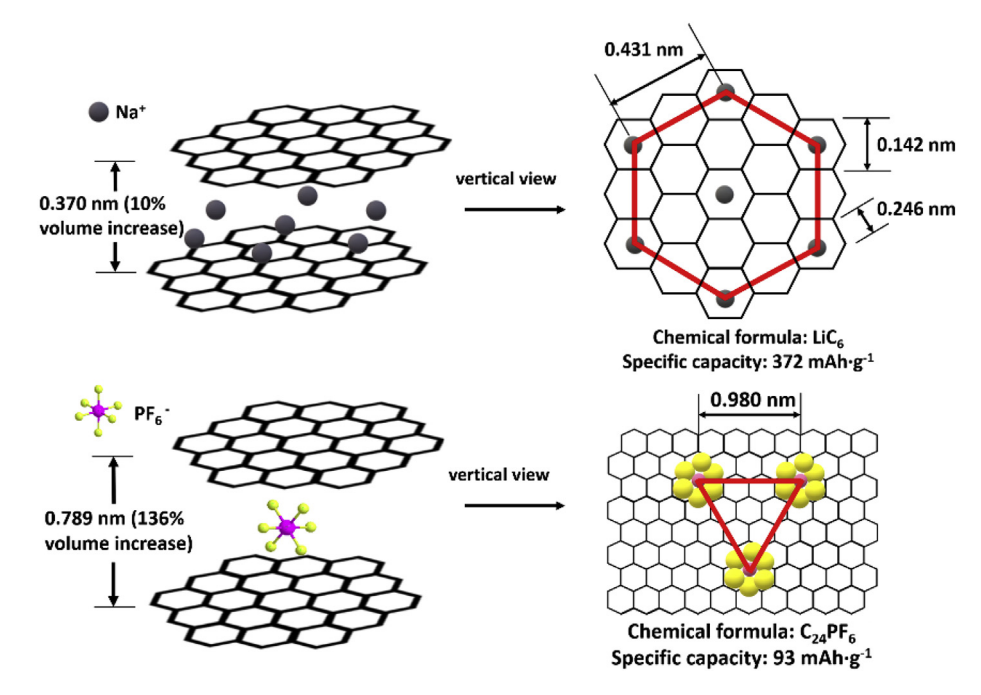


Fig. 11. Schematic diagram of pristine graphite and configuration after intercalation of Li^+ and PF_6^- separately. Furthermore, some values corresponding to LiC_6 and C_{24}PF_6 like capacity, adjacent layers distance are compared in order to illustrate the influence of intercalants' size [143,146].

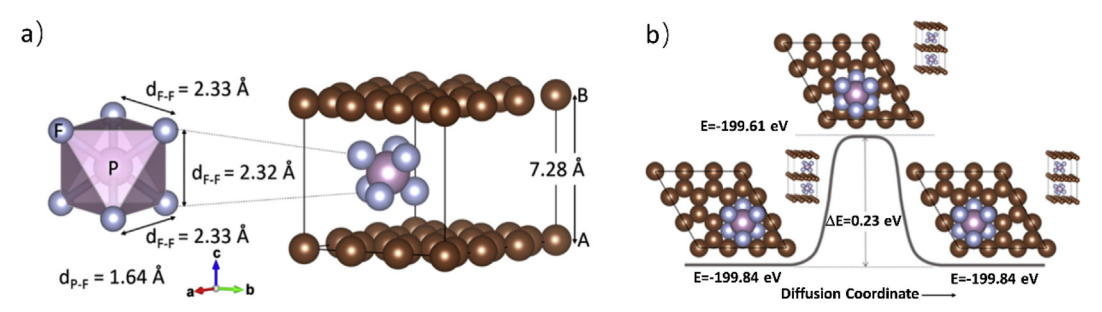


Fig. 12. a) Optimized model of PF₆ intercalation into graphitic carbon and d) diffusion route of PF₆ along the <100> direction in graphite with an energy barrier of 0.23 eV [172].

[96,182]. Hence, when the particle gets smaller, the ratio between surface plain and basal plain will be higher, in turn, the overall performance will be better. Experimental results and DFT simulations support this hypothesis, where increasing the surface area for the KS-type graphite is correlated with increased accommodated amount of TFSI⁻ [183,184]. Meanwhile, decreasing particle size or thickness is also a common method to improve rate performance in LIBs since it helps shorten the diffusion route of charge carriers [185-187]. Inspired by the idea, several works modify the morphology of graphite to increase the amounts of active sites for anions storage and to tune the rate performance. A type of porous graphite with nanoflake morphology (Fig. 14d) or called electrochemically generated nanoflake graphite (abbreviated as EGN) was synthesized through cathodic polarizing amorphous carbons in molten CaCl₂ at 1100 K and compared with commercial graphite powder and nanosheets over performances in DIBs. The porous nanoflake-shape graphite delivers high capacity of $116\,\mathrm{mA}\,\mathrm{h\cdot g}^{-1}$ at a rate of $1800\,\mathrm{mA\,g}^{-1}$ when charged to $5.25\,\mathrm{V}$ vs. $\mathrm{Li/Li}^+$ and outstanding 92% capacity retention when cycling at high rate of 10 A·g⁻¹ between 2.25 V and 5 V, which are better than the other two types of graphite (Fig. 14e) [188]. Another type highly porous graphite foam is also used as positive electrode material in DIBs. With electrolyte of 1 M Al(ClO₄)₃/PC: fluoroethylene carbonate (FEC) (94.5: 5.5, W:W), the cells exhibit approximately $101 \text{ mA h} \cdot \text{g}^{-1}$ capacity at superiorly high rate of 2 A g^{-1} . To note, porous structure can also help buffer volume expansion brought by large

anions intercalation, in turn, improve the cyclic stability. There is barely capacity decay ($\sim \! 100 \, mA \, h \cdot g^{-1}$) with charge rate of 2 A g⁻¹ and discharge rate of 0.2 A g⁻¹ for over 400 cycles [189].

Another route to improve rate performance is finding alternative anions with higher diffusion coefficient within graphite. To note, the diffusion energy barrier of AlCl $_4$ anion in graphite is calculated by first principle method, with the value ranging from 0.012 eV to 0.029 eV, corresponding to a diffusion coefficient of approximately $10^{-4}~{\rm cm}^2~{\rm s}^{-1}$ [81,190]. It is far more superior than PF $_6$ anion [172]. When using graphite foam which is grown on nickel foam through CVD method as positive electrode and aluminum metal as negative electrode, the cell delivers an impressive rate performance, with barely capacity decay when charging rate increase from 0.5 A·g $^{-1}$ to 5 A g $^{-1}$ (Fig. 15a). Meanwhile, 3D porous structure contributes to superior cyclic stability, lasting over 7500 charge/discharge cycles under extremely high current densities (4 A g $^{-1}$) and maintaining a specific capacity of about 70 mA h·g $^{-1}$ and a Coulombic efficiency of approximately 98% (Fig. 15b) 11001

To count, rate performance is also determined by the motion rate of electrons in electrodes which include active materials, binder, conductive additive and current collector. Based on the thought, series of binders (sodium alginate (Alg), sodium carboxymethyl cellulose (CMC), poly(acrylic acid) (PAA), polyvinylidene difluoride (PVDF)) are tested in the positive electrode half cells [191]. It is found that Alg, a bio-derived

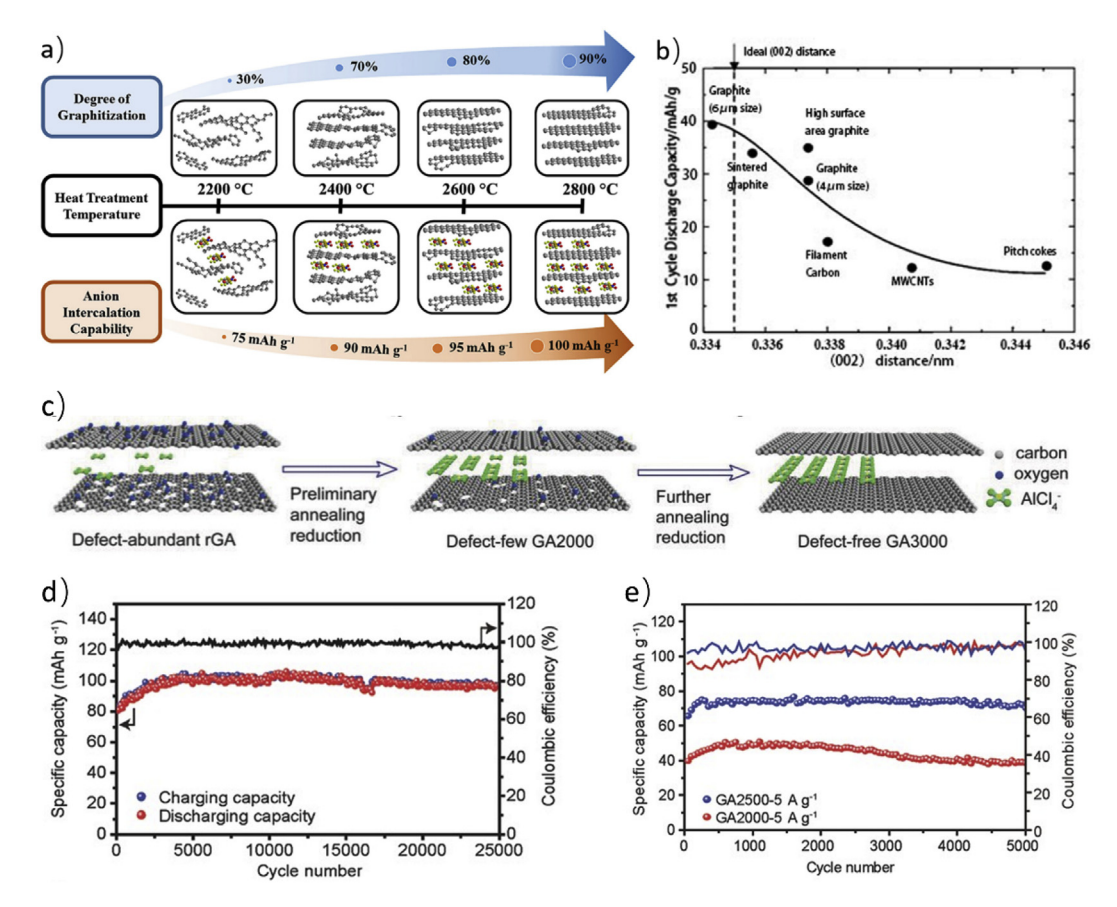


Fig. 13. a) Degree of graphitization as a function of annealing temperature and corresponding discharge capacity in DIBs [176]. b) Initial PF $_6^-$ discharge capacity as a function of the distance between (002) planes (carbon types differ and MWCNTs is short for multiwalled carbon nanotubes) [92]. c) Schematic diagram for the production process of defect-few GA2000 samples and defect free GA3000 samples from defect-abundant rGO and their performances for hosting AlCl $_4^-$ anions [178]. Galvanostatic cycling performance of d) GA3000 and e) GA2500 and GA2000 at the rate of $5A \cdot g^{-1}$ [178].

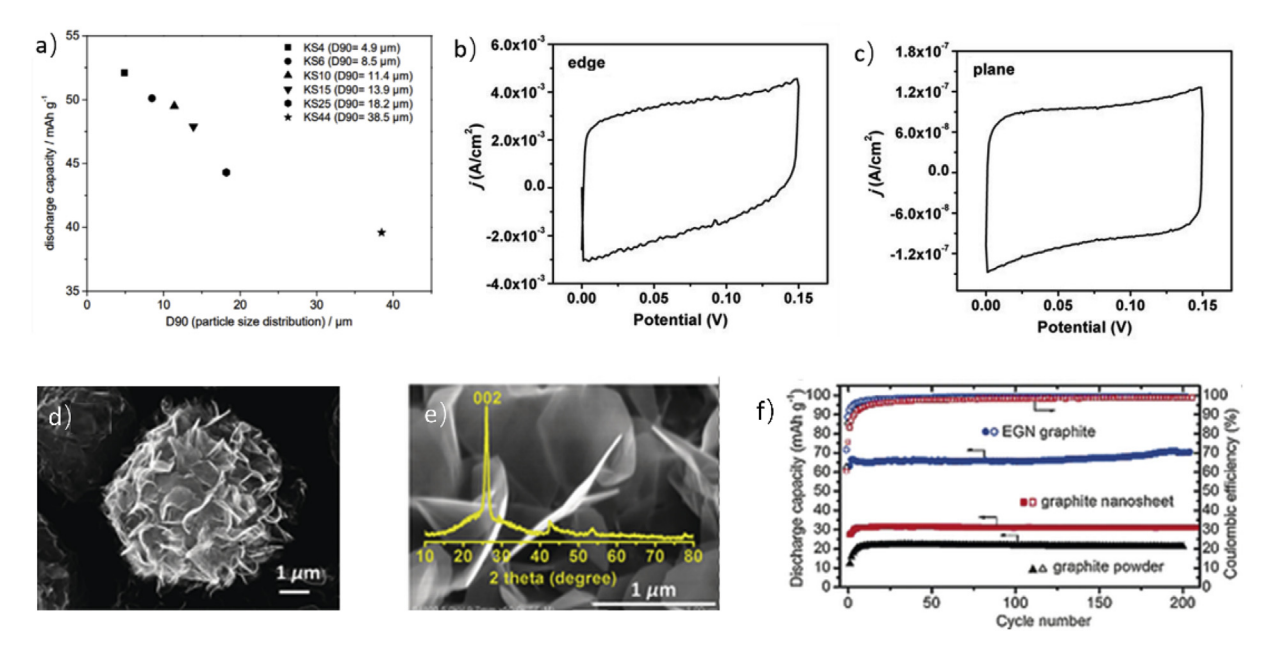


Fig. 14. a) Discharging capacity variation as a function of D90-values (particle size distribution) [183]. b-c) CV curves for both the edge plain and basal plain of graphene electrodes in the 0.1 M PBS solution with 0.1 M KCl under 50 mV s⁻¹ [182]. d-e) SEM images and XRD pattern of porous graphite nanoflake [188]. f) Galvanostatic charging/discharging curves of synthesized EGN, graphite nanosheets, graphite powder at the rate of 10 A g⁻¹ and cycled between 2.25 V and 5 V [188].

aqueous binder, outperforms all the other three types of binders. After the rate capability test, Alg glued graphite shows no obvious structural changes while PVDF-based positive electrode suffers from severe dropping of active materials from current collector. This is ascribed to Alg's high mechanical strength and good interaction with active materials [192,193]. To note, graphite positive electrode using Alg binder

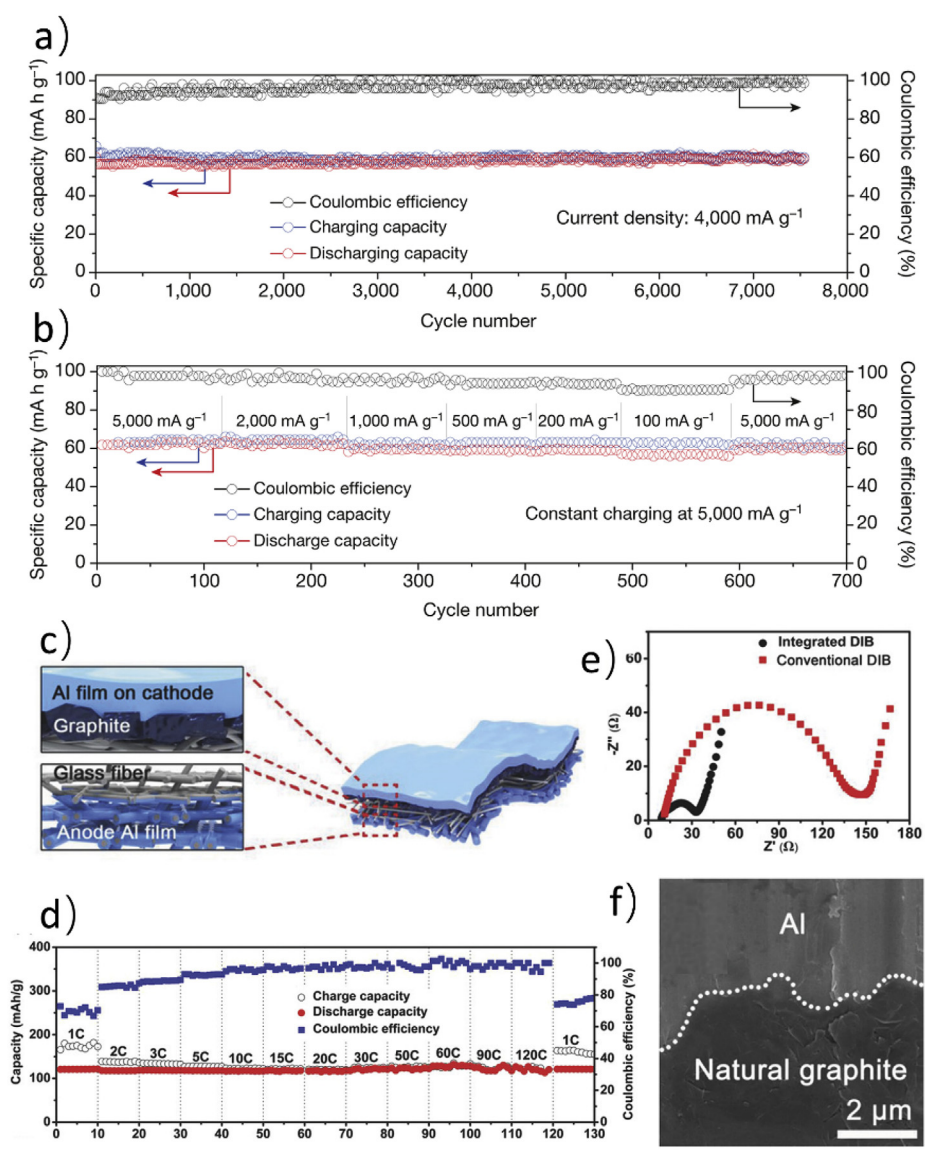


Fig. 15. Performances of $AlCl_4^-$ anion-based DIBs including a) transition of charge/discharge capacity and Coulombic efficiency as a function of the number of cycles at a current density of 4 Ag^{-1} and b) rate performance under different charge/discharge rate [100]. c) Schematic diagram of new confuguration of DIBs with graphite brushed over one side of separator and aluminum sputtered over graphite and the other side of separator [194]. d) Rate performance of new configuration-constructed DIBs [194]. e) EIS of new configuration-integrated DIBs and conventional DIBs [194]. f) SEM cross-section image of graphite-aluminum electrode [194].

deliver a superior rate performance and cyclic stability, with 97.8 mA $h \cdot g^{-1}$ and 87 mA $h \cdot g^{-1}$ capacity delivered at high rate of 10C and 50C separately when cycled between 3 V and 5.3 V and over 80% of initial capacity remained after 10000 cycles when cycled between 3 V and 5 V at high rate of 10C [191]. In full cell test with Al replacing Li metal as negative electrode material, the superior performance is reserved, with \sim 95 mA h·g $^{-1}$ capacity delivered at high rate of 10C when cycled between 3 V and 5 V and barely capacity decay after 500 cycles [191]. Besides, a new configuration of cells is designed as shown in Fig. 15c. To be specific, positive electrode active materials (graphite) are brushed over one side of separator and aluminum is magnetron sputtered over deposited positive electrode materials and the other side of separator as current collector. The assembled full cells deliver excellent rate performance. Almost no capacity decay is noticed when charging rate increase up to 150C, delivering a discharging capacity of 116 mA h·g⁻¹ (Fig. 15d). In addition to the porous structure of aluminum negative electrode, the increased conductivity by using aluminum as both current collector and negative electrode active materials and decreased contact impedance between are assumed responsible for the excellent rate performance, as noticed from EIS when compared with regular DIBs and SEM images (Fig. 15e,f) [194].

As solutions for solvent co-intercalation, the most direct way to abate

the phenomenon is to reduce the ratio of ethylene carbonate (EC)/PC in electrolytes or apply other solvents instead [195,196]. The other way is to artificially form even and protective interphases on the positive electrode by decomposing electrolyte, as proven feasible on negative electrode side of LIBs [197,198]. For instance, in a half cell configuration (Li metal//graphite) with 1 M LiPF₆/EMS as electrolyte, graphite positive electrode is pre-charged/discharged at 100 mA g⁻¹ for 5 cycles within potential range of 0.3 V-2.0 V. Afterwards, a layer of SEI is formed on graphite surface with average thickness of 8-10 nm which can be noticed by TEM and XPS (Fig. 16a-c). With SEI protection, improvement over cyclic stability is significant, with ~96% capacity retention after 500 cycles under the upper cut-off potential of 5 V and current density of $200\,\mathrm{mA\,g^{-1}}$ (Fig. 16d). As comparison, the capacity of unmodified graphite quickly decays to ~50% after 150 cycles (Fig. 16d) [199]. However, the interphase prepared totally relying on solvent/additive decomposition has one shortcoming, that is, severe volume expansion brought by anion intercalation is easy to deteriorate its structure [154, 200]. A robust coating of Li₄Ti₅O₁₂ (LTO) on graphite surface is proven a feasible way to further improve cyclic stability. LTO has relatively good electrochemical stability under high potential and mechanical properties, so it could efficiently avoid the exfoliation of graphite positive electrodes in DIBs [200-202]. Besides, LTO possesses Ti⁴⁺ on surface which could

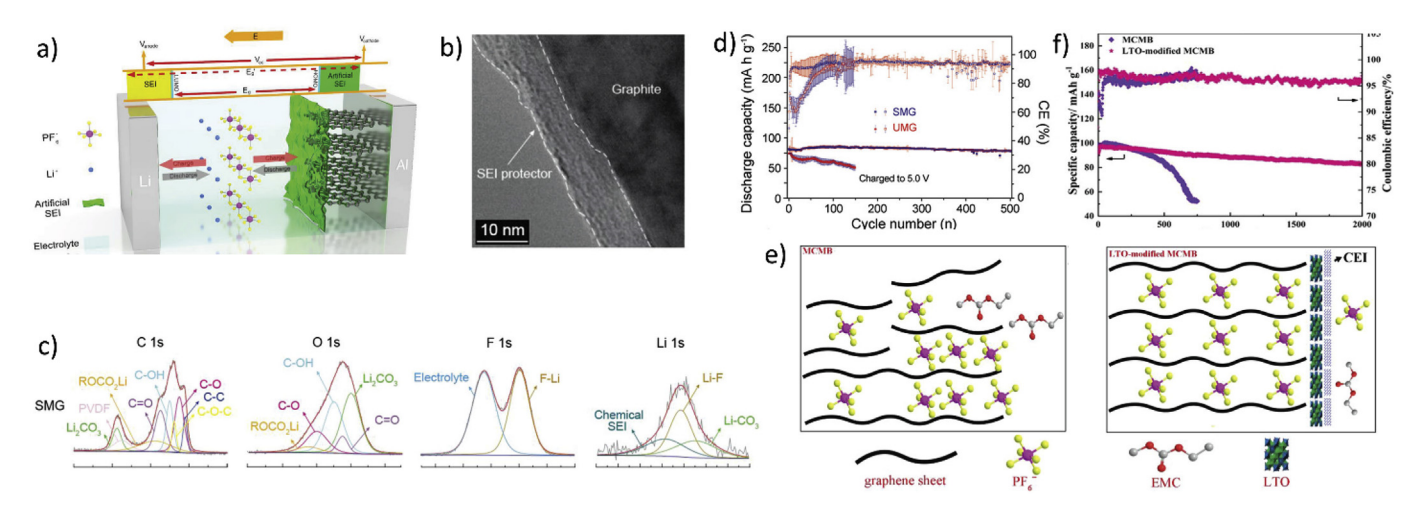


Fig. 16. a) Schematic configuration of DIBs with SEI layer artificially formed on the surface of graphite positive electrode [199]. b) TEM image of SEI layer on the graphite positive electrode surface [199]. c) XPS characterization for surface-forming SEI layer composition with C 1s, O 1s, F 1s, Li 1s peaks [199]. d) Cyclic stability comparison between surface modified graphite (SMG) and unmodified graphite (UMG) with upper cut-off potential of 5 V [199]. e) Schematic diagram of protection effect of CEI/LTO coating on graphite positive electrode [200]. f) Cyclic stability comparison between pristine MCMB graphite and LTO-modified one at the rate of 1C [200].

assist catalyzing ring-opening process of solvent sulfolane (SL) and turn it SL· radicals [203-205]. Then those radicals become electro-oxidization-resistant substance through certain polymerization process [206]. The formed CEI on LTO would play the role of de-solvation for anions and further protect graphite from structural collapse (see Fig. 16e). With CEI-LTO coated MCMB graphite as positive electrode, MCMB as negative electrode and 1 M LiPF₆/EMC:SL (1:4, V:V) as electrolyte, the cells exhibits excellent cyclic stability, with over 85% capacity retention after 2000 cycles at 1C (shown in Fig. 16f). In contrast, merely 53.6% capacity is remaining after 750 cycles for pristine MCMB graphite-positive electrode-based DIBs (see Fig. 16f) [200]. Overall, artificial CEI layer has been evidenced for its feasibility to inhibit solvent co-intercalation but it is not perfect. De-solvation is expected to happen outside the CEI layer, which increases the potential barrier for intercalation. Consequently, few ions could intercalate into graphite in a given potential range, in turn, the discharging capacity is reduced [82,200].

3.2. Novel positive electrodes

Due to the limitations of graphite, a great amount of efforts are put on finding alternative positive electrode materials for DIBs. The major options are nestled on redox reactive organic compounds because they could adsorb anions via the charge state change on active organic groups or moieties or the valent state change on transition metal centers [207–210]. Their mutual advantages like structure/property diversity, flexibility, element abundance, eco-friendliness, low mass density and great potential towards high energy density make them promising positive electrode materials in DIBs and endow them great potential to meet the demand of future energy storage devices [210]. Besides, some other materials like nitrogen-doped porous hard carbon [211] and coronene [212] are also tried as positive electrodes in DIBs and present some competitive performances. In the following section, novel positive electrodes proposed as alternative for graphite are categorized and summarized, followed by their properties and performances in DIBs.

Metal organic frameworks (MOF) with porous lattice structures are proven practicable as positive electrode materials for DIBs. As known, anions bring large volume change to graphite during intercalation, which has a negative effect on cells' overall stability and reversibility [81]. In contrast, for MOFs, post-synthetic modification has a strong impact on the pore size, which allows them to accommodate large anions without dramatic volume change [97]. To note, the most important structure motif for MOF is to get a short distance between redox-active metal

centers and no interruption in the crystal. Selection on the metal center should be careful as it determines both the working mode (p-type or n-type) and the electronic conductivity of the MOF materials [97,213]. Besides, the gravimetric densities of redox site could be improved through increasing the linker topicity [97]. For example, Fe₂(dobpdc) (dobpdc⁴⁻=4,4'-dioxidobipenyl-3,3'-dicarboxylate) could be electrochemically oxidized to Fe₂(dobpdc)A_x (A refers to the intercalated anions such as BF₄, PF₆, TFSI⁻ and x stands for the number of anions in the products) [97]. The framework of this material has hexagonal channels in which five oxygen-coordinated Fe²⁺ ions share their vertices in infinite 1D chains (Fig. 17a). When cycled in a half cell with electrolyte of 0.6 M NaPF₆/EC:DMC (3:7, W:W) between 2 V and 3.65 V, Fe₂(dobpdc) delivers an initial discharging capacity of ~95 mA h·g⁻¹ and displays a reversible and stable cycling, with ~90% capacity retention after 50 cycles. By comparing the discharging voltage profiles of several materials in Li- and Na-electrolyte system as shown in Fig. 17b, it is obvious to observe a linear decrement in the reduction progress for $Fe_2(dobpdc)(PF_6)_x$ (0.21 < x < 2) while other materials like $FePO_4$ and graphite show one or more plateaus. At the same time, its operating voltage is lower than graphite positive electrode. The decreased cut-off voltage benefits to choose a stable electrolyte by avoiding the decomposition of electrolytes but it also leads to an unsatisfying energy density with extra consideration of its low theoretical capacity (\sim 140 mA h·g⁻¹) [97]. Another type of MOF material, Cu(TCNQ) (TCNQ = 7,7,8,8-tetracyanoquinodimethane), is also applied as positive electrode material in DIBs [214]. It possesses a layer structure with metal centers Cu surrounded by 4 N-atoms from TCNQ anions (see Fig. 17c). In half cell configuration with 1 M LiPF₆/EC:DMC (1:1, W:W), Cu(TCNQ) shows high initial capacity (\sim 160 mA h·g $^{-1}$) but inferior cyclic stability between 2.4 V and 3.9 V vs. Li/Li+ and the situation gets reversed when increasing lower cut-off potential to 3.4 V vs. Li/Li⁺. This can be ascribed to the dissolution of active materials into electrolyte under potential of 2.6 V as confirmed by results from CV, XPS and XRD. Therefore, some strategies like changing components of electrolytes and modification of Cu(TCNQ) at low potential (<2.6 V) are needed for maintaining the high capacity and stability of active materials [214].

Another major category of positive electrode material to replace graphite in DIBs is the p-type organic radical compounds. Among them, nitrogen-based organics have been reported most frequently. For example, polytriphenylamine (PTPAn) could be oxidized and nitrogen atoms lose their electrons, then PF_6^- anion will be adsorbed on the positive N^+ sites for electric neutrality. In the discharging process, adsorbed

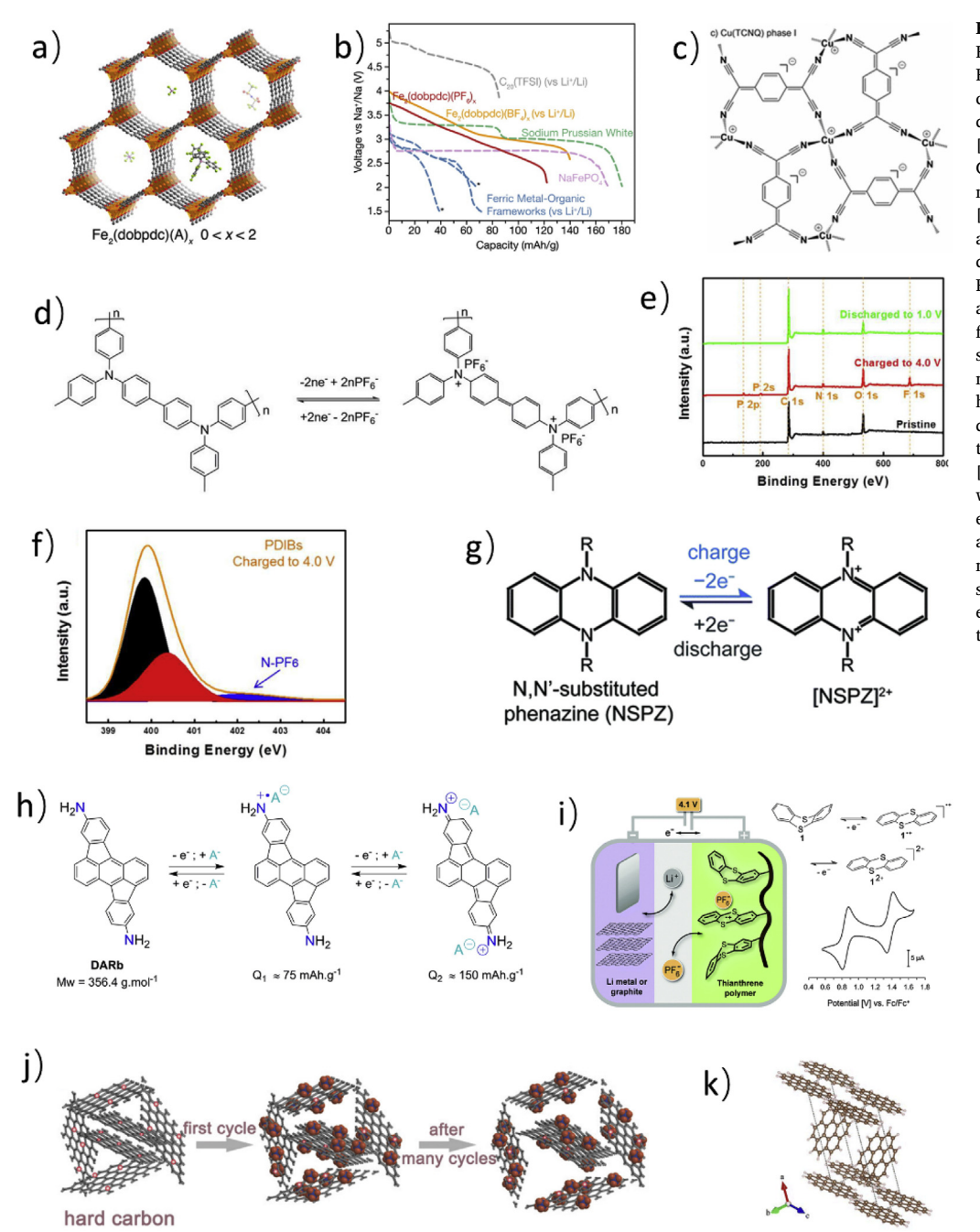


Fig. 17. a) Structural framework of Fe2(dobpdc). b) Comparison Fe₂(dobpdc)(PF₆)_x discharge profile compared to those of other electrodes discharged at their maximum capacity [97]. c) Structural framework of Cu(TCNQ) [214]. d) The reaction mechanism of PTPAn positive electrode [215]. e) PTPAn's XPS spectra collected at different electrochemical states, the detected characteristic peak from P and F reveal the successful anion insertion and f) high resolution XPS of N 1s. It further supports the anion insertion as speculated [216]. g) Reaction mechanism of NSPZ positive electrode [217]. h) Proposed two-stage redox reactions in diamino-rubicene electrodes and their theoretical capacities shown below [208]. i) Schematic of a type of DIBs with a thianthrene polymer positive electrode and its working mechanism and the redox CV curves [98]. j) Schematic illustration of adsorption/desorption mechanism of NPHC positive electrode [211]. k) Schematic illustration of coronene crystal structure [212].

anions are released and the positive nitrogen cations accept the coming electrons (Fig. 17d) [215]. To further verify the speculated working mechanism, the full survey XPS spectrum (Fig. 17e) finds the new additional peaks around 135, 192 and 687 eV when the pristine electrode is charged to 4 V, which correspond to P 2p, P 2s and F 1s, respectively, suggesting the PF₆ anion adsorbed on the PTPAn chain [216]. After discharging, the peaks from P disappears, and F characteristic peak becomes weak, meaning PF₆ anions are released. Besides, the high-resolution N 1s XPS spectrum (Fig. 17f) reveals that a broad peak situates at 402.3 eV at the charging state and disappears again when electrode goes back to discharging state. This peak refers to the interaction between N⁺ and PF₆ anion. The detailed analysis verifies the proposed mechanism for PTPAn positive electrode is reasonable and is supported further by the atom ratio from TEM. The PTPAn-based half cells show stable cycling but deliver only 71 mA $h \cdot g^{-1}$ capacity between 2 and 4 V at the rate of $100 \, \text{mA} \, \text{g}^{-1}$ [216]. For organic redox materials,

one way to improve capacity is to increase the ratio of active sites to overall mass [217]. Based on the rule, a new material called 5,10-Dihydro-5,10-dimethyl phenazine (DMPZ) is synthesized and applied as positive electrode material in DIBs [217]. This material is a phenazine with two nitrogen atoms methylated and is expected to donate two electrons in sequence as shown in Fig. 17g. Further DFT calculation supports the stability of the substance as electrons effectively delocalize after losing two electrons. As expected, the material delivers an initial capacity of 217 mA h·g⁻¹ of charging and 191 mA h·g⁻¹ of discharging for TFSI anions when cycled between 2.5 V and 4.1 V at the rate of 50 mA g⁻¹. However, [DMPZ]²⁺ is soluble in tetraethylene glycol dimethyl ether (TEGDME) solvent. The strategy of increasing salt concentration is proven an effective way to suppress the dissolution while other methods like surface modification or solvent replacement should also be tried to improve the stability [217]. In addition, amino groups could also act as redox center for reversible adsorption/desorption of anions. 5,12-diamino-rubicene (DARb), for instance, works through multi-electrons participated redox reaction on two amino groups (Fig. 17h) [208]. Extending rubicene's aromatic core could help stabilize unpaired electrons via delocalization, in turn, improving the reversibility/stability of redox reactions [208]. However, bulky rubicene offsets the contribution of two electrons reaction and make full cells deliver specific capacity of only 115 mA h·g $^{-1}$ (~75% of its theoretical capacity). And it also suffers relatively fast capacity degradation (75 mA h·g $^{-1}$ after 60 cycles).

Apart from the active center of nitrogen, sulfur in the organic chain also can work through redox reaction [98]. Fig. 17i shows the working mechanism of thianthrene in DIBs, in which thianthrene undergoes a two-step oxidation process in the charging process. The reactive process is similar to PTPAn mentioned above, and two pairs of redox peaks are detected by CV curves. However, this material is just tested referring to the first electron reaction at the lower voltage and delivers a specific capacity around $62\,\mathrm{mA}\,\mathrm{h\cdot g^{-1}}$. The most important thing is the voltage plateau at 4 V that is similar to the voltage profile of LiCoO2. If there is a stable electrolyte allowing for the reaction from the second electron, the specific capacity will double at least. The disappointing issue is that the cycling capacity is not stable and decays sharply, though there presents a slight increase in the first 10 cycles. The fast degradation is attributed to irreversible anion insertion and potential dissolution of active materials in the organic electrolyte [98].

Lastly, there are also some individual examples of novel positive electrodes for DIBs. The first one is the nitrogen-doped porous hard carbon (NPHC) which is synthesized through directly calcinating pyrrole monomer [211]. This material with N-doping on surface has several intrinsic advantages like i) adsorption/desorption mechanism which helps avoid the volume expansion brought by anion intercalation, ii) porous structure increases the specific area exposed to electrolyte which helps increase the capacity and also shortens the route for anion intercalation which benefits the rate performance. When tested between 1 V and 4.7 V in half cell, the material delivers an enhanced discharging capacity of 197 mA h·g⁻¹ and 100% Coulombic efficiency at the current rate of 100 mA g⁻¹ (Fig. 17j) [211]. Similarly, the carbon foam synthesized through facile carbonization process also works through the adsorption/desorption mechanism. In the half-cell test, this positive electrode material delivers a superior rate capability and cyclic stability with $\sim 110 \text{ mA h} \cdot \text{g}^{-1}$ capacity retained at high rate of 5 A g $^{-1}$ and almost no capacity decay at the rate of 1 ${\rm A\,g^{-1}}$ over 500 cycles [218]. Another one is the coronene crystals, a polycyclic aromatic hydrocarbon (PAH) solid material, exhibiting a monoclinic structure (Fig. 17k) in which molecules condense together by van der Waals forces and the lattice parameters are a=16.1, b=4.7 and c=10.1 Å [212]. It is an anion-intercalation-type positive electrode with a displayed discharging voltage plateau around 4 V and the first charge capacity is ~60 mA h·g meaning 0.68 PF₆ anion inserted into one coronene. During charging process, the anions charge carriers insert in between the (111) and (200) planes, causing an expansion along a direction. The transition tracked by ex-situ XRD. To be specifically, the (001) peak at 9.2° stays at the same position in the charging process, but peak (200) around 11.7° shifts towards a lower angle. A structure expansion along a direction is 0.08 Å, at the same time the shifted peak presents an increased intensity with further oxidation from point III to IV. To note, as the value of cycles gets bigger, it is found that anion intercalation causes a decrease of crystallinity evidenced by the weakened XRD peak intensity in the re-insertion. Unlike graphite, the molecules are not connected through strong co-valent bond, therefore, they are easy to pulverize during large anions intercalation and can't maintain the integrated crystalline structure. This may partially account for the loss of crystallinity during discharging processes [212].

Overall, the graphite is the most frequently used material for both electrodes in DIBs which benefits from its properties including redox amphotericity, high mechnical strength as well as superior electric conductivity. The layered structure allows the storage of charge carriers step

by step in so-called the staging mechanism, which could be observed through some characterization techniques like CV, XRD and Raman spectroscopy. However, the graphite positive electrode suffers from some serious problems on storing anions including the limited capacity, cyclic stability and rate capability influenced by solvent co-intercalation, anion types and graphite intrinsic properties. Accordingly, some strategies are developed to deal with these issues. Firstly, it has been proven that smaller particle size, more exposure of edge planes, high crystalline, defect/dopant-free graphite has the optimal capacity for storing anions. The rate capability of graphite materials could be improved by applying low diffusion energy barrier anions like AlCl₄ and decreasing the particle size to shorten the diffusion distance of anions. To deal with the problem of solvent co-intercalation, the feasible methods are to avoid the use of EC/PC solvents or to construct protective electrolyte-graphite positive electrode interphase. In addition, some efforts are also devoted to find alternative materials for graphite to achieve potentially higher electrochemical performances. At the current stage, the optional materials majorly lie on adsorption/desorption mechanism which contain the doped carbon materials and p-type organics and other individual examples like coronene. Despite of relatively poorer performances in comparison to graphite counterparts, they still exhibit attractive features and show great potential for further development and application.

4. Negative electrodes

Selection on the negative electrode is also an important issue in DIBs because it co-determines the performance of cells (i.e. rate capabilities, cyclic stability, specific capacity, safety and so forth) with positive electrode material and other components in cells. Although the positive electrode materials are considered major bottleneck on enhancing cells overall performance due to limited capacity, yet the negative electrode materials still need to offer excess capacity to avoid the metal plating in the practical situation concerning the cells' safety risks and lifespan issues, termed as "capacity balancing" [219-223]. Hence, constantly exploring the high-performance negative electrode materials is quite necessary. For DIBs, most commonly used negative electrode material is the intercalation-type graphite due to its high stability/reversibility for cation intercalation/de-intercalation and high ionic/electric conductivity, but it suffers from the low Coulombic efficiency in first cycles because of the formation of SEI and low capacity due to limited crystallographic sites. To improve the performances, a series of new negative electrodes are proposed as replacement for graphite. It should be noted that working mechanism for negative electrode material has no difference between DIBs and rocking-chair batteries, namely, storing and releasing cations during charging and discharging process. Hence, the novel negative electrode will be introduced based on well-established system of negative electrode materials in rocking-chair batteries with the sub-categories of intercalation-type, conversion-type, alloying-type adsorption/desorption-type which include some individual examples.

4.1. Intercalation-type negative electrodes

SEI formed on the surface of graphite negative electrode is composed of the reduced products from the electrolyte. SEI precipitated in the initial cycle would suppress the continuous decomposition of electrolyte and the co-intercalation of solvents with ions into graphite negative electrode due to its low electric conductivities and high ionic conductivities. However, SEI formation leads to the loss of Coulombic efficiency in the first cycle and reduced capacity in following cycles due to the consumption of salts/solvents in electrolyte [224]. The situation gets worse when considering that electrolytes are also counted as active mass in DIBs [104]. A feasible solution is to adjust the lower cut-off potential to a value higher than SEI formation potential of electrolytes [224]. And it is necessary to find some compatible negative electrodes which could fully release their performance with enhanced lower cut-off potential [225–228]. For instance, orthorhombic Nb₂O₅ has two reduction peaks

at 1.6 V and 1.2 V, corresponding to the redox pairs of Nb⁵⁺/Nb⁴⁺ and Nb⁴⁺/Nb³⁺ separately which could be noticed from its CV curve. When cycled between 1 V and 3 V at rate of $100 \, \text{mA} \, \text{g}^{-1}$ in a half cell, Nb_2O_5 presents ~90% Coulombic efficiency and delivers a charge capacity of 165 mA h·g⁻¹ in the second cycle [229]. Similarly, spinal-structure Li₄Ti₅O₁₂ (LTO) with the redox pair Ti⁴⁺/Ti³⁺ works at higher potential (~1.55 V vs. Li/Li⁺) than traditional carbon negative electrodes (~0.1 V vs. Li/Li⁺) [230–232]. Besides, small volume expansion during lithium-ion intercalation/de-intercalation bestows LTO another safeguard for high reversibility/stability [230,233]. Even if the SEI layer forms on its surface, SEI could be stable as there is no strain to deteriorate it. However, high working voltage and intrinsically low discharge capacity bring issue of energy density. The full cells using LTO/graphite as negative/positive electrodes present a low open circuit potential between 3.2 and 3.6 V and deliver only $54.9 \,\mathrm{mA \, h \cdot g^{-1}}$ discharge capacity with 99% Coulombic efficiency when cycled between 1.5 V and 3.6 V, which are all inferior to graphite-negative electrode-based DIBs [96]. For Nb₂O₅, full cells using it as negative electrode and KS6 graphite as positive electrode also merely exhibit a discharge capacity of ~57 mA h·g⁻¹ at the rate of 1C when cycled between 1.5 V and 3.5 V [229]. Therefore, some new chemistries (i.e. conversion, alloving, etc.) are necessary to replace the intercalation mechanism for negative electrode materials in DIBs to achieve higher energy density.

4.2. Conversion-type negative electrodes

Conversion-type negative electrodes, usually transition metal oxides and sulfides, react with ${\rm Li}^+$ to form ${\rm Li}_2{\rm O}/{\rm Li}_2{\rm S}$ and element-state metal inside (see Fig. 18a) [135]. This type of negative electrodes is promising because they could deliver much higher theoretical capacity (e.g. 890 mA h·g $^{-1}$ for ${\rm Co}_3{\rm O}_4$) than conventional graphite negative electrode [234,235]. However, this type of materials has several drawbacks that are necessary to overcome like i) large potential hysteresis during cycling, ii) low Coulombic efficiency in initial cycles, iii) fast capacity decay and iv) poor rate performance [46,236]. The formation of poor electric-conducting products, dramatic volume expansion and SEI layer deterioration/reproduction are assumed responsible for the problems

[236,237]. Reduction of particle size and increment of contact area between particles and electrolytes are seen as a feasible way to improve the overall performances of conversion-type materials [238]. As mentioned above, these methods not only shorten the diffusion route of ions but also release the strain for volume expansion. For instance, nanosheet-structure Co₃O₄ is grown on carbon fiber paper (CFP) and co-form the negative electrode material Co₃O₄/CFP in DIBs. In the half cell test, Co₃O₄/CFP presents an initial Coulombic efficiency of ~87.5% and the value rapidly increase to 98.6% after the third cycle. Besides, the cells show the rate capability of $385\,\mathrm{mA}\,\mathrm{h}\,\mathrm{g}^{-1}$ discharge capacity remained at rate of 500 mA g⁻¹ and stability with 90% capacity retained after 40 cycles at rate of 200 mA g⁻¹ [235]. In addition, conductive coating on surface could help further improve the rate performance and cyclic stability as coating not only decreases the resistivity for charges' motion but also helps maintain the active materials' integrity by providing high mechanical strength. For instance, a hollow sphere material composed of vertically grown MoS₂ nanosheets and surface coating of N-doped carbon is synthesized through sulfidation of solid Mo-glycerate (MoG) and thereafter the annealing with bovine serum albumin to precipitate N-rich carbon coating on surface (Fig. 18b and c). To evaluate the effect of conductive coating, uncoated samples (denoted as MoS₂ HHSs) are compared with coated samples (denoted as MoS₂@NC HHSs) through galvanostatic charge/discharge test (Fig. 18d) and rate capability test (Fig. 18e). The results indicate the significant improvement in both cyclic stability and rate performance. Applying this material as negative electrode, expanded graphite as positive electrode and 1 M NaPF₆/EC: DMC:EMC (1:1:1, V:V:V) as electrolyte, the cells present good rate performance and reversibility as capacity changes from 92 mA h·g⁻¹ to $45 \,\mathrm{mA}\,\mathrm{h\cdot g}^{-1}$ and then to $87 \,\mathrm{mA}\,\mathrm{h\cdot g}^{-1}$ when rate varies from $200 \,\mathrm{mA \cdot g^{-1}}$ to $2000 \,\mathrm{mA \, g^{-1}}$ and return to $200 \,\mathrm{mA \, g^{-1}}$ [239]. Another example is a composite negative electrode with MoS2 nanosheets grown on surface of nanofiber MoS2 nanofiber/carbon composite followed by carbon coating on surface (denoted as (MoS $_2$ /carbon fiber)@MoS $_2$ @C) (Fig. 18f). Owing to the 3D interconnected structure and good conductivity of the carbon fiber substrate, the half cells deliver superior rate performance and cyclic stability within voltage window of 0.01-2.5 V with over 233 mA h·g⁻¹ discharge capacity at high rate of 10C and over

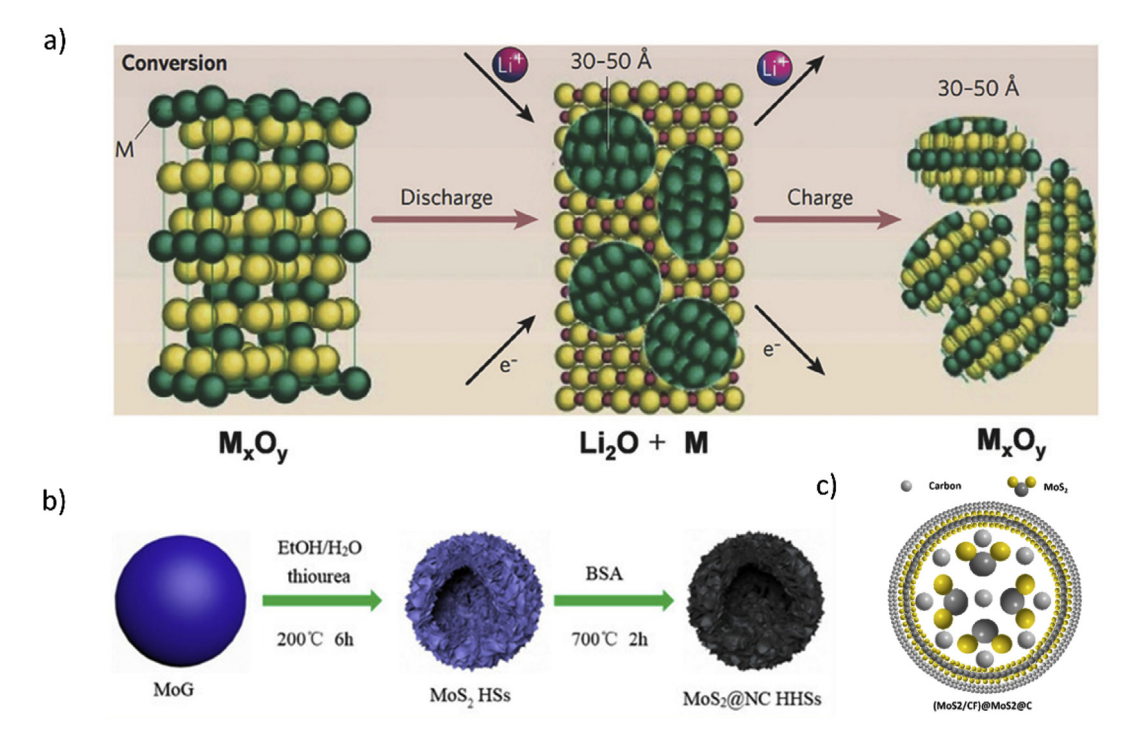


Fig. 18. a) Schematic diagram of the mechanism for conversion-type negative electrodes [135]. b) Schematic diagram of synthesizing $MoS_2@NC$ HHSs [239]. c) Schematic diagram of multi-layer (MoS_2 /carbon fiber)@ $MoS_2@C$ material [240].

90% capacity retention relative to second cycle after 200 cycles at a rate of 100 mA g $^{-1}$ (Fig. 18g,h). Furthermore, the full cells with graphite as positive electrode and 1 M NaPF₆/EC:DMC (6:4, V:V) as electrolyte also possess high capacity retention even at a high rate (about 100 mA h·g $^{-1}$ at 0.5 A g $^{-1}$ within the potential window from 2.0 to 4.7 V) [240].

4.3. Alloying-type negative electrodes

Alloying-type negative electrodes work through the electrochemical alloying between element negative electrode and metal cations from electrolyte (e.g. Si–Li [241,242], Sn–K [102,243], Sn-Na [244,245]). This type of negative electrodes has received increasing attention due to their intrinsic outstanding ability for storing metal cations (e.g. 993 mA h g $^{-1}$ with the phase of AlLi) and superior electrical conductivity (e.g. $3.50\times10^7\,\mathrm{m}^{-1}\,\Omega^{-1}$ for Al and $1.25\times10^7\,\mathrm{m}^{-1}\,\Omega^{-1}$ for Ni) [246,247]. Designing these metals as both current collector and hosting material is currently an active field, which is a convenient way to increase the ratio of active material, in turn increasing the energy density of full batteries [105,106]. For instance, Sn serving as both current collector and hosting material is applied in Na-ion-based DIBs (a schematic diagram is shown in Fig. 19a) with EG used as positive electrode material. The mass ratio of graphite positive electrode in the DIBs (48.9%) is higher than that of LiCoO2 positive electrode in LIBs counterparts (36.4%) with an equal

amount of stored capacity. The energy density of the tin-graphite cells has achieved $144 \, \text{Wh} \cdot \text{kg}^{-1}$ at $150 \, \text{W} \, \text{kg}^{-1}$, which is comparable to some commercial LIBs [195].

However, the disadvantages of those alloying-type metal negative electrodes are also serious. Firstly, the alloying reaction occurring below 1 V could cause the SEI formation, which usually accompanies the substantial loss of Coulombic efficiency in initial cycles [248]. Secondly, the type of metallic negative electrodes suffers from the inferior rate capability and cyclic stability because of the severe volume changes during charge/discharge process (e.g. 420% expansion by forming $Na_{15}Sn_4$ alloy and 96% for LiAl) [195,244,248]. Further, the SEI layer formed in first cycle faces periodic destruction/reformation due to severe volume expansion followed by the constant decomposition of electrolytes. The process leads to the loss of Coulombic efficiency or even the death of cells in a worse situation [248–252]. Hence, several methods like surface modification and structure design are incorporated into the design of metal negative electrodes (especially Al) in DIBs which is shown in Fig. 19 b-q.

Firstly, surface modification improves cyclic stability by offering enough mechanic strength to suppress the volume expansion of metal negative electrodes. For instance, introducing FEC additive into ionic liquid-based electrolytes is proven helpful in modifying the characteristics of the SEI layer (Fig. 19b) [105]. The modified SEI layer would

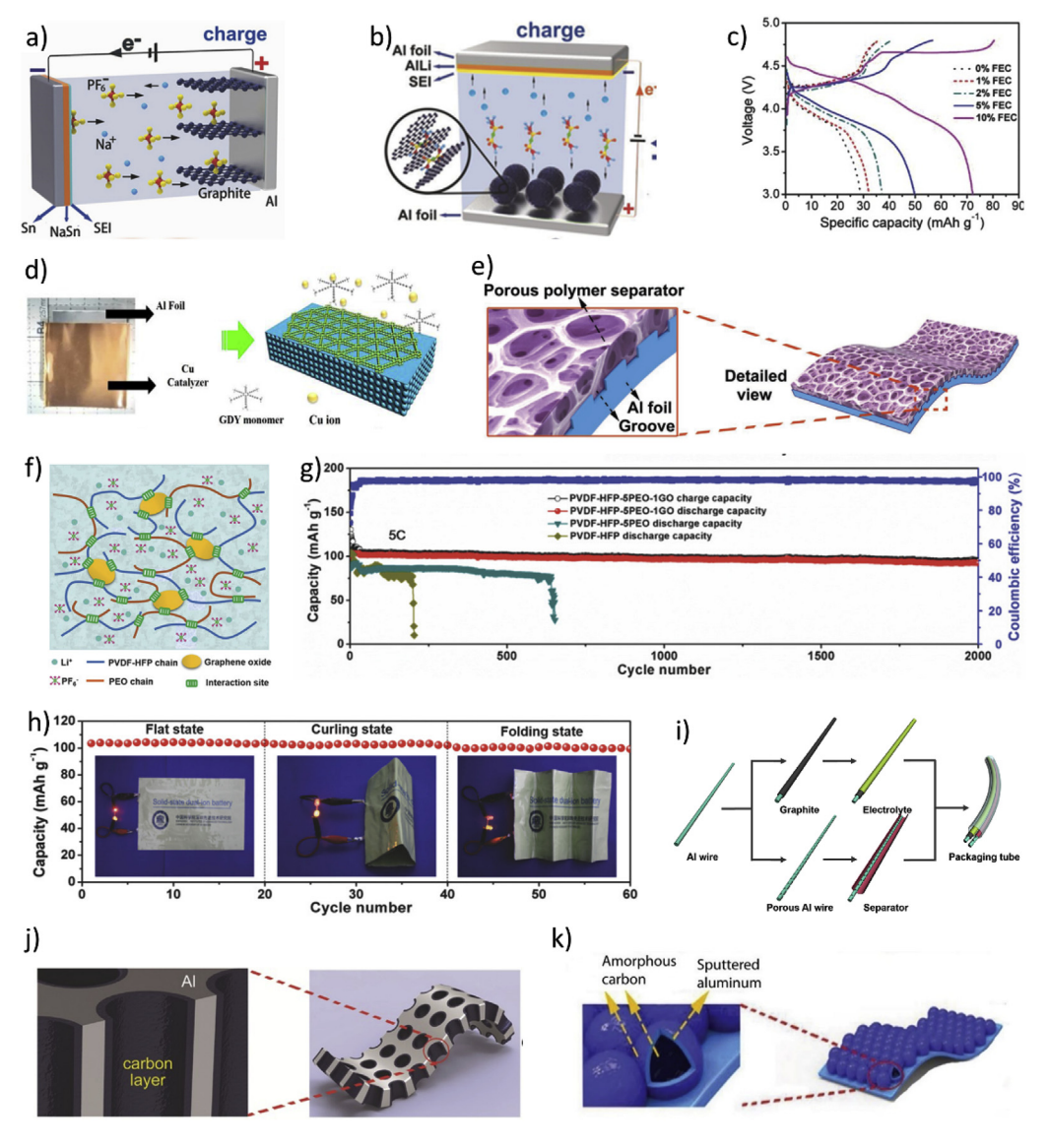


Fig. 19. a) Schematic diagram of Snbased negative electrode in Na-DIBs [195]. b-c) Schematic diagram of Al-based negative electrode for Li-DIBs and influence of FEC additives on cycling profile [105]. d) Schematic diagram of the synthesizing process for GDY coating on aluminum foil [247]. e) Schematic diagram of the integrated multifunctional electrode (ME) [253, 254]. f-h) Schematic diagram of PHPG with a further addition of GO and PEO, its positive influence on long time cyclic stability and full cells' capacity retention/cyclic stability when folded in different ways [255]. i) Schematic diagram of fabrication process and final performance of the novel flexible cells [256]. j) Schematic illustration of carbon coated 3D porous Al negative electrode [257]. k) Schematic illustration of bubble-sheet like Al/C negative electrode [258].

suppress the pulverization of Al negative electrode during cycling and help improve the cyclic stability drastically (Fig. 19c) [105]. With mesocarbon microbeads (MCMB) as the positive electrode material, the full cells exhibit outstanding cyclic stability, with almost no capacity decay when cycled at 0.5C for 300 cycles. To note, the cells deliver high energy density, reaching 221 Wh·kg $^{-1}$ at a power density of 109 W kg $^{-1}$, which is comparable to most of commercial LIBs [105]. Similarly, a thin graphdiyne (GDY) is in-situ grown on surface of commercial Al foil as protection layer through process shown in Fig. 19d. The improvement over stability is also noticeable. To be specific, over 88% capacity with Coulombic efficiency of over 96% remains after 450 cycles at rate of 1C while bare Al-based full cells fail after merely 80 cycles [247].

To note, coating Al negative electrode with certain insulating polymers not just increases the cyclic stability, but also incorporates more functions into the composite materials (active material, current collector separator). For example, poly (vinylidene fluoridecohexafluorpropylene) (PVDF-HFP) which has high ionic conductivity, large pores for holding electrolytes and feature of electric insulating for preventing short circuit is reported several times as multifunctional coating on aluminum surface [253,254]. As seen in Fig. 19e, the porous and flexible polymer coating closely adheres to the Al negative electrode which could effectively hinder severe pulverization and surface cracking of the Al negative electrode after the repeated alloying and dealloying process [253,254]. In one of the studies, the cells display satisfactory performance with 92.4% capacity retention after 1000 cycles at 2C and with only 20% capacity reduction when running at 10C [254]. With further addition of poly(ethylene oxide) (PEO) and graphene oxide (GO) and forming so-called PVDF-HFP-5PEO-1GO copolymer (PHPG), the arrangement of the pores and the mechanical strength are adjusted and improved to some extent (Fig. 19f). Consequently, the cyclic stability gets enhanced to a higher level, reserving 92% capacity after ~2000 cycles when cycling at high current density of 500 mA g⁻¹ (Fig. 19g). Besides, the composite material possesses high flexibility. When tested in a pouch cell, cells show good cyclic stability and capacity retention when folded in different ways as shown in Fig. 19h [255].

In addition to surface coating, constructing a porous or hollow structure is also found to be helpful to inhibit metal pulverization through releasing the expansion/contraction stress. In one work [256], aluminum wire with average diameter of 0.3 mm is pre-etched by electrochemical method to create porous structure. The positive electrode is made by dip-coating aluminum wire into graphite ink. Thereafter, the prepared positive and negative electrode wires are sealed within the heat-shrinkable tube with electrolyte-wetted separator (Fig. 19i). When cycled between 3 and 4.95 V in electrolyte containing 4 M LiP-F₆/EMC:VC, the flexible cells exhibit high discharging capacity with up to \sim 145 mA h·g $^{-1}$ at scan rate of 1C. Benefiting from porous structure of aluminum wire, superior long-term cyclic stability and outstanding rate performance are achieved with merely 10% capacity loss after cycling for 200 cycles at 1C and with \sim 80 mA h·g⁻¹ capacity remaining at high scan rate of 5C. It should be noted that this special structure for assembling DIBs enables them good flexibility with ~87.5% discharge capacity retention after bending from 0° to 360° for 200 cycles [256].

Furthermore, some works report the combination of above mentioned two protection methods to modify metal negative electrode [257,258]. For instance, Al foil is made into a porous structure via electrochemical etching and amorphous carbon is coated on the surface through calcinating the polymer attached in former steps (Fig. 19j). With the unique structure, the cyclic stability is greatly improved as noticed from galvanostatic charge/discharge profile at a rate of 2C in comparison to untreated Al foils and porous Al foil without carbon coating [257]. In another work, hollow sphere Al with carbon coating on its surface is synthesized as negative electrode material in DIBs (Fig. 19k) [258]. The special structure not just improves full cells' cyclic stability (only 1% capacity decay with over 95% Coulombic efficiency after 1500 cycles at 2C by buffering the harmful volume change but also offers an outstanding rate capability via shortening the diffusion route of Li⁺ ions

 $(98 \text{ mA h} \cdot \text{g}^{-1} \text{ discharge capacity at 5C})$ [258].

4.4. Adsorption/desorption-type negative electrodes

Storing cations through adsorption/desorption mechanism contributes to another important branch of negative electrode materials in DIBs. They have several advantages that make them more attractive than the other types of materials. The surface storage mechanism allows the facile uptake/release of cations from/into the electrolytes, which avoids the sluggish transfer and reaction rate of cations in conventional intercalation-type materials. The intriguing feature is helpful to improve cells' overall electrochemical performances like rate capability and longterm cyclic stability. The materials powered by the mechanism could be categorized into several types. The first type is the carbonaceous materials (e.g. hierarchical porous amorphous carbon [259], activated carbon [260], carbon foam [218]), which adsorb the cations through so-called Electric Double Layer Capacitive (EDLC) behavior. Typically, the materials are highly porous and possess large surface area which help further strengthen the capacitive behavior and allow the fast adsorption/desorption of the large cations. For example, a type of carbon foam synthesized by carbonization of sodium ascorbate has large surface area of 1126 m² g⁻¹. In half-cell test, the material exhibits superior rate capability with \sim 100 mA h·g⁻¹ capacity remained at high rate of 5 A g⁻¹, and great cyclic stability with merely 18% capacity loss after 500 cycles at high current density of 1 A g⁻¹ [218]. Another important type is the redox active organics, which contain n-type functional groups for reversible electrochemical reactions. To note, unlike metal and metal oxide/suifide negative electrodes, organics are majorly composed of abundant resources which cut their cost for synthesizing and render these materials' good sustainability [215]. Besides, organics have high diversity over structure and composition, hence the rate capacities have great potential to improve [261]. In comparison, intercalation-type negative electrodes have limited space for improvements, especially the specific capacity. The works reporting the organic negative electrode in DIBs are very limited so far. One work reports the application of n-type polymer poly(anthraquinonyl sulfide) (PAQS) as negative electrode in sodium-ion-based DIBs. The reversible redox reactions are shown in Fig. 20a. The two-electron reactions correspond to the theoretical capacity of \sim 224 mA h·g⁻¹ and the average discharging potential is around 1.8 V vs. Na/Na+ which is high enough to avoid the reduction of electrolytes. In the half cell test, it shows superior cyclic stability and rate capability, with almost no capacity decay at the rate of 8C for 200 cycles and over 160 mA h·g⁻¹ capacity remaining at high rate of 30C. The full cells with PAOS as negative electrode, p-type polymer polytriphenylamine (PTPAn) as positive electrode and saturated NaPF₆/1,2-dimethoxy ethane (DME):1,3-dioxolane (DOL) (1:1, V:V) as electrolyte possess an open circuit potential of ~1.8 V and also deliver superior performances. At a rate of 8C, over 85% capacity remains after 500 cycles. Relative to 1C, over 73% capacity retention is observed at a high rate of 32C [215]. In addition, some organics possess n-type and p-type features simultaneously, which means, they could act as both negative and positive electrodes in full cells. For instance, 4,4'-(phenazine-5,10-diyl)dibenzoate anion (abbreviated as PZDB) has both positive electrode-active moieties (phenazine) and negative electrode-active moieties (benzoate) in its structure which allows it work as electrons donors as well as electrons acceptors as shown in Fig. 20b. Further, PZDB anions combined with two lithium ions and the salt (denoted as PZDB-Li₂) are used as both electrodes in symmetry cells. The energy states of materials during redox reactions are displayed in Fig. 20c. To note, HOMO and LUMO of the material separately lie in those two types of moieties, which allows the redox reactions to occur independently. In addition, energy differences between reactants and products in the redox reactions are relatively small, so low energy is needed to activate those reactions [261,262]. With the bipolar materials as both electrodes and 1 M LiPF₆/EC: diethyl carbonate (DEC) (1:1, V:V) as electrolyte, the symmetry cell is constructed with open circuit potential of 2.5 V. A stable discharge capacity

Fig. 20. a) Two step reaction mechanism of PAQS [215]. b) Redox reaction mechanism of PZDB anion, c) energy states of reactants and products in redox reactions of PZDB-Li₂ [261].

of \sim 53 mA h·g⁻¹ (based on total mass of electrodes) is obtained at 1C with Coulombic efficiency of 97%. Besides, the cells deliver an energy density of 127 Wh·g⁻¹ at a power density of 308 W g⁻¹ [261].

Intense research has been done on finding suitable alternative negative electrode materials for conventional graphite materials in DIBs to improve the overall performances. The intercalation-type materials like Nb₂O₅ and LTO exhibit stable cycling and have relatively higher featured working potential than graphite counterparts which help enhances the Coulombic efficiency by suppressing the SEI formation. However, they suffer from the low capacity due to the limited active sites in their structure. In comparison, the conversion and alloying chemistries exhibits much higher theoretical capacity, but they are confronted with one fatal problem of structure instability during cycling due to great volume change and derived problems like low Coulombic efficiency and poor cyclic stability. However, alloying-type materials have some other intringing features like great abundance in nature and superior electric conductivities which endow them great potential for future broad application. Furthermore, the metal electrodes could help cut the overall mass of the cells by acting multiple roles including the current collector and active material, which also meets the demands on light weight and high energy density for future rechargeable batteries [195,253,254]. The cyclic stability could be improved through some strategies including the construction of robust SEI layer, surface coating and structure design. Lastly, the adsorption/desorption-type materials are also received a lot of attention since they are kinetically unlimited and majorly composed of nature-abundant elements and they have great potential for high rate capability and cyclic stability.

5. Electrolytes

The electrolyte plays a crucial role in cell performance and the electrolyte selection is a complicated process with trade-offs that sometimes must be made [118]. In the DIBs system, a wide number of solvents, salts, and additives are to choose from in order to withstand high voltage of graphite-positive electrode-based DIBs and to achieve highly reversible/stable electrochemical behavior. At the same time, some other cation charge carriers within DIBs (e.g. Na⁺ [99], K⁺ [216], Zn²⁺ [113],Al³⁺ [100], NH⁴₊ [263]) are well studied and receive high expectation to replace conventional lithium charge carriers with the consideration of exhausting lithium resources and increasing cost of Li-DIBs [46]. In this section, strategies to deal with the high working voltage of conventional DIBs from the perspective of solvents will be classified and summarized. Besides, novel cation-based DIBs other than lithium will also be summarized here accompanied by some related background introduction.

5.1. Solvents

One of the core issues in DIBs is the compatibility between the electrolytes and superiorly high working potential. Similarly, conventional LIBs could also possess high voltage reaching 5 V when applying positive electrode materials like LiNi $_{0.5}$ Mn $_{1.5}$ O4 [264–266], LiCoPO4 [76,267] and Li $_{2}$ NiPO4F [76,268] and the history for studying electrolytes/additives compatible with these materials is longer than the systematic study on DIBs [269]. Hence, high voltage LIBs are good references for DIBs in selecting appropriate electrolytes for a reversible

cyclic process. Some strategies such as high concentrated electrolytes [270,271] and ionic liquid electrolytes [272] could be shared between each other to create a wide-enough electrochemically stable range. In the following parts, electrolytes in DIBs are categorized into three parts based on the type of solvents, specifically, organic solvents, ionic liquid and aqueous solvents in DIBs. Their properties, development history, methods for soothing the aforementioned problems will be introduced in detail below. To note, the properties of each type of electrolytes are summarized in Table 1 at the end of this session for the convenient reference of readers [273].

5.1.1. Organic solvents

Organic solvents are considered the most feasible and practical candidates for the future commercialization of DIBs, not only because of their long-studied history in LIBs but also due to their varieties, low cost. high ionic conductivity, ability to form SEI layer for protection and so forth [274]. However, a major challenge of using organic solvents within DIBs is the stability under high oxidizing potentials for the anion uptake into the graphitic positive electrode (above 4.5 V vs. Li/Li⁺), which is far beyond the upper limit of frequently used electrolytes in LIBs (\sim 4.3 V) [74,206,264,274,275]. Consequently, the working potential which is more negative than that of the organic electrolytes' HOMOs will cause the electrolyte to oxidize and decompose. Besides, other factors like stability of decomposition interphase layer on electrodes surface, ionic conductivity of electrolytes, wettability with electrodes and separator, thermal stability also influence the exhibited performances of the cells. Hence, constant efforts are devoted to tuning solvents/additives composition to improve performances with the basis of good cyclic stability/reversibility. Examples of the solvents/additives include PC [72, 276], EC [72,276], DMC [195,277], EMS [74], EMC [278], methyl propionate (MP) [279] and FEC [70,154,279].

Among them, EMC is one of the promising solvents as it is reported working better over some other electrolytes. It possesses high stability towards a reduction and low viscosity and so forth [280]. More importantly, it supports the smooth intercalation of PF_6^- anions into graphite positive electrode. For instance, when 1 M LiPF₆ with EMC was compared against 1 M LiPF₆ with PC, the results suggested that less energy is required for anions intercalation from electrolyte solutions containing EMC. Furthermore, the charge transfer resistance decreased (as measured

Table 1Characteristics of several types of electrolytes and their availability in the history of DIBs and high-voltage LIBs [273].

	*	
Solvent type	Advantages	Disadvantages
Sulfone-based solvents	High oxidative stability (e.g. 6.35 V vs. Li/Li ⁺ for SL) [278], moderate cost	High viscosity, high melting point
Fluorinated solvents	High oxidative stability (>5.2 V vs. Li/Li ⁺), low melting point, formation of stable SEI layer after decomposition, moderate cost	High viscosity, low ionic conductivity
Super concentrated electrolytes	High oxidative stability (e.g. 6.1 V vs. Li/Li ⁺ for 3.5 M LiPF ₆ /EMC [295]), high reductive stability, ability to inhibit Al corrosion, high energy/power density (for DIBs)	Relatively low ionic conductivity, increased cost relative to regular electrolytes, high cost
Ionic liquid	None volatility, inflammability, wide electrochemical-stable range (up to 5.5 V with high oxidative stability over 5 V vs. Li/Li ⁺)	Expensive for large-scale production, high viscosity, corrosion on Al current collector
Aqueous solvents	Inflammability, low cost, high solubility to salts, high ionic conductivity	Short electrochemical-stable range (0–1.23 V vs. Reversible Hydrogen Electrode (RHE)), low energy/power density

using EIS) and more stage 1 GICs were observed (in Raman and XRD spectra) as the mole fraction of EMC was increased relative to PC. This effect was also observed when EMC was added into 1 M LiPF₆ sulfolane (SL) electrolyte, improving the performance to a stable capacity of $\sim 100 \text{ mA h} \cdot \text{g}^{-1}$ (stage 1 GIC) at 5.4 V (vs. Li/Li⁺) [135,278]. Likewise when 3.5 M LiPF₆ was dissolved into MP, the cell displayed a high capacity of $110 \text{ mA h} \cdot \text{g}^{-1}$ with working potential at 3.0-5.2 V and capacity retention of 90% after 300 cycles [279]. The researchers speculate that anion intercalation is easier with the linear structure of additive EMC and MP, which also helps enhance the ionic conductivity. In comparison, additives with cyclic structure like EC, PC and SL hamper the intercalation process, possibly because of the steric hindrance of ions solvated with these molecules [162,279,281]. However, EMC doesn't work well with all the anions. For instance, it has a compatibility issue with BF₄ anions. EMC solvated BF₄ shows more sluggish mobility and high initial intercalation voltage into graphite electrode when compared with PF₆ in EMC solvents. It is assumed blamed for a strong combination between Li⁺ cation and BF₄ anion and special solvation configuration of EMC around BF_4^- anion [280].

Besides, a group of fluorinated carbonates and fluorinated ether such as FEC, methyl 2,2,2-trifluoroethyl carbonate (F-EMC), ethyl propyl ether (EPE) and tris(hexafluoro-iso-propyl)phosphate (HFIP) are considered as suitable solvents or additives in DIBs. Benefited from fluorine substituents, they derive an improved stability towards oxidation and reduction [240,282–287]. By employing 1.7 M LiPF₆/FEC:EMC (4:6 W: W) + 5 mM HFIP as electrolyte, the reported battery presents stable cycling behavior when operated between 4.0-5.2 V (vs. Li/Li⁺), delivering a satisfactory specific capacity of 85 mA h·g $^{-1}$. The cycle life of analogous cells using only EC and acyclic carbonate lasted for only 10 cycles before failing [70]. In addition, fluorinated carbonates have other advantages like low flammability, high volatility and the capability to form effective SEI layer on the negative electrode surface [105,273].

Noteworthily, sulfone-based solvents [205,288–291] and nitriles electrolytes [292,293] are frequently used solvents/additives in high-voltage LIBs as they also possess very high oxidation potential. There are scarce works [135,278] reporting the use of sulfone-based solvents in DIBs and no work so far uses the nitriles electrolytes. The reason for the situation is maybe closely related to their inherent disadvantages. For sulfone-based solvents, they have a short liquid range and high viscosity which vastly limit their application sites. For nitriles electrolytes, the problem firstly lies on its relatively low solubility for lithium salts while DIBs have high demand on the concentration of charge carriers within electrolyte for a higher specific capacity and energy density [273]. Besides, nitriles electrolytes have low reducing stability and are unable to form protective SEI on negative electrode surface [294]. As a result, the Coulombic efficiency and reversibility of paired negative electrode will get negatively influenced.

In addition to adjusting the composition of solvents, highly concentrated electrolyte (i.e. LiPF₆, LiTFSI) is counted as a route for stable cycling in DIBs [295–298]. They not just improve the anodic and cathodic stability of electrolytes but also help form more uniform and compatible CEI/SEI layers on both electrode surfaces in comparison to the dilute electrolytes and help suppress the corrosion of Al current collector, notwithstanding the loss of ionic conductivity and increased costs [299-303]. For instance, when using high concentration 2 M LiPF₆/EMC:SL (1:4, V:V) as electrolytes and graphite as both electrodes, over 94% of initial capacity is retained after 1000 cycles at a high rate of 5C and superior rate performance is exhibited, with 91 mA $h \cdot g^{-1}$ delivered at a high rate of 20C [301]. Furthermore, higher oxidization stability by using highly concentrated electrolytes allows higher working potential and higher salt concentration could improve the specific capacity to some extent, both of which contribute to the higher energy density of cells [298,301]. For example, impressively high concentrated electrolyte (5 M KFSI in EC/DMC) is realized owing to KFSI's low lattice energy. As applied in DGBs, a dramatically improved 207 Wh·Kg⁻¹ energy density could be achieved in comparison to regular DGBs (20-80 Wh·Kg⁻¹) [298].

5.1.2. Ionic liquids

Ordinary organic solvents face poor stability at high working potentials, and one solution is to adjust the composition of electrolytes or apply high concentrated electrolytes to reach a more negative HOMO without sacrificing other characteristics [299,300]. Another method relies on ionic liquids (ILs) or named room-temperature-molten salts-based electrolytes because of their wide electrochemical stability range [272]. Advantages of ILs that make them promising electrolyte candidates for high-voltage LIBs and DIBs include i) increased difficulty for solvent co-intercalation as ILs are comprised of ions which are too large to co-intercalate into graphite, ii) high safety due to excellent thermal stability, non-flammability and low volatility, and iii) a broad liquid range and ionic conductivity which are comparable with organic solvents [73, 82,304-309], The study on ILs for DIBs could date back to 1994 when Carlin et al. [93] investigated a series of ILs with combinations of cations 1-ethyl-3-methylimidazolium like (EMI^+) dimethyl-3-propylimidazolium (DMPI⁺), and anions like AlCl₄, BF₄, PF₆ and so forth. They reported the feasibility of the ILs in DIBs but didn't go further on the long term performances.

Despite the improved stability of the ILs over a wider potential range, the compatibility with graphite negative electrodes with some of them (like Pyr₁₄TFSI [96,310]) is relatively poor. This is because the increased anodic stability of IL means a thinner SEI formed on the negative electrode surface in comparison to organic solvent-based electrolytes. For this reason, large organic cations (i.e. Pyr₁₄) from the IL are easier to co-intercalate with cations in salts, leading to further graphite exfoliation/severe loss of cycling Coulombic efficiency [96,304,311-313]. The direct solution enabling the use of ILs with graphite negative electrodes is the addition of electrolyte additives such as vinylene carbonate [314], vinyl ethylene carbonate [315], fluoroethylene carbonate [316], chlorethylene carbonate [317], ethylene sulfite (ES) [304,312,314] which assist the formation of SEI layer on negative electrode surface via electrochemical reduction-polymerization. Among them, only ES is reported to effectively suppress the irreversible intercalation/de-intercalation process [304,312] while other additives like dimethyl carbonate (DMC) decompose at high working potentials and cause further loss of Coulombic efficiency [60]. When adding 2 wt% ES into a Pyr₁₄TFSI--LiTFSI-based electrolyte, the system exhibits stable cycling life, where the capacity retains $74\,\text{mA}\,\text{h}\cdot\text{g}^{-1}$ on the 500th cycle at a current rate of $50 \,\mathrm{mA}\,\mathrm{g}^{-1}$. Meanwhile, the maximum capacity reaches $97 \,\mathrm{mA}\,\mathrm{h\cdot g}^{-1}$ nearly doubled the capacity of the system without the electrolyte additive [304,312]. The specific mechanism of the SEI formation in the presence of ES is still unknown so far. One proposed mechanism involves the reduction of additives like ES to sulfur-containing intermediates like Li₂SO₃ or Li₂SO₄ and then undergo another reaction to form the inorganic part of the SEI layer [318]. Several other molecules are also proposed to be responsible for the formation of an SEI layer including (CH2OSO2Li) 2, CH3CH(OSO2Li)- CH2OCO2Li and ROSO2Li. The small lithium ions can pass through the lithium-rich SEI layer, but while at the same time the SEI is impermeable to bulky cations from the ionic liquid [319]

Even if the system can guarantee stable cycles and considerable capacity, materials like lithium and organic additives bring up issues like costs and sustainability. Employing pure ionic liquid like 1-butyl-1-methylpiperidinium bis(trifluoromethylsulfonyl)imide (PP14TFSI) [60], N-butyl-N-methyl-piperidinium bis(trifluoromethylsulfonyl)imide [71] 1-butyl-1-methylpyrrolidinium (PP₁₄NTF₂) and fluoromethanesulfonyl)imide (Pyr14TFSI) [320] as both electrolyte and charge carrier provides another route for studying IL-DIBs. Due to large size of the cation charge carriers, assembled full batteries with the electrolyte deliver comparatively poorer specific capacity than that of metal-cation-based DIBs (i.e. 78 mA $h \cdot g^{-1}$ for PP₁₄NTF₂ when cycling at a current density of 20 mA g⁻¹) [60,71]. Even though, some excellent properties of PP₁₄TFSI-based DIBs still shed light on its future application. It shows superior stability with no capacity decay after 600 cycles. Besides, the intrinsic appropriate conductivity of PP14TFSI is helpful in

hindering the self-discharging process, in turn, contributing to the satisfying Coulombic efficiency (Fig. 21) [60,320].

5.1.3. Aqueous electrolytes

In contrast to strategies for avoiding electrolytes decomposition, one more straight way is to decrease the working potential of anion hosting materials. For instance, the aforementioned graphite alternative positive electrode materials such as MOF, PAH, p-type organic materials all show lower working potential than graphite. Here we introduce a new group of anion-hosting materials (i.e. BiF₃ [108], Fe(C₂H₅)₂ [113], Mn₃O₄ [114], poly(2,2,6,6-tetramethylpiperidinyloxy-4-yl methacrylate) [103] and 1,4 bis(diphenylamino)benzene (BDB) [263]) which possess low enough working potential to allow the safe working of aqueous electrolytes. Although it sacrifices the high working voltage and potential for high energy density, yet the idea is still attractive considering the advantages of aqueous electrolytes such as low cost, environment benignity, high conductivity and safety [109-112]. For instance, manganese (II, III) oxide (Mn₃O₄) (see Fig. 22a) allows the reversible insertion/de-insertion of NO₃ anions from 1 M NH₄NO₃ aqueous electrolytes. It should be noted that cations (i.e. K⁺, Na⁺) insert into Mn₃O₄ instead of anions when their size is small enough to insert into Mn₃O₄ structure. When cycled between 0-1 V vs. Ag/AgCl at the rate of 1 Ag^{-1} , the cells could deliver a discharge capacity up to 150 mA $h \cdot g^{-1}$. Although capacity decays rapidly afterwards, it stabilizes around 50 mA $h \cdot g^{-1}$ with Coulombic efficiency of 99% which indicates a highly reversible reaction (Fig. 22b) [114]. Another material, ferrocene (Fe(C₂H₅)₂) with Fe^{II} ion sandwiched by two cyclopentadienyl rings to form the monoclinic structure (presented in Fig. 22c), is also reported an electrode for reversible insertion/de-insertion of anions at low voltage [321,322]. To inhibit its dissolution within the aqueous electrolyte, ferrocene is penetrated into nanoporous activated carbon via the melt diffusion method with final active mass ratio of 50%. And ferrocene-based half cells based on Equation (12) display a reversible capacity of 106 mA h·g⁻¹ and 80% capacity retention at 1C rate for 100 cycles within optimized electrolyte containing 30 m ZnCl₂ when cycled between 0.4 V and 1.2 V vs. Ag/AgCl (1 m stands for 1 mol solutes in one kg solvent) as displayed in Fig. 22d

Furthermore, when they are paired with some cation-hosting materials which work at higher voltage, full cells are formed but the transfer direction of ions during charging/discharging process gets reversed in

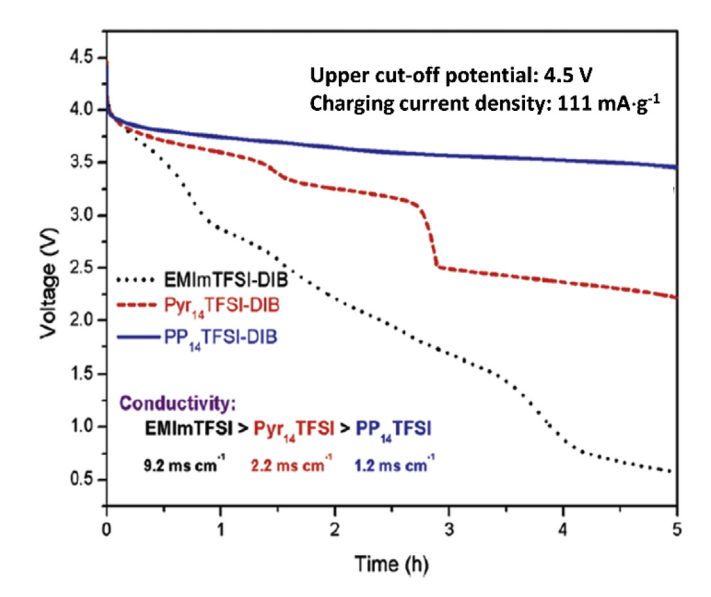


Fig. 21. Self-discharging curves of the DIBs with three different ionic liquids after charging to $4.5\,\mathrm{V}$ at the current density of $111\,\mathrm{mA\,g^{-1}}$ in which the PP₁₄TFSI-based DIBs deliver the best self-discharging-retarding capability and this is ascribed to its appropriate conductivity [60].

Energy Storage Materials 25 (2020) 1-32

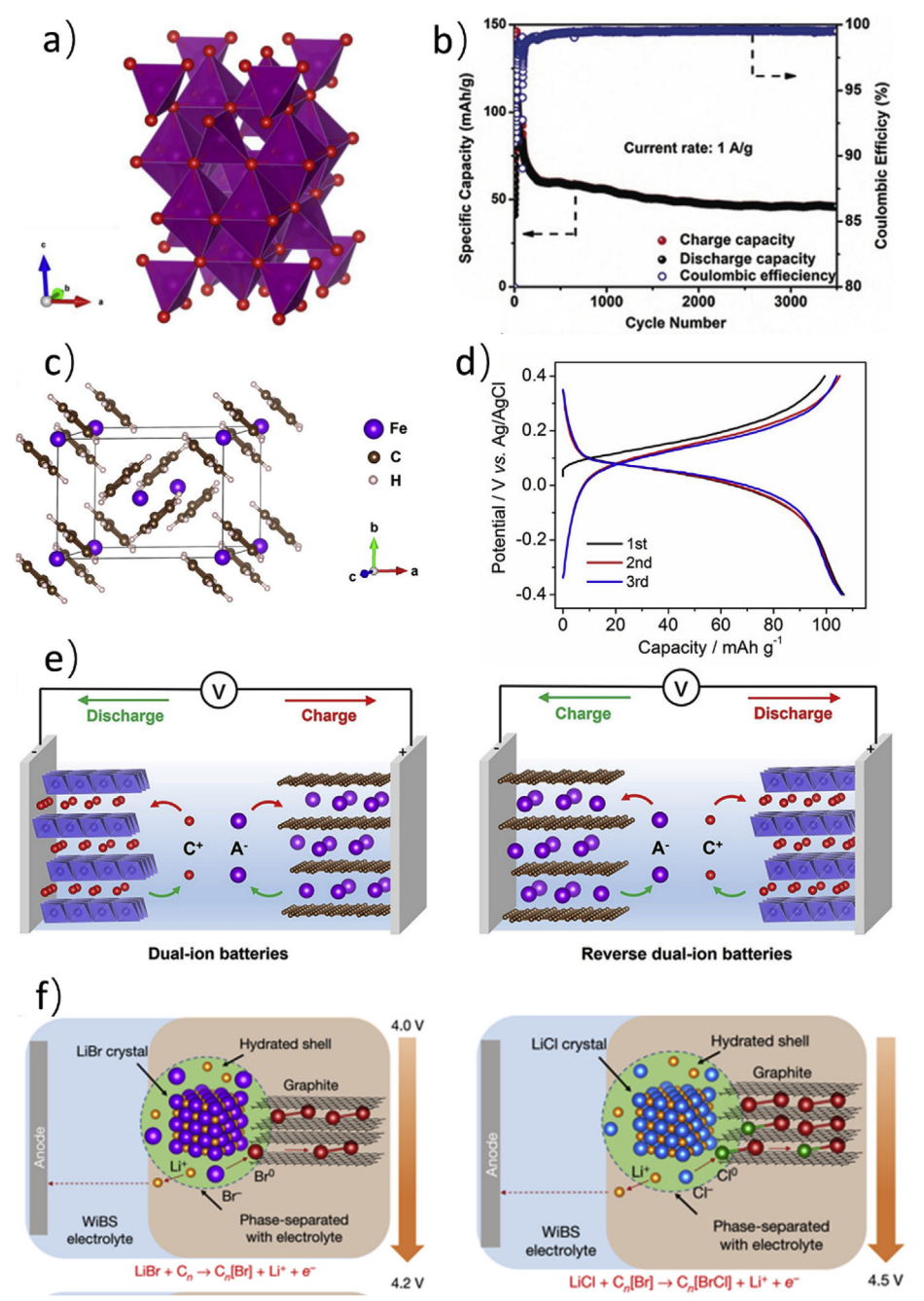


Fig. 22. a) Structure of $\rm Mn_3O_4$ and b) its galvano-static charge/discharge test at a rate of 1 A g⁻¹ [114]. c) Schematic diagram of monoclinic structure of ferrocene (Fe(C₂H₅)₂) and d) its galvanostatic cycling curves of first cycles at 1C within electrolytes containing 30 m ZnCl₂ aqueous solutions [113]. e) Schematic diagram of conventional DIBs (left) and reverse DIBs (right) with ions transfer towards reversed direction during the charging/discharging process [113]. f) Schematic illustration of hydrated layer on surface and two-step reaction of Cl⁻ and Br⁻ intercalation into graphite interlayers in sequence [324].

comparison to conventional DIBs (as shown in Fig. 22e) [113]. The new configuration is also called "Reverse DIBs" [113]. For instance, BiF $_3$ could reversibly adsorb and release F^- anions according to Equation (13) with the configuration of BiF $_3$ as negative electrode, Na $_{0.44}$ MnO $_2$ as positive electrode and NaF aqueous solution as electrolyte, the full cells deliver the initial discharge capacity of 123.34 mA h·g $^{-1}$ at 100 mA g $^{-1}$ and the outstanding rate performance with almost 82.8% capacity retention when running at 3200 mA g $^{-1}$ and cycled between 0 V and 1.5 V. One fatal shortcoming is that the capacity decays quickly even at 100 mA g $^{-1}$ with only 47.28 mA h·g $^{-1}$ discharge capacity left after 40 cycles [108].

$$2Fe(C_5H_5)_2 + [ZnCl_4]^{2-} - 2e^- \Leftrightarrow 2[Fe(C_5H_5)_2]^+ [ZnCl_4]^{2-}$$
 (12)

$$BiF_3 \Leftrightarrow Bi + 3F^-$$
 (13)

Nevertheless, low working potential followed by the limited energy density becomes the greatest block on aqueous electrolyte way for further development and broad application [273]. Under the circumstances, Xu et al. developed several highly concentrated aqueous electrolytes or called "water-in-bisalt" electrolytes (WiBS) which broadened the stable working range to over 4V [323,324]. The positive electrode material used in their work is the composite of lithium halide salts (LiBr and LiCl) and graphite with the mass ratio of 2:1:2. When immersed in highly concentrated aqueous electrolyte (21 mol kg⁻¹ LiTFSI + 7 mol kg⁻¹ lithium trifluoromethanesulfonate (LiOTf) dissolved in water), both lithium halide salts in electrode will absorb a certain amount of water from electrolytes and form a hydrated layer on electrode surface, which supports the fast diffusion of Li⁺ and helps reserve anions within electrodes (see Fig. 22f) [324]. Then Br and Cl will intercalate into graphite interlayers in sequence during the charging process and de-intercalate in reverse sequence during the discharging process with an

average potential of 4.2 V (see Fig. 22f). Remarkably, the composite positive electrode together with the WiBS-contained gel electrolytes delivers a high initial capacity of $243 \, \text{mA h} \cdot \text{g}^{-1}$ and remains 82% after 230 cycles at the rate of 0.2C in a three-electrode cell. The full cell with graphite as negative electrode also exhibits a high capacity of $127 \, \text{mA h} \cdot \text{g}^{-1}$, high energy density of $460 \, \text{Wh} \cdot \text{kg}^{-1}$ (calculated based on overall mass of both electrodes) and good cyclic stability with 74% capacity remained at the rate of 0.2C after $150 \, \text{cycles}$ [324].

Overall, finding electrolytes which could bear high working potential of graphite-positive electrode-based DIBs is one determining factor to achieve stable and reversible cycling. For conventional dilute organic electrolytes, they could be mixed with other solvents or additives that could help form effective solid interface on electrode surface or possess high stability towards oxidization. Among the co-solvents or additives, the fluorinated solvents like FEC are considered as the most appropriate options for DIBs while other types of solvents like nitriles or sulfone solvents are received much less attention partially due to their intrinsic shortcomings like high melting point or limited solubility for salts. Some other strategies including highly concentrated electrolytes and ionic liquids also possess high oxidative stability. However, they are hindered by the high cost. Furthermore, by using ILs as electrolytes, graphite negative electrode usually suffers from low stability or low specific capacity due to the difficult intercalation of large organic cations from ILs. In comparison, the highly concentrated electrolytes exhibit far more advantages than ILs including the chemical compatibility with current collector and improvement over cells' specific capacity and energy density. The aqueous solvents are also feasible in the system of DIBs because they allow for anions intercalation at relatively low voltage and their advantages like high conductivity, sustainability and low price help them attract more attention. Nevertheless, one fatal disadvantage of the aqueous electrolytes is their narrow electrochemical-stable window followed by limited energy/power.

5.2. Salts and ions

Between the tight supply of lithium resources and the projected demand for electric vehicle/utility-scale energy storage systems, lithium shortage may become more serious in the next years [325,326]. This uncertain situation forces researchers to seek suitable alternatives for lithium. In this case, monovalent $(K^+, Na^+ \text{ and } NH_4^+)$, divalent $(Mg^{2+}, Ca^{2+} \text{ and } Zn^{2+})$ as well as trivalent (Al^{3+}) cations come into view in the past decades majorly due to their abundance in nature [77]. As summarized in Fig. 23, element Al. Ca. Na. K. Mg separately ranked 3rd, 5th.

6th, 7th, 8th of abundance in the crust earth while Li ranked at 33rd [46]. And natural resources like air and sea have considerable reserves for element C, N, H, O which are resources to synthesize NH⁺₄ cations. Besides, potentially higher volumetric energy density of multivalent alkali metal ions shed lights on their future development. However, the high redox potential of alternative cations has a negative influence on performances. Besides, negative electrode material is the host for cation charge carriers in DIBs system. The enlarged size of these alternative cations also imposes some compatibility issue with negative electrode materials. In this part, we aim at introducing the intrinsic properties of these alternative cations with sub-categories of monovalent alkali metal cations, multivalent alkali metal cations and others which includes individual examples of free-metal cations and highlighting the progress made in the recent years.

5.2.1. Monovalent alkali metal cations

As Na and K lie in the same group and right below Li in the periodic table, they share many similar physical and chemical properties [52,59, 62,327,328]. Theoretically, these advantages help reduce the difficulty on research as the mature knowledge from LIBs could be directly transplanted to study Na- and K-DIBs. And considering their rich reserve in crust of the earth, Na- and K-DIBs are promising candidates as new energy storage devices. Nevertheless, both K and Na possess higher redox potential (-2.93 V for K/K⁺ and -2.71 V for Na/Na⁺) than Li (-3.04 Vfor Li/Li⁺) referenced to the potential of the standard hydrogen electrode (SHE) [23,329-333]. The insertion potential of Na⁺ on negative electrode side is improved accordingly, which decreases the working potential of the full cells and damages the delivered energy density. Besides, K and Na possess large ionic radius than Li (1.02 Å for Na⁺, 1.38 Å for K⁺ vs. 0.76 Å for Li⁺) which imposes higher demand on the host materials, especially the intercalation-type materials [37,81,146,164]. In the history of DIBs, there are several negative electrodes that support the reversible/stable insertion/de-insertion of Na⁺/K⁺.

The first work on sodium-ion-based DIBs (Na-DIBs) applied the hard carbon as negative electrode material, which could deliver $\sim\!300\,\text{mA}\,\text{h}\cdot\text{g}^{-1}$ capacity with an average redox potential of $0.3\,\text{V}$ vs. Na/Na^+ [37,99]. The optimizing cells with an electrolyte containing 0.5 M NaPF₆/EC:DEC (1:1, W:W) and graphite as positive electrode show relatively stable cycling for 100 cycles under the current of 100 μA , yet they only deliver a discharge capacity of 55–60 mA h·g $^{-1}$. Thereafter, intercalation-type Na₂Ti₃O₇ (NTO) featuring a sodium-insertion potential around 0.3 V vs. Na/Na $^+$ is also applied as negative electrode in Na-DIBs. NTO possesses a unique zigzag-like layered structure (see

Availability

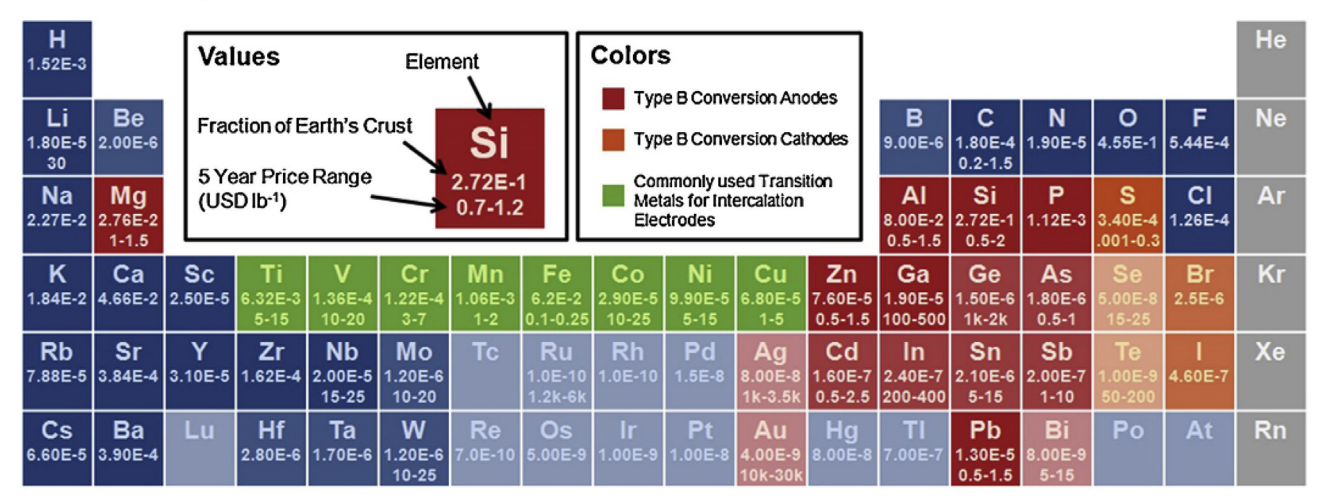


Fig. 23. Periodic table with element abundance in the crust and their price range [46].

Fig. 24a) which is composed of edge-connected TiO₆ octahedra and large bandgap (~3.7 eV) and result in the increased resistance of ions and electrons transfer [334-336]. Meanwhile, large volume change during intercalation/de-intercalation of large Na⁺ leads to an inferior cyclic stability. Hence, the conductive reduced graphene oxide (rGO) coating on the surface is adopted to improve the performance. Assembling it into full cells with coronene as positive electrode yielded a high voltage of 3.2 V and ~75% capacity retention after 5000 cycles. It is interesting that this type of DIBs operated at -20 °C still showed 100% Coulombic efficiency and 20% capacity retention compared to data collected at room temperature [59]. Besides, as mentioned above, a composite negative electrode named (MoS₂/carbon fiber)@MoS₂@C delivers rather stable discharge capacity thanks to the protection from the outer carbon shell and good rate capability owing to the 3D interconnected structure and good conductivity of the carbon fiber substrate (Fig. 18b-d) [240]. In another work, a soft carbon negative electrode is doped with phosphorus and used as negative electrode in Na-DIBs (Fig. 24b). By this method, the incorporated phosphorus is supposed to donate electron density to the conduction band of the soft carbon, which is supported by emerging peaks near the Fermi energy level (see Fig. 24c) and dramatically improved conductivity (from 7.46×10^{-4} S/cm to 9.79×10^{-3} S/cm). In turn the full cells display excellent performance with 81 mA h·g⁻¹ capacity retention under 1A g⁻¹ after 900 cycles. Furthermore, to compensate for the initial sodium lost in forming the SEI layer on negative electrode surface, regular pre-sodiation is executed which efficiently improved the initial Coulombic efficiency to 90% [337].

For potassium-based DIBs (K-DIBs), graphite is the most frequently used negative electrode [216,332,338]. In half cell configuration by using K metal as counter electrode and electrolyte of $0.8\,\mathrm{M}$ KPF₆/EC:DEC (1:1, V:V), graphite exhibits a rather stable profile and a considerable

discharge capacity of 210 mA h·g⁻¹ at the current density of 100 mA g⁻¹ and cycled in range of 0.01-3 V. Besides, it shows good rate capability, with $110 \, \text{mA} \, \text{h} \cdot \text{g}^{-1}$ remaining at $500 \, \text{mA} \, \text{g}^{-1}$ and $250 \, \text{mA} \, \text{h} \cdot \text{g}^{-1}$ when cycling rate returns to $50 \, \text{mA} \, \text{g}^{-1}$. In the full cell test, graphite negative electrode is assembled with PTPAn positive electrode and tested in the same electrolyte. The cells present an average discharge voltage of merely 3.23 V which is far lower than conventional DIBs and display a small discharge capacity of 60 mA h·g⁻¹ despite the superior rate performance and fascinating cycling stability with a capacity retention of 75.5% over 500 cycles [216]. In contrast, replacing the organic positive electrode (PTPAn) with graphite positive electrode is effective to improve the average discharging potential. Ji et al. [332] and Fan et al. [338] separately achieve average discharging potential of 4.5 V and 3.96 V vs. K/K⁺ and both works present similar discharging capacity of \sim 61 mA h·g⁻¹ at 1C in 1 M KPF₆/EC:DMC:EMC (4:3:2, V:V:V) and 0.8 M KPF₆/EC:DMC (1:1, V:V) respectively. In ionic liquid-based electrolytes of 0.3 M KTFSI/Pyr₁₄TFSI +2 wt% ES, full cells with graphite as both electrodes is able to operate at 4.5 V vs. K/K⁺ and deliver a stable capacity (~42 mA h·g⁻¹) for over 1500 cycles with high Coulombic efficiency of 99% at the current density of 250 mA g^{-1} [339].

The above materials show some good capabilities for hosting large Na^+ and K^+ but still suffer from limited capacity. In recent years, metal negative electrodes that work with alloying mechanism receive a lot of attention due to their high theoretical capacity as mentioned above. For instance, tin (Sn) could alloy with both Na and K to form $Na_{15}Sn_4$ (846 mA $h\cdot g^{-1}$) and KSn (226 mA $h\cdot g^{-1}$) separately [243,340]. In addition, an improvement over mass ratio of active material is realized by entitling metal negative electrode the function of current collector simultaneously, in turn, the energy density get increased. By using Sn metal as multi-function negative electrode, Na-DIBs and K-DIBs

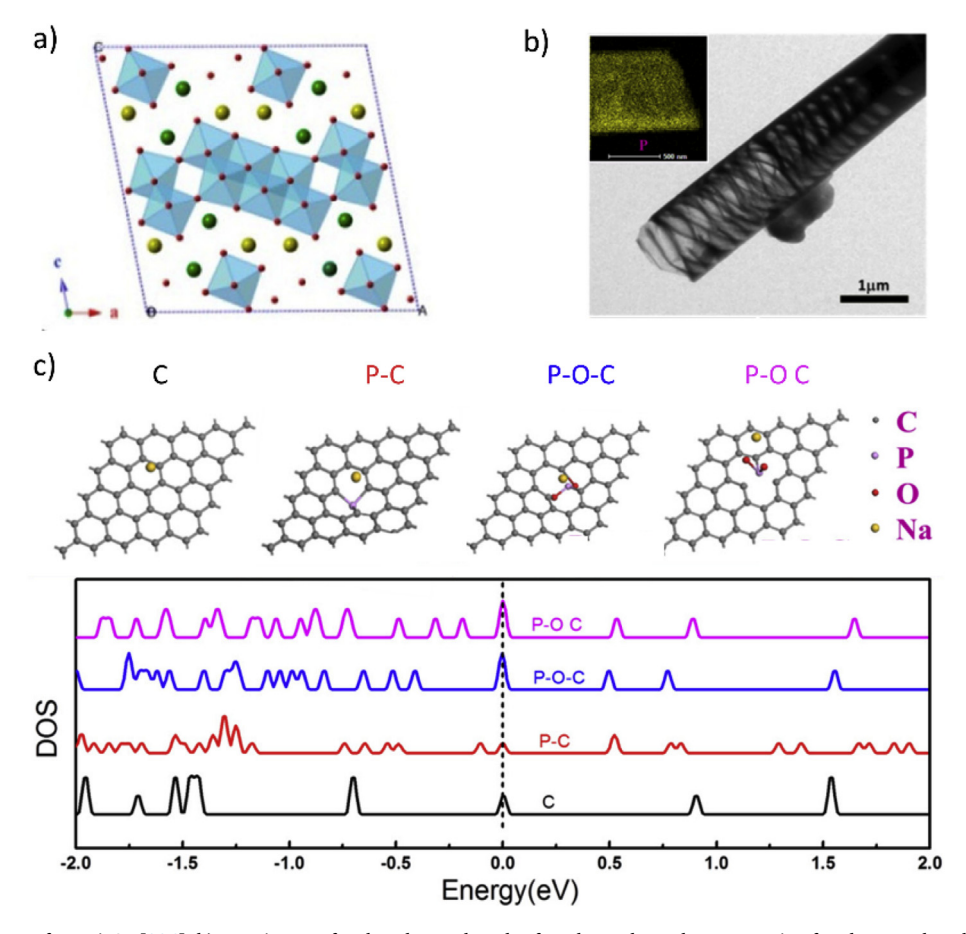


Fig. 24. a) Crystal structure of Na₂Ti₃O₇ [336]. b) TEM image of a phosphorus-doped soft carbon tube and EDX mapping for element phosphorus, scale bar: 1 µm and c) monolayer configuration of sodium adsorption on pristine graphite, P-doped graphite including P-O-C, P-O C, P-C and corresponding density of states (DOS) [337].

separately achieve high energy density of $144 \, \text{Wh} \cdot \text{kg}^{-1}$ at a power density of $150 \, \text{W kg}^{-1}$ and $155 \, \text{Wh} \cdot \text{kg}^{-1}$ at a power density of $116 \, \text{W kg}^{-1}$ [102,195].

Another challenge associated with the Na-DIBs and K-DIBs is the sluggish solid-diffusion capability of Na⁺ and K⁺ in intercalation-type host materials and poor cyclic performance due to their relatively large ionic radius. To deal with the challenges, some materials which are widely applied in supercapacitors and store electric power through capacitive behaviors (e.g. hierarchical porous amorphous carbon [259], activated carbon [260], carbon foam [218]) are incorporated into the DIBs to replace the originally diffusion-controlled insertion-type negative electrodes. When the positive and negative electrodes in full cells are the combination of capacitive-behavior and intercalation-behavior, the new type of cells is termed as hybrid DIBs or dual-ion capacitors (DICs) [211, 259,260]. For instance, Lu et al. reported one DICs with capacitive-type microporous carbon foam as both electrodes and 0.8 M KPF₆/EC: DEC (1:1, V:V). Benefited from the capacitive mechanism, the cells deliver superior rate capability and long-term cyclic stability, with over $51\,\text{mA}\,\text{h}\cdot\text{g}^{-1}$ capacity delivered at a high rate of 10 A g $^{-1}$ and 97.7% capacity remaining after 10000 cycles at 2 $\mathrm{A}\,\mathrm{g}^{-1}$. In addition, the cells also deliver good energy density of 39 Wh kg⁻¹ at a power density of $7800 \,\mathrm{W \, kg^{-1}}$ [218].

5.2.2. Multivalent alkali metal cations

Multiple alkali metal cations (*i.e.* Al³⁺, Zn²⁺, Ca²⁺) are able to store multiple electrons when they insert into the host materials (negative electrode in DIBs). This feature bestows them a potential for higher volumetric energy density. As property differs between Ca and Al& Zn, they are introduced separately in the following part.

5.2.2.1. Calcium-based DIBs. Calcium-based-DIBs (denoted as Ca-DIBs) are attractive because Ca possess a plating potential of -2.87 V vs. SHE which is closer to the plating potential for lithium than sodium and gives it the potential for a wider operating voltage window [341–343]. But the study on it is still at the very beginning stage and only two papers report the relevant content. The first work uses alloying type-metal Sn as negative electrode and graphite as positive electrode. For the electrolyte, it is composed of four solvents (EC, PC, DMC and EMC) (2:2:3:3, V:V:V:V) and 0.8 M Ca(PF₆)₂ salt. Each solvent plays a specific role contributing to the electrochemical performance. Specifically, EC can be reduced to form a passivation film on negative electrode materials (SEI) in initial cycles and guarantees good reversibility/stability in the following cycles. Simultaneously, EC and PC possessing high dielectric constant are used to dissolve the salts. The addition of linear dimethyl carbonate (DMC) and ethyl methyl carbonate (EMC) help improve the ionic conductivity and decrease viscosity. The cells exhibit utmost merely 85 mA h·g $^{-1}$ capacity at the current density of 100 mA g $^{-1}$ with unstable Coulombic efficiency, ranging from 80 to 95%, but excitingly it shows relatively stable performance and good capacity retention. Even cycling at current rate of 100 mA g⁻¹ for 350 cycles, 95% of the highest capacity can be retained [101]. When using mesocarbon microbeads (MCMB) as negative electrode instead of Sn in cooperation with an expanded graphite (EG) positive electrode and electrolyte of 0.7 M CaPF₆ in EC/DMC/EMC (4:3:2, V:V:V), the Ca-DIBs shows a decreased performance of $66\,\mathrm{mA\,h\cdot g}^{-1}$ discharging capacity at 1C and 94% capacity retention after 300 cycles with voltage window of 3-5 V [341].

5.2.2.2. Aluminum and Zinc-based DIBs. Unlike Ca, Al and Zn have low reactivity and high stability which allow the use of Al and Zn metal as negative electrode in full cells. This is fascinating as both of them combine the advantages of great abundance in nature, low cost, high volumetric and gravimetric capacity (2981 mA $h \cdot g^{-1}$ and 8056 mA $h \cdot cm^{-3}$ for Al, 820 mA $h \cdot g^{-1}$ and 5857 mA $h \cdot cm^{-3}$), high safety and so forth [344].

Besides, the potential of Zn (-0.76 V vs. SHE) is much less negative

than that of Li⁺, Na⁺, Al³⁺ and it has large overpotential for H₂ evolution. Hence, Zn metal has the capability to be used as negative electrode in aqueous electrolyte [345,346]. To count, there are also only two works on aqueous zinc-ion-based DIBs (abbreviated as Zn-DIBs). In one work, an organic positive electrode (1,4 bis(diphenylamino)benzene (BDB)) which works through two-electron redox reaction on nitrogen atom and BDB is coated with cellulose membrane in order to prevent its dissolution during cycling. And the aqueous electrolytes dissolve high concentrated salts (1 m zinc triflate (Zn(OTf)2 and 19 m LiTFSI) to improve the reduction and oxidation resistance [215]. During cycling process, plating/de-plating of Zn²⁺ occurs on Zn negative electrode while anions including TFSI⁻ and OTF⁻ adsorb/release from BDB positive electrode. The cells deliver a discharge capacity of $120-125 \text{ mA h} \cdot \text{g}^{-1}$ at the rate of 26 mA g⁻¹ and a satisfying cyclic stability with over 82% capacity retention after 500 cycles at the rate of 3C with almost 100% Coulombic efficiency. However, the low working potential (1.25 V vs. Zn/Zn²⁺) damages the energy density. Calculating based on the mass of both electrodes and intercalated anions, the cells only contribute energy density of 60-80 Wh·Kg⁻¹. In another work, the cell is designed with Reverse DIBs configuration (Fig. 25a) as mentioned above. Zn²⁺ hosting material prussian blue Zn₃[Fe(CN)₆]₂ is used as positive electrode and $(ZnCl_4)^{2-}$ hosting material $Fe(C_2H_5)_2$ is applied as negative electrode. According to the authors, increasing salt concentration in water in salt electrolyte promotes negative shift intercalation/de-intercalation in positive electrode and positive shift of cations intercalation/de-intercalation in negative electrode, though the exact explanation is still unclear (Fig. 25b). Thereafter, an optimizing electrolyte (30 m ZnCl₂ in water) is chosen and the assembled full cells exhibit an average potential of 0.9 V. Even though the cells only deliver a capacity of 40 mA h·g⁻¹ and 58% capacity retention after 1000 cycles, it still paves some new ways on studying Zn-DIBs [113].

For aluminum-ion-based DIBs (Al-DIBs), all the works apply the Al metal as negative electrode due to its advantages mentioned above. Majorly two reaction mechanisms contribute the Al to the negative electrode depending on the electrolytes. In the molten salt mixture of MCl/AlCl₃, Al has different clusters present in an acidic melt including AlCl₄ and Al₂Cl₇ and an equilibrium equation exists for these substances (Fig. 25c) [347]. With more AlCl₃ in the mixture, Al₂Cl₇ will be the major substance. Conversely, less AlCl₃ will make AlCl₄ the dominant substance [348,349]. In DIBs system, a combination of AlCl₃/1-ethyl-3-methylimidazolium chloride ([EMIm]Cl) ionic liquid is broadly applied as electrolyte and graphite/Al as positive/negative electrodes separately. Upon charging, the Al₂Cl₇ anion can be reduced on the negative electrode side to deposit Al while AlCl₄ intercalates into graphite positive electrode (see Fig. 25d). Therefore, the ratio of AlCl₃/[EMIm]Cl in the mixture has direct connection with overall performances of the Al-DIBs, as proved by several works [100,350]. To be specific, increasing amount of AlCl₃ to [EMIm]Cl ratio in the electrolyte firstly leads to the improvements of discharge capacity before 1.3 and then decrement of discharge capacity from 1.3 to 2 (2 is saturated amount of AlCl₃ in the mixture), and increasing ratio constantly promotes the improvement over energy density as seen in Fig. 25e. Utmost 150 mA h·g⁻¹ specific capacity could be achieved with an energy density of only 33 $\mbox{Wh} \cdot \mbox{Kg}^{-1}$ at the ratio of 1.3 while the maximum energy density of 62 Wh·Kg⁻¹ could be obtained by sacrificing a little bit specific capacity (\sim 124 mA h·g⁻¹) at the ratio of 2 [350].

In addition to salt concentration, the positive electrode material is assumed another limiting factor for overall performance [350]. In order to achieve high performance, a series of graphite structures are designed. Here we introduce their morphology and synthesis method and their performance will be summarized in Table 2 for easy comparison. The first work is done by Dai et al., in which the graphitic foam (Fig. 25f) is used as positive electrode material in Al-DIBs. The material is synthesized via few steps, including chemical vapor deposition (CVD) of graphite on nickel foam, surface coating poly(methyl methacrylate) (PMMA), removing nickel foam by acid at 80 °C and removing PMMA by acetone followed by

Energy Storage Materials 25 (2020) 1-32

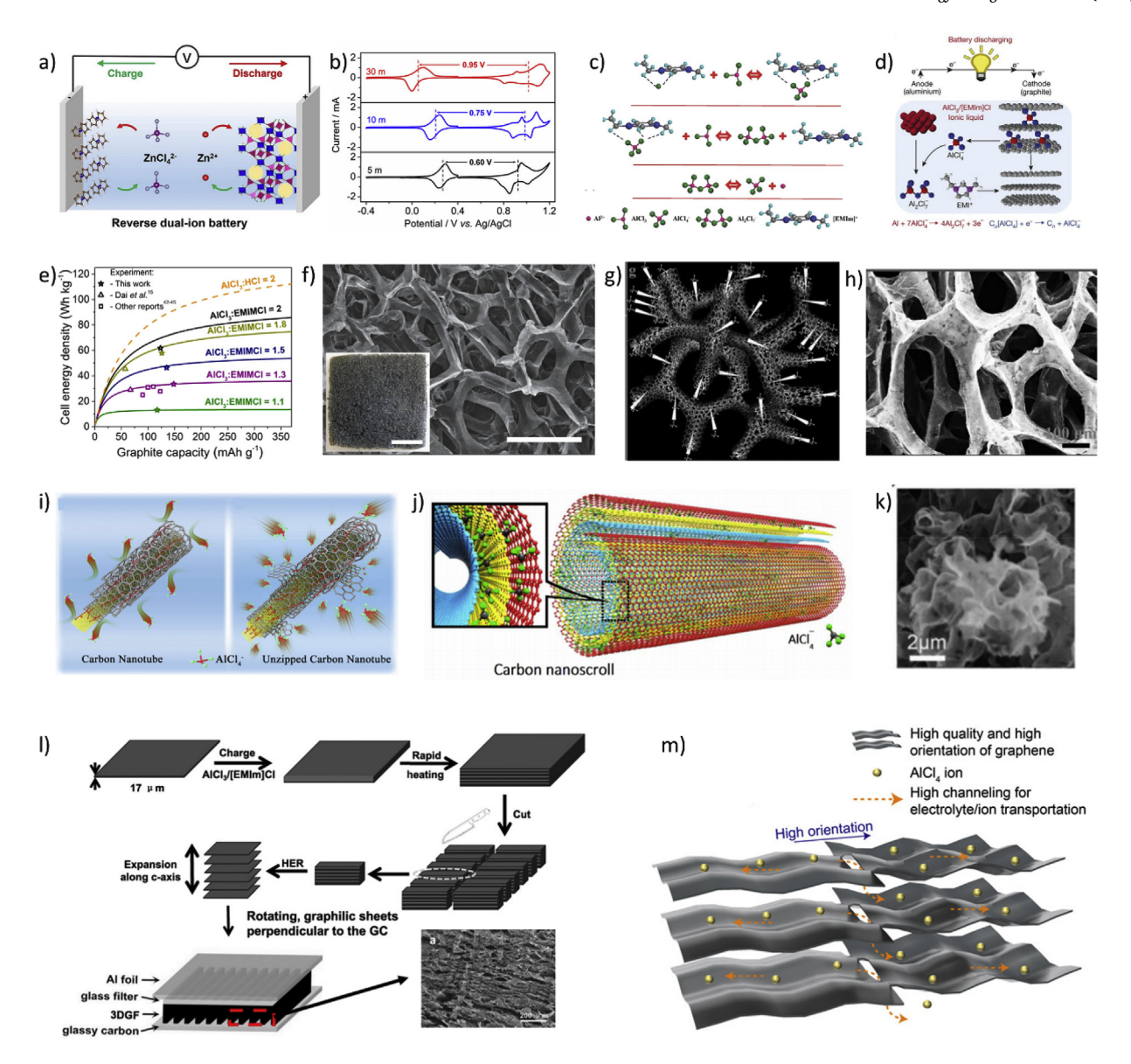


Fig. 25. a) Schematic diagram of $Fe(C_2H_5)_2||30$ m $ZnCl_2$ aqueous solution $||Zn_3[Fe(CN)_6]_2$ cell with reverse DIBs configuration and b) comparison of CV curves of $Fe(C_2H_5)_2$ negative electrode and $Zn_3[Fe(CN)_6]_2$ positive electrode in different concentration of $ZnCl_2$ electrolytes [113]. c) Reactions happen in $AlCl_3/[EMIm]Cl$ ionic liquid [347]. d) Schematic diagram of $Al||AlCl_3/[EMIm]Cl$ ionic liquid [graphite cells during discharging process [100]. e) Calculated (curves) and experimental (data points) cell-level graphite capacity and energy density for hosting $AlCl_4^-$ anions [350]. f) SEM image and light microscopy image of graphite foam with porous structure [100]. g) Schematic diagram of porous graphene foam and h) SEM image of it [351]. i) Schematic illustration of unzipped carbon nanotube (right) which possesses more electrochemical active sites than bare carbon nanotube (left) [354]. j) Schematic illustration of carbon nanoscrolls containing several layers of graphene [355]. k) SEM image of edge-rich graphene paper, scale bar: $2 \mu m$ [356]. l) Schematic diagram of synthesis process of a monolithic graphite foam with its SEM image, scale bar: $200 \mu m$ [357]. m) Schematic diagram of highly oriented graphene with the smooth route for $AlCl_4^-$ anions transfer [189].

annealing in $\mathrm{NH_3}$ atmosphere [100]. The porous structure allows the rapid diffusion of anions between electrolyte and positive electrode. And it is helpful to bear the volume expansion during anion intercalation. In order to enhance the surface area, the foam structure is also widely adopted in other works. After growing graphene on nickel foam via CVD, the composite is etched by $\mathrm{Ar^+}$ plasma and nickel foam is removed in order to achieve a porous 3D graphene foam (Fig. 25g,h) [351]. To note, the energy of $\mathrm{Ar^+}$ plasma to create pores in graphene isn't enough to bring in vacancies [352,353]. Nevertheless, the aforementioned synthesis methods are fairly complicated and the nickel foam take up large mass and volume in cells which jeopardize the energy density of cells. Hence, high active mass loading and facile synthesized materials are developed to meet the demands on practical use. In one work, the low-cost carbon nanotubes attached by graphene nanoribbons, termed as unzipped carbon nanotubes exhibit far better electrochemical performances than bare

carbon nanotube counterparts and show great potential as positive materials in Al-DIBs (Fig. 25i). The kinetics is dramatically improved by applying the materials since it offers facile transfer of both anions and electrons [354]. In another work, the curly carbon nanoscrolls containing several layers of graphene are also synthesized through a facile multi-step sintering process in which the Fe³⁺ acts as the catalyst for the synthesis reactions (Fig. 25j). In addition to simplified synthesis process, the method also exhibits other advantages like low cost and superior electrochemical performances of the obtained carbon nanoscrolls [355]. Besides, the high surface-area edge-rich graphene is synthesized by firstly growing over nickel particles through calcination in CH₄ atmosphere and later washed with HCl solution to remove the nickel substrate (Fig. 25k). Notably, the material delivers superior electrochemical performance at various working temperature and outstanding flexibility [356]. Meanwhile, tuning the orientation of graphene sheets in graphite is also a

Table 2Structure of the graphite positive electrodes in different work and comparison of their performances in full cells.

Positive Electrodes	Electrolyte	Capacity	Cyclic Stability	Rate Capability	Reference
Graphite foam	AlCl ₃ /[EMIm]Cl ionic liquid (1.3:1, molar ratio)	60 mA h· g^{-1} at 4 A g^{-1}	\sim 100% capacity retention after 7500 cycles at rate of 4 A g $^{-1}$	no obvious decay (60 mA h· g $^{-1}$) with discharging/ charging rate at 1–6 A g $^{-1}$	[100]
Porous graphene foam	AlCl ₃ /[EMIm]Cl ionic liquid (1.3:1, molar ratio)	$150 \text{ mA h} \cdot \text{g}^{-1} \text{at}$ 2 A g^{-1}	\sim 100% capacity retention (123 mA h·g $^{-1}$) after 10000 cycles at rate of 5 A g $^{-1}$	$111\text{mA}\text{h}\cdot\text{g}^{-1}$ with discharging/charging rate of $8A\cdot\text{g}^{-1}$, no capacity decay (125 mA h·g $^{-1}$) with discharging capacity from $0.5-5\text{A}\text{g}^{-1}$ and charging rate of $5\text{A}\text{g}^{-1}$	[351]
Unzipped carbon nanotubes	AlCl ₃ /[EMIm]Cl ionic liquid (1.3:1, molar ratio)	$100 \text{ mA h} \cdot \text{g}^{-1} \text{ at}$ 2 A g^{-1}	\sim 100% capacity retention after 5000 cycles at rate of 5 A g ⁻¹	$\sim\!100\text{mA}h\text{-g}^{-1}$ with discharging/charging rate of $2A\text{-g}^{-1},\sim\!75\text{mA}h\text{-g}^{-1}$ with discharging/charging rate of 5 A g $^{-1}$	[354]
Carbon nanoscrolls	AlCl ₃ /[EMIm]Cl ionic liquid (1.3:1, molar ratio)	\sim 104 mA h· g $^{-1}$ at 1 A g $^{-1}$	\sim 100% capacity retention after 55000 cycles at rate of 50 A g $^{-1}$	no obvious decay ($\sim\!100$ mA h \cdot g $^{-1}$) with discharging/charging rate at 5–100 A g $^{-1}$	[355]
Edge-rich graphene paper	AlCl ₃ /[EMIm]Cl ionic liquid (1.3:1, molar ratio)	\sim 128 mA h· g ⁻¹ at 2 A g ⁻¹	\sim 100% capacity retention after 20000 cycles at rate of 8 A g $^{-1}$	\sim 128 mA h·g ⁻¹ with discharging/charging rate of $2A \cdot g^{-1}$, \sim 84 mA h·g ⁻¹ with discharging/charging rate of 10 A g ⁻¹	[356]
Expanded graphite foam and aligned perpendicular to current collector	AlCl ₃ /[EMIm]Cl ionic liquid (1.3:1, molar ratio)	$60 \text{mA h} \cdot \text{g}^{-1} \text{at}$ 12A g^{-1}	\sim 100% capacity retention (60 mA $h \cdot g^{-1}$) after 4000 cycles at rate of 12 A g^{-1}	no capacity decay (60 mA $h \cdot g^{-1}$) with discharging capacity from 0.5 – 5 A g^{-1} and charging rate of 5 A g^{-1}	[357]
Highly ordered graphene film	AlCl ₃ /[EMIm]Cl ionic liquid (1.3:1, molar ratio)	$120 \text{ mA h} \cdot \text{g}^{-1}$ at 6 A g^{-1}	\sim 100% capacity retention (120 mA h g ⁻¹) after 25000 cycles at rate of 12 A g ⁻¹	no obvious decay (with discharging/charging rate at 10–200 ${\rm Ag}^{-1}$	[358]

feasible way to enhance performances. For instance, a monolithic graphite foam (Fig. 251) is synthesized with some graphene sheets and short of defects/impurities on surface. The schematic diagram of the synthesis process is shown in Fig. 25l. With pyrolytic graphite (PG) foil as sources, it is first intercalated with AlCl₄ anions, followed by heating and inducing hydrogen evolution with electro-catalyst method in order to expand the compact graphite structure. Thereafter, the electrode is made with graphene sheets aligned perpendicular to current collector in order to create the smooth route for anions to diffuse [357]. In another work, orientated graphene sheets (Fig. 25m) are realized by cast coating/wet spinning GO crystal liquid over substrate to form a thin film. Then it undergoes reduction and annealing at 2850 °C to form perfect oriented graphene sheets with low density of defects and groups. Materials made in this way also possess smooth route for anions transfer and has better electric conductivity/mechanical properties than nickel foam counterparts [358].

As an alternative, Al-DIBs could also work in organic liquid electrolytes but with a different mechanism. By employing 1 M Al(ClO₄)₃ in PC + 5.5 wt% FEC as electrolyte, Al nanowires grown over Al foil as negative electrode and 3D-graphite foam as positive electrode, Al $^{3+}$ plates/strips on/from Al metal negative electrode and ClO $_{4-}^{4}$ anions reversibly intercalate/de-intercalate in/from graphite positive electrode. With the configuration, the batteries display brilliant long cycling life, presenting nearly 100 mA h·g $^{-1}$ discharge capacity after 400 cycles at a high current density of 2000 mA g $^{-1}$. However, the battery still has enormous space to improve as the average Coulombic efficiency is merely 75% [189].

5.2.3. Others

The Li⁺ alternatives discussed above are all metal ions (*i.e.* Na⁺, K⁺, Ca²⁺, Al³⁺, Zn²⁺). In contrast, non-metal cations receive much less attention. It should be noted that these cations have some attractive features and could deliver comparable performance to metal-ion-based batteries [60,71,263]. For instance, metal-free hosting materials and charge carriers usually compose of abundant elements in the earth like C, N, O, S. The assembled metal-free full cell is expected to have low cost [60,71,263]. The first example is the aqueous ammonium DIBs (NH₄⁺-DIBs) with n-type material 1,4,5,8-naphthalenetetracarboxylic dianhydride-derived polyimide (PI) as negative electrode, p-type material poly(2,2,6,6-tetramethylpiperidinyloxy-4-yl methacrylate) (PTMA) as positive electrode and 1 M (NH₄)₂SO₄ aqueous solution as electrolyte [263]. All the components in the system are composed of cheap and abundant resources in nature. Besides, NH₄⁺ cation in aqueous solution is

prominent over alkali metal ion counterparts (i.e. Na⁺, K⁺, Ca²⁺, Al³⁺, Zn^{2+}) not only because of its low molar mass (18 g mol⁻¹) but also due to its low hydrated ionic size of 3.31 Å. A smaller size is helpful to improve its transfer rate in electrolytes. Above all, the cells cycled between 0 V and $1.9\,\mathrm{V}$ deliver a high discharge capacity of $136.5\,\mathrm{mA}\,\mathrm{h\cdot g}^{-1}$ at the current density of 0.5 A g-1 and have 86.4% capacity retention after 10000 cycles at the current density of 5 A $\rm g^{-1}$. The cells exhibit good rate capability as well, with $\sim 100 \text{ mA h} \cdot \text{g}^{-1}$ capacity remaining at the rate of 5 A g⁻¹ and \sim 80 mA h·g⁻¹ capacity remaining at the rate of 10 A g⁻¹. Limited by its low working potential, it could present a maximum energy density of 51.3 Wh·kg⁻¹ but it is still outstanding when compared with other aqueous rechargeable batteries [263]. The other example has been mentioned in ionic liquid section that ionic liquids like PP14TFSI and PP₁₄NTF₂ act as both solvents and active salts simultaneously. By using graphite as both electrodes, a free-metal system is created. In contrast to the aqueous electrolyte-based example, the cells have wider working potential (1–5 V) but relative low capacity offsets their potential for high energy density. Besides, ionic liquids are still expensive to produce which also overshadows their future on low cost rechargeable devices [60,71].

To date, intense studies have been done on finding more sustainable alternatives for Li⁺ in DIBs. Under the circumstances, Na-, K-, Zn-, Ca-, Aland metal free cations-based DIBs have been emerged in the past decades. However, they still exhibit some serious shortcomings that make them unable to compete with conventional Li-DIBs. For monovalent cations containing Na⁺ and K⁺, they suffer from sluggish transfer within negative electrodes, poor cyclic stability/reversibility and limited capacity due to relatively large ionic radius. Accordingly, the application of alloying-type and adsorption-type materials instead of the insertion-type help improve the situation, though the performance is still inferior to the Li-DIBs counterparts. For multivalent cations-based DIBs, research on Znand Ca-DIBs are still at its infant stage with low capacity and energy density. In comparison, the Al-DIBs have already been hot-debated for many years and the configuration with graphite electrodes and ionic liquid electrolytes delivers relatively large capacity, good cyclic stability and rate capability, which is partially ascribed to the facile transfer of AlCl₄ anions between graphite electrodes. Considering the Al abundance in nature, the Al-DIBs is a promising alternative for Li-DIBs. Lastly, metalfree cations which are derived from pure ionic liquids or salts dissolved in aqueous electrolytes are also proven feasible in DIBs system. Nevertheless, the DIBs based on the cations deliver fairly poor performances which overshadows their potential for cost-saving and hinders their further development.

6. Challenges and outlook

DIBs become an important part of the next-generation rechargeable battery technologies. Applying graphite as both electrodes is an important branch of DIBs and the so-called DGBs or DCBs are studied for the longest time and are the most promising ones for broad application. Compared to the conventional LIBs, the high working potential (>4.5 V) of DIBs promises the ways for enhancing energy density. In addition, free lithium in electrodes helps cut the overall cost to a much lower level which is especially precious in the condition of shorting natural resources. The symmetric configuration also allows the switchable polarity during working, which means, full cells could be charged/discharged on both directions [359]. This characteristic would help avoid the active materials structural damage and further the safety concerns like the fire or explosion brought by wrongly charging in the opposite direction for regular cells. However, the high potential exceeds the working potential range of many organic electrolytes and the decomposition of the electrolyte would lead to the fast failure of full battery. On this point, electrolyte selection and development in high-voltage LIBs are good examples for DIBs to follow. For a reversible and stable cycling, several methods are proven feasible including ionic liquid electrolytes, highly concentrated electrolytes and adjustment of electrolyte composition or introduction of extra additives. Among them, the highly concentrated electrolytes are considered one of the most practical and promising options for future DIBs due to several intriguing features like enlarged stable potential range, suppression of corrosion on current collectors, improvement on delivered capacity and compatible CEI/SEI layer on both electrode surfaces, which clearly overweight the intrinsic disadvantage of high price. Besides, it should be noted that few works in DIBs focus on the additives within organic solvents to improve overall reversibility and cycling stability [70,83,105,278,304], in sharp contrast to a large amount of feasible additives reported in high-voltage LIBs, which are powered by electrochemical-induced polymerization or decomposition of additives to form an effective CEI layer on the surface of positive electrode materials. With more focus on the additives in electrolytes or directly transplant proven-feasible additives from high-voltage LIBs, overall performances of DIBs are supposed to improve [360]. The relatively low capacity, ranging from $80 \,\mathrm{mAh \cdot g}^{-1}$ to $150\,\mathrm{mA}\,\mathrm{h\cdot g}^{-1}$ as reported in literature, is another critical shortcoming for today's DIBs, which makes it uncompetitive with LIBs [50,117]. This is ascribed to the limited active sites within electrodes to some extent, in which positive electrode is the major limiting factor. From this perspective, intercalation-type graphite is not a good choice due to its low theoretical capacity. Some novel electrodes are needed with much higher capacity. Among the hosting mechanisms, the potential alternative materials for graphite on positive electrode side are mainly dependent on adsorption/desorption mechanism including the p-type organics and doped carbonaceous materials since it is possible to increase the amounts of active sites. They also exhibit other attractive features like the feasible way of anions uptake/release, free volume change brought by large anion intercalation/de-intercalation, low cost and great abundance of their composing elements. In addition, some materials like BiF3 and Fe(C₂H₅)₂ which possess quite low working potential for anion insertion/de-insertion, sometimes even lower than working potential of cation-hosting materials, make the aqueous electrolytes applicable in the DIBs system (as a reverse DIB). Aqueous solvent allows the rapid diffusion of ions and has advantages of high safety, low cost and environmental benign. Furthermore, several studies based on BiF3 present promising performances like high specific capacity over 120 mA h·g⁻¹ and superior rate capability [113,114]. For negative electrode materials, plating/stripping mechanism (i.e. Li metal with Li cations in electrolytes) is most encouraging due to the highest theoretical capacity and widest working potential range of full cells. Regarding the growth of hazardous dendrite growth, some effective methods have been studied. Unfortunately, few works focus on lithium-metal-based DIBs. Next to it is the alloying-type negative electrodes as they also offer high theoretical

capacity and the metal negative electrodes could act for multiple functions as current collectors and cation-hosting materials to cut overall mass, and thus increase the energy density. The severe volume expansion during cycling could be buffered through surface modification and structure tuning.

As the concept of DIBs just emerged for 8 years, the systematic research is still at the initial stage and there are many technical challenges that need more studies. Energy density, cycling stability/reversibility and capacity, rate performance, cost and security are the most basic issues to consider for designing and improving DIBs. If DIBs are to ever be deployed in large-scale battery systems, improvements in material properties and battery performance must come without compromising the overall cost. Gradual replacement of scarce elements (i.e. Li) with earth-abundant elements (e.g. Na, K, Al, N, C, S) as charge carriers is encouraged in the future development. And it should be noted that a standard is needed for calculating the energy density of DIBs. Different from conventional LIBs, electrolytes in DIBs are the sources of charge carriers and should also be counted as active mass for calculation. In literature, the mix of different calculation standards brings troubles for evaluating the performances of cells [195,257,261]. Besides, some gases are possible to release as organic electrolyte decomposes under high working potential and heat produced during cycling may aggravate the harm [361]. Nevertheless, few comprehensive report for DIBs safety hasn't been seen so far regarding the routine safety testing like nail penetrating test, cell extrusion test and short-circuit test for DIBs. As few papers discussed these issues [85,362], it is necessary to have more considerations at this development stage of DIBs. DIBs possess potentially attractive properties/performance and present some potentials as next-generation rechargeable batteries but there are still a lot of technical and scientific issues uncertain, which need more efforts to explore.

Declaration of competing interest

All of the authors declare there is no interest conflict.

Acknowledgement

This work was supported in part by the National Science Foundation (CBET 1803256). The authors extend their appreciation to the International Scientific Partnership Program ISPP at King Saud University for funding this research work through ISPP-139.

References

- D. Campbell-Lendrum, A. Prüss-Ustün, Climate change, air pollution and noncommunicable diseases, Bull. World Health Organ. 97 (2) (2019) 160–161.
- [2] J. Goldemberg, et al., Household air pollution, health, and climate change: cleaning the air, Environ. Res. Lett. 13 (3) (2018), 030201.
- [3] EIA, International energy Outlook 2017, Int. Energy Outlook 2017 (2017).
- [4] D.o.E.a.S. Affairs, World Population Prospects: the 2015 Revision. World Population Prospects: the 2015 Revision, Department of Economic and Social Affairs, United Nations, 2015.
- [5] M. Hosenuzzaman, et al., Global prospects, progress, policies, and environmental impact of solar photovoltaic power generation, Renew. Sustain. Energy Rev. 41 (2015) 284–297.
- [6] J.M. Frost, A. Walsh, What is moving in hybrid halide perovskite solar cells? Accounts Chem. Res. 49 (3) (2016) 528–535.
- [7] N.H. Tiep, Z.L. Ku, H.J. Fan, Recent advances in improving the stability of perovskite solar cells, Adv. Energy Mater. 6 (3) (2016) 1501420.
- [8] Z. Liang, et al., ZnO cathode buffer layers for inverted polymer solar cells, Energy Environ. Sci. 8 (12) (2015) 3442–3476.
- [9] Q. Li, et al., Solar energy storage in the rechargeable batteries, Nano Today 16 (2017) 46–60.
- [10] J.H. Montoya, et al., Materials for solar fuels and chemicals, Nat. Mater. 16 (1) (2016) 70–81.
- [11] K.L. Buchheit, et al., Techno-economic analysis of a sustainable coal, wind, and nuclear hybrid energy system, Energy Fuels 30 (12) (2016) 10721–10729.
- [12] M. Cheng, Y. Zhu, The state of the art of wind energy conversion systems and technologies: a review, Energy Convers. Manag. 88 (2014) 332–347.
- [13] T. Mesbahi, et al., A stand-alone wind power supply with a Li-ion battery energy storage system, Renew. Sustain. Energy Rev. 40 (2014) 204–213.

- [14] Y. Zhao, et al., Layered double hydroxide nanostructured photocatalysts for renewable energy production, Adv. Energy Mater. 6 (6) (2016) 1501974.
- [15] L. Yong, Functional nanostructuring for efficient energy conversion and storage, Adv. Energy Mater. 6 (23) (2016) 1600461.
- [16] Z.L. Wang, Triboelectric nanogenerators as new energy technology for self-powered systems and as active mechanical and chemical sensors, ACS Nano 7 (11) (2013) 9533–9557.
- [17] F.-R. Fan, et al., Transparent triboelectric nanogenerators and self-powered pressure sensors based on micropatterned plastic films, Nano Lett. 12 (6) (2012) 3109–3114.
- [18] S. Niu, et al., Theoretical study of contact-mode triboelectric nanogenerators as an effective power source, Energy Environ. Sci. 6 (12) (2013) 3576–3583.
- [19] M.S. Whittingham, Electrical energy storage and intercalation chemistry, Science 192 (4244) (1976) 1126–1127.
- [20] J. Perkins, Materials and mechanisms determining the performance of lead-acid storage batteries an invited review, Mater. Sci. Eng. 28 (2) (1977) 167–199.
- [21] A. Manthiram, Y. Fu, Y.-S. Su, Challenges and prospects of lithium-sulfur batteries, Accounts Chem. Res. 46 (5) (2013) 1125–1134.
- [22] M.S. Whittingham, C. Siu, J. Ding, Can multielectron intercalation reactions Be the basis of next generation batteries? Accounts Chem. Res. 51 (2) (2018) 258–264.
- [23] A. Eftekhari, Z. Jian, X. Ji, Potassium secondary batteries, ACS Appl. Mater. Interfaces 9 (5) (2017) 4404–4419.
- [24] J.B. Goodenough, Changing Outlook for rechargeable batteries, ACS Catal. 7 (2) (2017) 1132–1135.
- [25] W.-J. Kwak, et al., Controversial topics on lithium superoxide in Li–O2 batteries, ACS Energy Lett. 2 (2017) 2756–2760.
- [26] C. Zhou, S. Bag, V. Thangadurai, Engineering materials for progressive all-solid-
- state Na batteries, ACS Energy Lett. 3 (9) (2018) 2181–2198.

 [27] P. Barpanda, et al., Polyanionic insertion materials for sodium-ion batteries, Adv.
- Energy Mater. 8 (2018) 1703055.

 [28] D. Bin, et al., Progress in aqueous rechargeable sodium-ion batteries, Adv. Energy
- Mater. 8 (2018) 1703008.

 [29] Y. Shao, et al., Making Li-air batteries rechargeable: material challenges, Adv.
- Funct. Mater. 23 (8) (2013) 987–1004.
- [30] M.D. Slater, et al., Sodium-ion batteries, Adv. Funct. Mater. 23 (8) (2013) 947–958.
- [31] J. Fu, et al., Electrically rechargeable zinc-air batteries: progress, challenges, and perspectives, Adv. Mater. 29 (2016) 1604685.
- [32] R.J. Gummow, et al., Calcium-ion batteries: current state-of-the-art and future perspectives, Adv. Mater. 30 (39) (2018) 1801702.
- [33] H. Yadegari, Q. Sun, X. Sun, Sodium-oxygen batteries: a comparative review from chemical and electrochemical fundamentals to future perspective, Adv. Mater. 28 (33) (2016) 7065–7093.
- [34] H. Kim, et al., Aqueous rechargeable Li and Na ion batteries, Chem. Rev. 114 (23) (2014) 11788–11827.
- [35] A. Manthiram, et al., Rechargeable lithium-sulfur batteries, Chem. Rev. 114 (23) (2014) 11751–11787.
- [36] M.S. Whittingham, Lithium batteries and cathode materials, Chem. Rev. 104 (10) (2004) 4271–4302.
- [37] N. Yabuuchi, et al., Research development on sodium-ion batteries, Chem. Rev. 114 (23) (2014) 11636–11682.
- [38] F. Li, H. Kitaura, H. Zhou, The pursuit of rechargeable solid-state Li-air batteries, Energy Environ. Sci. 6 (8) (2013) 2302–2311.
- [39] H.D. Yoo, et al., Mg rechargeable batteries: an on-going challenge, Energy Environ. Sci. 6 (8) (2013) 2265–2279.
- [40] M. Zhao, et al., Metal-organic frameworks as selectivity regulators for hydrogenation reactions, Nature 539 (2016) 76.
- [41] A. Yoshino, The birth of the lithium-ion battery, Angew. Chem. Int. Ed. 51 (24) (2012) 5798–5800.
- [42] A. Manthiram, An Outlook on lithium ion battery technology, ACS Cent. Sci. 3 (10) (2017) 1063–1069.
- [43] M. Winter, B. Barnett, K. Xu, Before Li ion batteries, Chem. Rev. 118 (23) (2018) 11433–11456.
- [44] B. Scrosati, J. Hassoun, Y.-K. Sun, Lithium-ion batteries. A look into the future, Energy Environ. Sci. 4 (9) (2011) 3287–3295.
- [45] L. Lu, et al., A review on the key issues for lithium-ion battery management in electric vehicles, J. Power Sources 226 (2013) 272–288.
- [46] N. Nitta, et al., Li-ion battery materials: present and future, Mater. Today 18 (5) (2015) 252–264.
- [47] J.B. Goodenough, K.-S. Park, The Li-ion rechargeable battery: a perspective, J. Am. Chem. Soc. 135 (4) (2013) 1167–1176.
- [48] C. Liu, Z.G. Neale, G. Cao, Understanding electrochemical potentials of cathode materials in rechargeable batteries, Mater. Today 19 (2) (2016) 109–123.
- [49] J.B. Goodenough, Y. Kim, Challenges for rechargeable batteries, J. Power Sources 196 (16) (2011) 6688–6694.
- [50] C. Liu, G. Cao, Fundamentals of rechargeable batteries and electrochemical potentials of electrode materials, in: D. Wang, G. Cao (Eds.), Nanomaterials for Energy Conversion and Storage, WORLD SCIENTIFIC, 2018, pp. 397–451 (EUROPE).
- [51] C. Liu, et al., A promising cathode for Li-ion batteries: Li3V2(PO4)3, Energy Storage Mater. 4 (2016) 15–58.
- [52] S.W. Kim, et al., Electrode materials for rechargeable sodium-ion batteries: potential alternatives to current lithium-ion batteries, Adv. Energy Mater. 2 (7) (2012) 710–721.
- [53] J.M. Tarascon, M. Armand, Issues and challenges facing rechargeable lithium batteries, Nature 414 (2001) 359.

- [54] M. Armand, J.M. Tarascon, Building better batteries, Nature 451 (2008) 652.
- [55] B. Scrosati, Recent advances in lithium ion battery materials, Electrochim. Acta 45 (15) (2000) 2461–2466.
- [56] M.R. Palacín, Recent advances in rechargeable battery materials: a chemist's perspective, Chem. Soc. Rev. 38 (9) (2009) 2565–2575.
- [57] B. Dunn, H. Kamath, J.-M. Tarascon, Electrical energy storage for the grid: a battery of choices, Science 334 (6058) (2011) 928–935.
- [58] K. Brandt, Historical development of secondary lithium batteries, Solid State Ion. 69 (3) (1994) 173–183.
- [59] S. Dong, et al., A novel coronene//Na₂Ti₃O₇ dual-ion battery, Nano Energy 40 (2017) 233–239.
- [60] Z.Z. J Fan, Y. liu, et al., An excellent rechargeable PP₁₄TFSI ionic liquid dual-ion battery, Chem. Commun. 53 (51) (2017) 6891.
- [61] R.C. Massé, et al., Energy storage through intercalation reactions: electrodes for rechargeable batteries, Natl. Sci. Rev. 4 (1) (2017) 26–53.
- [62] C. Vaalma, et al., A cost and resource analysis of sodium-ion batteries, Nat. Rev. Mater. 3 (2018) 18013.
- [63] K. Luo, et al., Charge-compensation in 3d-transition-metal-oxide intercalation cathodes through the generation of localized electron holes on oxygen, Nat. Chem. 8 (2016) 684.
- [64] M. Sathiya, et al., Reversible anionic redox chemistry in high-capacity layeredoxide electrodes, Nat. Mater. 12 (2013) 827.
- [65] H. Vikström, S. Davidsson, M. Höök, Lithium availability and future production outlooks, Appl. Energy 110 (2013) 252–266.
- [66] N. Gunawardhana, et al., Constructing a novel and safer energy storing system using a graphite cathode and a MoO_3 anode, J. Power Sources 196 (18) (2011) 7886–7890.
- [67] H.S.Y. Nakano, T. Morishita, et al., Anion secondary batteries Utilizing a reversible BF4 insertion/extraction two dimensional Si material, J. Mater. Chem. 2 (20) (2014) 758–7592.
- [68] W. Xu, et al., Lithium metal anodes for rechargeable batteries, Energy Environ. Sci. 7 (2) (2014) 513–537.
- [69] M.S. Whittingham, History, evolution, and future status of energy storage, Proc. IEEE 100 (2012) 1518–1534. Special Centennial Issue.
- [70] J.A.,C.A.V. Read, M.H. Ervin, et al., Dual-graphite chemistry enabled by a high voltage electrolyte, Energy Environ. Sci. 7 (2) (2014) 617–620.
- [71] Z. Li, et al., A novel graphite-based dual ion battery using PP14NTF2 ionic liquid for preparing graphene structure, Carbon 138 (2018) 52–60.
- [72] W. Märkle, et al., The influence of electrolyte and graphite type on the PF₆ intercalation behaviour at high potentials, Carbon 47 (11) (2009) 2727–2732.
- [73] P. Meister, et al., Dual-ion cells based on the electrochemical intercalation of asymmetric fluorosulfonyl-(trifluoromethanesulfonyl) imide anions into graphite, Electrochim. Acta 130 (2014) 625–633.
- [74] J.A. Seel, J.R. Dahn, Electrochemical Intercalation of PF₆ into graphite, J. Electrochem. Soc. 147 (3) (2000) 892–898.
- [75] N.P.W. Pieczonka, et al., Understanding transition-metal dissolution behavior in LiNi0.5Mn1.5O4 high-voltage spinel for lithium ion batteries, J. Phys. Chem. C 117 (31) (2013) 15947–15957.
- [76] M. Hu, X. Pang, Z. Zhou, Recent progress in high-voltage lithium ion batteries, J. Power Sources 237 (2013) 229–242.
- [77] D. Larcher, J.M. Tarascon, Towards greener and more sustainable batteries for electrical energy storage, Nat. Chem. 7 (1) (2015) 19–29.
- [78] J.W. Choi, D. Aurbach, Promise and reality of post-lithium-ion batteries with high energy densities, Nat. Rev. Mater. 1 (2016) 16013.
- [79] J. Lopez, et al., Designing polymers for advanced battery chemistries, Nat. Rev. Mater. 4 (2019) 312–330.
- [80] J.B. Goodenough, Y. Kim, Challenges for rechargeable Li batteries, Chem. Mater. 22 (3) (2010) 587–603.
- [81] X. Zhou, et al., Beyond conventional batteries: strategies towards low-cost dualion batteries with high performance, Angew. Chem. Int. Ed. (2019), https:// doi.org/10.1002/anie.201814294.
- [82] I.A. Rodríguez-Pérez, X. Ji, Anion hosting cathodes in dual-ion batteries, ACS Energy Lett. 2 (8) (2017) 1762–1770.
- [83] S. Aladinli, et al., Anion intercalation into a graphite cathode from various sodium-based electrolyte mixtures for dual-ion battery applications, Electrochim. Acta 231 (2017) 468–478.
- [84] L. Michael, J.R.L. Aubrey, A dual-ion battery cathode via oxidative insertion of anions in a metal-organic framework, J. Am. Chem. Soc. 137 (42) (2015) 13594–13602.
- [85] Q. Liu, et al., Low cost and superior safety industrial grade lithium dual-ion batteries with a second life, Energy Technol. 6 (10) (2018) 1994–2000.
- [86] T. Placke, et al., Lithium ion, lithium metal, and alternative rechargeable battery technologies: the odyssey for high energy density, J. Solid State Electrochem. 21 (7) (2017) 1939–1964.
- [87] R. Marom, et al., A review of advanced and practical lithium battery materials, J. Mater. Chem. 21 (27) (2011) 9938–9954.
- [88] W. Rüdorff, U. Hofmann, Über Graphitsalze, Z. Anorg. Allg. Chem. 238 (1938) 1–50.
- [89] M. Armand, P. Touzain, Graphite intercalation compounds as cathode materials, Mater. Sci. Eng. 31 (1977) 319–329.
- [90] J.S. Dunning, et al., A secondary, nonaqueous solvent battery, J. Electrochem. Soc. 118 (12) (1971) 1886.
- [91] F.P.,L.C.A. McCullough, R.V.U.S. Snelgrove, Patent 4 (1989) 830-938.
- [92] T. Ishihara, M. Koga, H. Matsumoto, et al., Electrochemical intercalation of hexafluorophosphate anion into various carbons for cathode of dual-carbon rechargeable battery, Electrochem. Solid State Lett. 10 (3) (2007) A74–A76.

- [93] R.T. Carlin, et al., Dual intercalating molten electrolyte batteries, J. Electrochem. Soc. 141 (7) (1994) L73–L76.
- [94] J.R. Dahn, J.A. Steel, Energy and capacity projections for practical dual-graphite cells, J. Electrochem. Soc. 147 (3) (2000) 899–901.
- [95] C. Grosjean, et al., Assessment of world lithium resources and consequences of their geographic distribution on the expected development of the electric vehicle industry, Renew. Sustain. Energy Rev. 16 (3) (2012) 1735–1744.
- [96] F.O. Placke T, S.F. Lux, et al., Reversible intercalation of bis(trifluoromethanesulfonyl)imide anions from an ionic liquid electrolyte into graphite for high performance dual-ion cells, J. Electrochem. Soc. 159 (11) (2012) A1755–A1765.
- [97] M.L. Aubrey, J.R. Long, A dual-ion battery cathode via oxidative insertion of anions in a metal-organic framework, J. Am. Chem. Soc. 137 (42) (2015) 13594–13602.
- [98] M.E. Speer, et al., Thianthrene-functionalized polynorbornenes as high-voltage materials for organic cathode-based dual-ion batteries, Chem. Commun. 51 (83) (2015) 15261–15264.
- [99] F. Bordet, et al., Anion intercalation into graphite from a sodium-containing electrolyte, Electrochim. Acta 174 (2015) 1317–1323.
- [100] M.-C. Lin, et al., An ultrafast rechargeable aluminium-ion battery, Nature 520 (2015) 324.
- [101] M. Wang, et al., Reversible calcium alloying enables a practical room-temperature rechargeable calcium-ion battery with a high discharge voltage, Nat. Chem. 10 (6) (2018).
- [102] B. Ji, et al., A novel potassium-ion-based dual-ion battery, Adv. Mater. 29 (19) (2017) 1700519.
- [103] H. Glatz, et al., An organic cathode based dual-ion aqueous zinc battery enabled by a cellulose membrane, ACS Appl. Energy Mater. 2 (2) (2019) 1288–1294.
- [104] M. Wang, Y. Tang, A review on the features and progress of dual-ion batteries, Adv. Energy Mater. 8 (19) (2018) 1703320.
- [105] F. Zhang, et al., A dual-ion battery constructed with aluminum foil anode and mesocarbon microbead cathode via an alloying/intercalation process in an ionic liquid electrolyte, Adv. Mater. Interfaces 3 (23) (2016) 1600605.
- [106] X.L. Zhang, et al., A novel aluminum-graphite dual-ion battery, Adv. Energy Mater. 6 (11) (2016) 1502588.
- [107] Z. Tan, et al., Fabrication of porous Sn-C composites with high initial coulomb efficiency and good cyclic performance for lithium ion batteries, J. Mater. Chem. 1 (33) (2013) 9462–9468.
- [108] Z. Zhang, et al., Aqueous rechargeable dual-ion battery based on fluoride ion and sodium ion electrochemistry, J. Mater. Chem. 6 (2018) 8244–8250.
- [109] J.Y. Luo, Y.Y. Xia, Aqueous lithium-ion battery LiTi2(PO4)3/LiMn2O4 with high power and energy densities as well as superior cycling stability, Adv. Funct. Mater. 17 (18) (2010) 3877–3884.
- [110] D. Su, et al., High-capacity aqueous potassium-ion batteries for large-scale energy storage, Adv. Mater. 29 (1) (2016) 1604007.
- [111] F. Beck, P. Rüetschi, Rechargeable batteries with aqueous electrolytes, Electrochim. Acta 45 (15) (2000) 2467–2482.
- [112] N. Alias, A.A. Mohamad, Advances of aqueous rechargeable lithium-ion battery: a review, J. Power Sources 274 (2015) 237–251.
- [113] X. Wu, et al., Reverse dual-ion battery via a ZnCl2 water-in-salt electrolyte, J. Am. Chem. Soc. 141 (15) (2019) 6338–6344.
- [114] H. Jiang, et al., An aqueous dual-ion battery cathode of Mn3O4 via reversible insertion of nitrate, Angew. Chem. Int. Ed. 58 (16) (2019) 5286–5291.
- [115] T. Placke, et al., Perspective on performance, cost, and technical challenges for practical dual-ion batteries, Joule 2 (12) (2018) 2528–2550.
- [116] J. Hao, et al., Recent progress and perspectives on dual-ion batteries, EnergyChem 1 (1) (2019) 100004.
- [117] K.V. Kravchyk, M.V. Kovalenko, Rechargeable dual-ion batteries with graphite as a cathode: key challenges and opportunities, Adv. Energy Mater. 9 (2019) 1901749.
- [118] X. Jiang, et al., Electrolytes for dual-carbon batteries, ChemElectroChem 6 (10) (2019) 2615–2629.
- [119] M. Zhang, et al., Rechargeable batteries based on anion intercalation graphite cathodes, Energy Storage Mater. 16 (2019) 65–84.
- [120] E. Memarzadeh Lotfabad, et al., Origin of non-SEI related coulombic efficiency loss in carbons tested against Na and Li, J. Mater. Chem. 2 (46) (2014) 19685–19695.
- [121] Y. He, et al., Alumina-coated patterned amorphous silicon as the anode for a lithium-ion battery with high coulombic efficiency, Adv. Mater. 23 (42) (2011) 4938–4941.
- [122] G. Venugopal, et al., Characterization of microporous separators for lithium-ion batteries, J. Power Sources 77 (1) (1999) 34–41.
- [123] M.-H. Ryou, et al., Mussel-inspired polydopamine-treated polyethylene separators for high-power Li-ion batteries, Adv. Mater. 23 (27) (2011) 3066–3070.
- [124] P. Arora, Z. Zhang, Battery separators, Chem. Rev. 104 (10) (2004) 4419–4462.
- [125] L.-X. Yuan, et al., Development and challenges of LiFePO4 cathode material for lithium-ion batteries, Energy Environ. Sci. 4 (2) (2011) 269–284.
- [126] X. Shi, et al., (EMIm)⁺(PF₆)⁻ ionic liquid unlocks optimum energy/power density for architecture of nanocarbon-based dual-ion battery, Adv. Energy Mater. 6 (24) (2016) 1601378.
- [127] X. Zhang, et al., LiNi0.5Mn1.5O4 porous nanorods as high-rate and long-life cathodes for Li-ion batteries, Nano Lett. 13 (6) (2013) 2822–2825.
- [128] A. Kraytsberg, Y. Ein-Eli, Higher, stronger, better a review of 5 Volt cathode materials for advanced lithium-ion batteries, Adv. Energy Mater. 2 (8) (2012) 2020, 2020.
- [129] J. Shim, K.A. Striebel, Cycling performance of low-cost lithium ion batteries with natural graphite and LiFePO4, J. Power Sources 119–121 (2003) 955–958.

- [130] J. Li, Z.-F. Ma, Past and present of LiFePO4: from fundamental research to industrial applications, Chem 5 (1) (2019) 3–6.
- [131] Y. Takahashi, et al., Structure and electron density analysis of electrochemically and chemically delithiated LiCoO2 single crystals, J. Solid State Chem. 180 (1) (2007) 313–321.
- [132] K. Edström, T. Gustafsson, J.O. Thomas, The cathode–electrolyte interface in the Li-ion battery, Electrochim. Acta 50 (2) (2004) 397–403.
- [133] J. Kasnatscheew, et al., The truth about the 1st cycle Coulombic efficiency of LiNi1/3Co1/3Mn1/3O2 (NCM) cathodes, Phys. Chem. Chem. Phys. 18 (5) (2016) 3956–3965.
- [134] K. Parvez, et al., Exfoliation of graphite into graphene in aqueous solutions of inorganic salts, J. Am. Chem. Soc. 136 (16) (2014) 6083–6091.
- [135] M. Zheng, et al., Hierarchically nanostructured transition metal oxides for lithiumion batteries, Adv. Sci. 5 (3) (2018) 1700592.
- [136] M. Winter, et al., Insertion electrode materials for rechargeable lithium batteries, Adv. Mater. 10 (10) (2010) 725–763.
- [137] R. Sengupta, et al., A review on the mechanical and electrical properties of graphite and modified graphite reinforced polymer composites, Prog. Polym. Sci. 36 (5) (2011) 638–670.
- [138] S. Flandrois, B. Simon, Carbon materials for lithium-ion rechargeable batteries, Carbon 37 (2) (1999) 165–180.
- [139] J. Chen, F. Cheng, Combination of lightweight elements and nanostructured materials for batteries, Accounts Chem. Res. 42 (6) (2009) 713–723.
- [140] A. Sakhaee-Pour, Elastic properties of single-layered graphene sheet, Solid State Commun. 149 (1) (2009) 91–95.
- [141] C. Lee, et al., Measurement of the elastic properties and intrinsic strength of monolayer graphene, Science 321 (5887) (2008) 385–388.
- [142] M.C. Wang, et al., Effect of defects on fracture strength of graphene sheets, Comput. Mater. Sci. 54 (2012) 236–239.
- [143] M.S. Fuhrer, C.N. Lau, A.H. MacDonald, Graphene: materially better carbon, MRS Bull. 35 (4) (2010) 289–295.
- [144] S.V. Morozov, et al., Giant intrinsic carrier mobilities in graphene and its bilayer, Phys. Rev. Lett. 100 (1) (2008), 016602.
- [145] A.S. Mayorov, et al., Micrometer-scale ballistic transport in encapsulated graphene at room temperature, Nano Lett. 11 (6) (2011) 2396–2399.
- [146] T. Placke, et al., In situ X-ray diffraction studies of cation and anion inter-calation into graphitic carbons for electrochemical energy storage applications, Z. Anorg. Allg. Chem. 640 (10) (2014) 1996–2006.
- [147] G. Schmuelling, et al., X-ray diffraction studies of the electrochemical intercalation of bis(trifluoromethanesulfonyl)imide anions into graphite for dual-ion cells, J. Power Sources 239 (2013) 563–571.
- [148] W. Rüdorff, Kristallstruktur der Säureverbindungen des Graphits. Zeitschrift für Physikalische Chemie, 1940, p. 42.
- [149] H. Zabel, A. Magerl, J.J. Rush, Phonons in LiC₆, Phys. Rev. B 27 (6) (1983) 3930–3933.
- [150] N. Daumas, A H, Relations between phase concept and reaction mechanics in graphite insertion compounds, C. R. Acad. Sci. 268 (878) (1969) 373.
- [151] M. Balabajew, et al., In-situ Raman study of the intercalation of bis(trifluoromethylsulfonyl)imid ions into graphite inside a dual-ion cell, Electrochim. Acta 211 (2016) 679–688.
- [152] P. Meister, et al., New insights into the uptake/release of FTFSI⁻ anions into graphite by means of in situ powder X-ray diffraction, Electrochem. Commun. 71 (2016) 52–55.
- [153] X. Zhang, N. Sukpirom, M.M. Lerner, Graphite intercalation of bis(trifluoromethanesulfonyl) imide and other anions with perfluoroalkanesulfonyl substituents, Mater. Res. Bull. 34 (3) (1999) 363–372.
- [154] J.A. Read, In-situ studies on the electrochemical intercalation of hexafluorophosphate anion in graphite with selective cointercalation of solvent, J. Phys. Chem. C 119 (16) (2015) 8438–8446.
- [155] B. Özmen-Monkul, M.M. Lerner, The first graphite intercalation compounds containing tris(pentafluoroethyl)trifluorophosphate, Carbon 48 (11) (2010) 3205–3210.
- [156] F. Tuinstra, J.L. Koenig, Raman spectrum of graphite, J. Chem. Phys. 53 (3) (1970) 1126–1130.
- [157] A.C. Ferrari, D.M. Basko, Raman spectroscopy as a versatile tool for studying the properties of graphene, Nat. Nanotechnol. 8 (2013) 235.
- [158] A. Ferrari, et al., Raman spectroscopy of graphite, Philos. Trans. R. Soc. London, Ser. A: Math. Phys. Eng. Sci. 362 (1824) (2004) 2271–2288.
- [159] A.C. Ferrari, Raman spectroscopy of graphene and graphite: disorder, electron-phonon coupling, doping and nonadiabatic effects, Solid State Commun. 143 (1) (2007) 47–57.
- [160] A. Das, et al., Phonon renormalization in doped bilayer graphene, Phys. Rev. B 79 (15) (2009) 155417.
- [161] J.C. Chacóntorres, L. Wirtz, T. Pichler, Manifestation of charged and strained graphene layers in the Raman response of graphite intercalation compounds, ACS Nano 7 (10) (2013) 9249–9259.
- [162] H. Fan, L. Qi, H. Wang, Intercalation behavior of hexafluorophosphate into graphite electrode from propylene/ethylmethyl carbonates, J. Electrochem. Soc. 164 (9) (2017) A2262–A2267.
- [163] H. Zabel, S.P.D. Stuart, Graphite Intercalation Compounds I, Springer Berlin Heidelberg, 1990, pp. 320–321.
- [164] Q. Shi, et al., High-performance sodium metal anodes enabled by a bifunctional potassium salt, Angew. Chem. 130 (29) (2018) 9207–9210.
- [165] D.P. DiVincenzo, E.J. Mele, Cohesion and structure in stage-1 graphite intercalation compounds, Phys. Rev. B 32 (4) (1985) 2538–2553.

- [166] K. Ozawa, Lithium-ion rechargeable batteries with LiCoO2 and carbon electrodes: the LiCoO2/C system, Solid State Ion. 69 (3) (1994) 212–221.
- [167] J. Jiang, J.R. Dahn, Effects of solvents and salts on the thermal stability of LiC6, Electrochim. Acta 49 (26) (2004) 4599–4604.
- [168] P.W. Ruch, et al., In situ X-ray diffraction of the intercalation of $(C_2H_5)_4N^+$ and BF_4^- into graphite from acetonitrile and propylene carbonate based supercapacitor electrolytes, Electrochim. Acta 53 (3) (2007) 1074–1082.
- [169] G.C. Chung, et al., Origin of graphite exfoliation an investigation of the important role of solvent cointercalation, J. Electrochem. Soc. 147 (12) (2000) 4391–4398.
- [170] W. Zhou, et al., Joint theoretical and experimental study on the effects of the salts in the graphite-based dual-ion batteries, J. Phys. Chem. C 123 (30) (2019) 18132–18141.
- [171] R. Tian, et al., Quantifying the factors limiting rate performance in battery electrodes, Nat. Commun. 10 (1) (2019) 1933.
- [172] S. Miyoshi, et al., Fast Diffusivity of PF₆ Anions in graphitic Carbon for a dualcarbon rechargeable battery with superior rate property, J. Phys. Chem. C 120 (40) (2016) 22887–22894.
- [173] P.P. Prosini, et al., Determination of the chemical diffusion coefficient of lithium in LiFePO4, Solid State Ion. 148 (1) (2002) 45–51.
- [174] K. Persson, et al., Lithium diffusion in graphitic carbon, J. Phys. Chem. Lett. 1 (8) (2010) 1176–1180.
- (2010) 1176–1180.
 [175] A. Eftekhari, Lithium-ion batteries with high rate capabilities, ACS Sustain. Chem.
- Eng. 5 (4) (2017) 2799–2816.
 [176] A. Heckmann, et al., New insights into electrochemical anion intercalation into carbonaceous materials for dual-ion batteries: impact of graphitization degree, Carbon 131 (2018) 201–212.
- [177] W.J. Lee, et al., Nitrogen-doped carbon nanotubes and graphene composite structures for energy and catalytic applications, Chem. Commun. 50 (52) (2014) 6818–6830
- [178] H. Chen, et al., A defect-free principle for advanced graphene cathode of aluminum-ion battery, Adv. Mater. 29 (12) (2017) 1605958.
- [179] T.J. Davies, M.E. Hyde, R.G. Compton, Nanotrench arrays reveal insight into graphite electrochemistry, Angew. Chem. 117 (32) (2010) 5251–5256.
- [180] M. Pumera, et al., Graphene for electrochemical sensing and biosensing, Trac. Trends Anal. Chem. 29 (9) (2010) 954–965.
- [181] T. Placke, et al., Influence of graphite surface modifications on the ratio of basal plane to "non-basal plane" surface area and on the anode performance in lithium ion batteries, J. Power Sources 200 (2012) 83–91.
- [182] W. Yuan, et al., The edge- and basal-plane-specific electrochemistry of a single-layer graphene sheet, Sci. Rep. 3 (31) (2013) 2248.
- [183] O.F. Tobias Placke, et al., Electrochemical intercalation of bis(trifluoromethanesulfonyl) imide anion into various graphites for dual-ion cells, Ecs Trans. 50 (24) (2013) 59–68.
- [184] A. Heckmann, et al., A route towards understanding the kinetic processes of bis(trifluoromethanesulfonyl) imide anion intercalation into graphite for dual-ion batteries. Electrochim. Acta 284 (2018) 669–680.
- [185] W. Du, et al., Effect of cycling rate, particle size and transport properties on lithium-ion cathode performance, Int. J. Heat Mass Transf. 53 (17) (2010) 3552–3561.
- [186] J. Ye, et al., Structural optimization of 3D porous electrodes for high-rate performance lithium ion batteries, ACS Nano 9 (2) (2015) 2194–2202.
- [187] D.Y.W. Yu, et al., Effect of electrode parameters on LiFePO4 cathodes, J. Electrochem. Soc. 153 (5) (2006) A835–A839.
- [188] J. Peng, et al., Electrochemically driven transformation of amorphous carbons to crystalline graphite nanoflakes: a facile and mild graphitization method, Angew. Chem. 129 (7) (2017) 1777–1781.
- [189] E. Zhang, et al., A novel aluminum dual-ion battery, Energy Storage Mater. 11 (2018) 91–99.
- [190] Y. Gao, et al., Understanding ultrafast rechargeable aluminum-ion battery from first-principles, J. Phys. Chem. C 121 (13) (2017) 7131–7138.
- [191] G. Wang, et al., Self-activating, capacitive anion intercalation enables high-power graphite cathodes, Adv. Mater. 30 (20) (2018) 1800533.
- [192] S. Choi, et al., Highly elastic binders integrating polyrotaxanes for silicon microparticle anodes in lithium ion batteries, Science 357 (6348) (2017) 279–283.
- [193] I. Kovalenko, et al., A major constituent of Brown algae for use in high-capacity Liion batteries, Science 334 (6052) (2011) 75–79.
- [194] C. Jiang, et al., Integrated configuration design for ultrafast rechargeable dual-ion battery, Adv. Energy Mater. 7 (19) (2017) 1700913.
- [195] S. Maohua, et al., A novel tin-graphite dual-ion battery based on sodium-ion electrolyte with high energy density, Adv. Energy Mater. 7 (7) (2017) 1601963.
- [196] H. Wang, M. Yoshio, Suppression of PF₆ intercalation into graphite by small amounts of ethylene carbonate in activated carbon/graphite capacitors, Chem. Commun. 46 (9) (2010) 1544.
- [197] S.J. An, et al., The state of understanding of the lithium-ion-battery graphite solid electrolyte interphase (SEI) and its relationship to formation cycling, Carbon 105 (2016) 52–76.
- [198] H. Schranzhofer, et al., Electrochemical impedance spectroscopy study of the SEI formation on graphite and metal electrodes, J. Power Sources 153 (2) (2006) 391–395.
- [199] W.-H. Li, et al., Highly improved cycling stability of anion de-/intercalation in the graphite cathode for dual-ion batteries, Adv. Mater. 31 (4) (2019) 1804766.
- [200] X. Han, et al., An in situ interface reinforcement strategy achieving long cycle performance of dual-ion batteries, Adv. Energy Mater. 9 (16) (2019) 1804022.
- [201] Y.-R. Zhu, et al., Increased cycling stability of Li4Ti5O12-coated LiMn1.5Ni0.5O4 as cathode material for lithium-ion batteries, Ceram. Int. 39 (3) (2013) 3087–3094.

- [202] M. Zhang, et al., A facile approach to enhance high-cutoff voltage cycle stability of LiNi0.5Co0.2Mn0.3O2 cathode materials using lithium titanium oxide, Electrochim. Acta 232 (2017) 80–88.
- [203] Y. Wang, et al., Investigation into the surface chemistry of Li4Ti5O12 nanoparticles for lithium ion batteries, ACS Appl. Mater. Interfaces 8 (39) (2016) 26008–26012.
- [204] T. Yuan, et al., Challenges of spinel Li4Ti5O12 for lithium-ion battery industrial applications, Adv. Energy Mater. 7 (12) (2017) 1601625.
- [205] J. Alvarado, et al., A carbonate-free, sulfone-based electrolyte for high-voltage Liion batteries, Mater. Today 21 (4) (2018) 341–353.
- [206] K. Xu, Electrolytes and interphases in Li-ion batteries and beyond, Chem. Rev. 114 (23) (2014) 11503–11618.
- [207] P. Novák, et al., Electrochemically active polymers for rechargeable batteries, Chem. Rev. 97 (1) (1997) 207–282.
- [208] E. Deunf, et al., A dual-ion battery using diamino-rubicene as anion-inserting positive electrode material, Electrochem. Commun. 72 (2016) 64–68.
- [209] K. Deuchert, S. Hünig, Multistage organic redox systems—a general structural principle, Angew Chem. Int. Ed. Engl. 17 (12) (1978) 875–886.
- [210] Z. Song, H. Zhou, Towards sustainable and versatile energy storage devices: an overview of organic electrode materials, Energy Environ. Sci. 6 (8) (2013) 2280–2301
- [211] S. Chen, et al., An ultrafast rechargeable hybrid sodium-based dual-ion capacitor based on hard carbon cathodes, Adv. Energy Mater. 8 (18) (2018) 1800140.
- [212] I.A. Rodríguez-Pérez, et al., A hydrocarbon cathode for dual-ion batteries, ACS Energy Lett. 1 (4) (2016) 719–723.
- [213] J.L. Bredas, G.B. Street, Polarons, bipolarons, and solitons in conducting polymers, Accounts Chem. Res. 18 (10) (1985) 309–315.
- [214] S. Dühnen, et al., Reversible anion storage in a metal-organic framework for dualion battery systems, J. Electrochem. Soc. 166 (3) (2019) A5474–A5482.
- [215] W. Deng, et al., A low cost, all-organic Na-ion battery based on polymeric cathode and anode, Sci. Rep. 3 (2013) 2671.
- [216] L. Fan, et al., An organic cathode for potassium dual-ion full battery, ACS Energy Lett. 2 (7) (2017) 1614–1620.
- [217] M. Lee, et al., Multi-electron redox phenazine for ready-to-charge organic batteries, Green Chem. 19 (13) (2017) 2980–2985.
- [218] Y. Feng, et al., Carbon foam with microporous structure for high performance symmetric potassium dual-ion capacitor, J. Energy Chem. 43 (2020) 129–138.
- [219] J. Kasnatscheew, et al., A tutorial into practical capacity and mass balancing of lithium ion batteries, J. Electrochem. Soc. 164 (12) (2017) A2479–A2486.
- [220] J. Vetter, et al., Ageing mechanisms in lithium-ion batteries, J. Power Sources 147 (1) (2005) 269–281.
- [221] H. Zheng, et al., Correlation between lithium deposition on graphite electrode and the capacity loss for LiFePO4/graphite cells, Electrochim. Acta 173 (2015) 323–330.
- [222] C.-S. Kim, et al., Effects of capacity ratios between anode and cathode on electrochemical properties for lithium polymer batteries, Electrochim. Acta 155 (2015) 431–436.
- [223] P. Arora, R.E. White, M. Doyle, Capacity fade mechanisms and side reactions in lithium-ion batteries, J. Electrochem. Soc. 145 (10) (1998) 3647–3667.
- [224] C. Bommier, X. Ji, Electrolytes, SEI formation, and binders: a review of nonelectrode factors for sodium-ion battery anodes, Small 14 (16) (2018) 1703576.
- [225] S. Fu, et al., Hydrogenation driven conductive Na2Ti3O7 nanoarrays as robust binder-free anodes for sodium-ion batteries, Nano Lett. 16 (7) (2016) 4544.
- [226] P. Senguttuvan, et al., Na2Ti3O7: lowest voltage ever reported oxide insertion electrode for sodium ion batteries, Chem. Mater. 23 (18) (2011) 4109–4111.
- [227] G. Rousse, et al., Rationalization of intercalation potential and redox mechanism for A2Ti3O7 (A = Li, Na), Chem. Mater. 25 (24) (2013) 4946–4956.
- [228] M.A. Tsiamtsouri, et al., Exfoliation of layered Na-ion anode material Na2Ti3O7 for enhanced capacity and cyclability, Chem. Mater. 30 (5) (2018) 1505–1516.
- [229] G. Park, et al., Development of a novel and safer energy storage system using a graphite cathode and Nb2O5 anode, J. Power Sources 236 (2013) 145–150.
- [230] T.-F. Yi, et al., Recent development and application of Li4Ti5O12 as anode material of lithium ion battery, J. Phys. Chem. Solids 71 (9) (2010) 1236–1242.
- [231] S.S. Zhang, The effect of the charging protocol on the cycle life of a Li-ion battery, J. Power Sources 161 (2) (2006) 1385–1391.
- [232] T. Ohzuku, A. Ueda, N. Yamamoto, Zero-strain insertion material of Li [Li1/3Ti5/3] O 4 for rechargeable lithium cells, J. Electrochem. Soc. 142 (5) (1995) 1431–1435.
- [233] E.M. Sorensen, et al., Three-dimensionally ordered macroporous Li4Ti5O12: effect of wall structure on electrochemical properties, Chem. Mater. 18 (2) (2006) 482–489.
- [234] S.-H. Park, W.-J. Lee, Hierarchically mesoporous flower-like cobalt oxide/carbon nanofiber composites with shell–core structure as anodes for lithium ion batteries, Carbon 89 (2015) 197–207.
- [235] L. Sui, et al., Integrated Co3O4/carbon fiber paper for high-performance anode of dual-ion battery, J. Energy Chem. 37 (2019) 7–12.
- [236] J. Li, et al., Phase evolution of conversion-type electrode for lithium ion batteries, Nat. Commun. 10 (1) (2019) 2224.
 [237] M.V. Reddy, G.V. Subba Rao, B.V.R. Chowdari, Metal oxides and oxysalts as anode
- materials for Li ion batteries, Chem. Rev. 113 (7) (2013) 5364–5457.

 [238] H.B. Wu, et al., Nanostructured metal oxide-based materials as advanced anodes
- [238] H.B. Wu, et al., Nanostructured metal oxide-based materials as advanced anode for lithium-ion batteries, Nanoscale 4 (8) (2012) 2526–2542.
- [239] Z. Li, et al., Hierarchical MoS2@N-doped carbon hollow spheres with enhanced performance in sodium dual-ion batteries, ChemElectroChem 6 (3) (2019) 661–667.

- [240] C. Cui, et al., Three-dimensional carbon frameworks enabling MoS2 as anode for dual ion batteries with superior sodium storage properties, Energy Storage Mater. 15 (2018) 22–30.
- [241] C.K. Chan, et al., High-performance lithium battery anodes using silicon nanowires, Nat. Nanotechnol. 3 (2007) 31.
- [242] Y. Yao, et al., Interconnected silicon hollow nanospheres for lithium-ion battery anodes with long cycle life, Nano Lett. 11 (7) (2011) 2949–2954.
- [243] I. Sultana, et al., Tin-based composite anodes for potassium-ion batteries, Chem. Commun. 52 (59) (2016) 9279–9282.
- [244] Y. Xu, et al., Electrochemical performance of porous carbon/tin composite anodes for sodium-ion and lithium-ion batteries, Adv. Energy Mater. 3 (1) (2013) 128–133
- [245] Z. Hongli, et al., Tin anode for sodium-ion batteries using natural wood fiber as a mechanical buffer and electrolyte reservoir, Nano Lett. 13 (7) (2013) 3093–3100.
- [246] J. Cui, E. Forssberg, Mechanical recycling of waste electric and electronic equipment: a review, J. Hazard Mater. 99 (3) (2003) 243–263.
- [247] K. Wang, et al., In-situ preparation of ultrathin graphdiyne layer decorated aluminum foil with improved cycling stability for dual-ion batteries, Carbon 142 (2019) 401-410.
- [248] W.-J. Zhang, A review of the electrochemical performance of alloy anodes for lithium-ion batteries, J. Power Sources 196 (1) (2011) 13–24.
- [249] M. Wachtler, J.O. Besenhard, M. Winter, Tin and tin-based intermetallics as new anode materials for lithium-ion cells, J. Power Sources 94 (2) (2001) 189–193.
- [250] M.R. Wagner, et al., Electrolyte decomposition reactions on tin- and graphite-based anodes are different, Electrochem. Solid State Lett. 7 (7) (2004) A201–A205
- [251] M.T. Mcdowell, et al., 25th anniversary article: understanding the lithiation of silicon and other alloying anodes for lithium-ion batteries, Adv. Mater. 25 (36) (2013) 4966–4985.
- [252] L. Ji, et al., Recent developments in nanostructured anode materials for rechargeable lithium-ion batteries, Energy Environ. Sci. 4 (8) (2011) 2682–2699. Energy Environ. Sci. 4, 2682-2699.
- [253] S. Zhang, et al., Multifunctional electrode design consisting of 3D porous separator modulated with patterned anode for high-performance dual-ion batteries, Adv. Funct. Mater. 27 (39) (2017) 1703035.
- [254] S. Wang, et al., Room temperature solid state dual-ion batteries based on gel electrolytes, J. Mater. Chem. 6 (10) (2018) 4313–4323.
- [255] G. Chen, et al., A flexible dual-ion battery based on PVDF-HFP-modified gel polymer electrolyte with excellent cycling performance and superior rate capability, Adv. Energy Mater. 8 (25) (2018) 1801219.
- [256] C. Song, et al., A novel flexible fiber-shaped dual-ion battery with high energy density based on omnidirectional porous Al wire anode, Nano Energy 60 (2019) 285–293.
- [257] X.F. Tong, et al., Carbon-coated porous aluminum foil anode for high-rate, long-term cycling stability, and high energy density dual-ion batteries, Adv. Mater. 28 (45) (2016) 9979–9985.
- [258] P.P. Qin, et al., Bubble-sheet-like interface design with an ultrastable solid electrolyte layer for high-performance dual-ion batteries, Adv. Mater. 29 (17) (2017) 1606805.
- [259] J. Lang, et al., Sodium-ion hybrid battery combining an anion-intercalation cathode with an adsorption-type Anode for enhanced rate and cycling performance, Batter. Supercaps 2 (5) (2019) 440–447.
- [260] L. Fan, et al., A nonaqueous potassium-based battery-supercapacitor hybrid device, Adv. Mater. 30 (20) (2018) 1800804.
- [261] G. Dai, et al., A dual-ion organic symmetric battery constructed from phenazine-based artificial bipolar molecules, Angew. Chem. Int. Ed. 58 (29) (2019) 9902.
- [262] Y. Liang, Z. Tao, J. Chen, Organic electrode materials for rechargeable lithium batteries, Adv. Energy Mater. 2 (7) (2012) 742–769.
- [263] Y. Zhang, et al., A novel aqueous ammonium dual-ion battery based on organic polymers, J. Mater. Chem. 7 (18) (2019) 11314–11320.
- [264] L. Yang, B. Ravdel, B.L. Lucht, Electrolyte reactions with the surface of high voltage LiNi0.5Mn1.5O4 cathodes for lithium-ion batteries, Electrochem. Solid State Lett. 13 (8) (2010) A95–A97.
- [265] G.Q. Liu, L. Wen, Y.M. Liu, Spinel LiNi0.5Mn1.5O4 and its derivatives as cathodes for high-voltage Li-ion batteries, J. Solid State Electrochem. 14 (12) (2010) 2191–2202.
- [266] A. Manthiram, K. Chemelewski, E.-S. Lee, A perspective on the high-voltage LiMn1.5Ni0.5O4 spinel cathode for lithium-ion batteries, Energy Environ. Sci. 7 (4) (2014) 1339–1350.
- [267] J.M. Lloris, C. Pérez Vicente, J.L. Tirado, Improvement of the electrochemical performance of LiCoPO4 5 V material using a novel synthesis procedure, Electrochem. Solid State Lett. 5 (10) (2002) A234–A237.
- [268] M. Nagahama, N. Hasegawa, S. Okada, High voltage performances of Li2NiPO4F cathode with dinitrile-based electrolytes, J. Electrochem. Soc. 157 (6) (2010) A748–A752.
- [269] J. Wang, et al., Superconcentrated electrolytes for a high-voltage lithium-ion battery, Nat. Commun. 7 (2016) 12032.
- [270] S. Chen, et al., High-voltage lithium-metal batteries enabled by localized high-concentration electrolytes, Adv. Mater. 30 (21) (2018), e1706102.
- [271] P. Shi, et al., A highly concentrated phosphate-based electrolyte for high-safety rechargeable lithium batteries, Chem. Commun. 54 (35) (2018) 4453–4456.
- [272] M. Watanabe, et al., Application of ionic liquids to energy storage and conversion materials and devices, Chem. Rev. 117 (10) (2017) 7190–7239.
- [273] S. Chen, et al., Progress and future prospects of high-voltage and high-safety electrolytes in advanced lithium batteries: from liquid to solid electrolytes, J. Mater. Chem. 6 (25) (2018) 11631–11663.

- [274] X. Kang, Nonaqueous liquid electrolytes for lithium-based rechargeable batteries, Chem. Rev. 104 (10) (2004) 4303–4417.
- [275] Y.-M. Song, et al., A multifunctional phosphite-containing electrolyte for 5 V-class LiNi0.5Mn1.5O4 cathodes with superior electrochemical performance, J. Mater. Chem. 2 (25) (2014) 9506–9513.
- [276] W. Märkle, et al., In situ X-ray diffraction study of different graphites in a propylene carbonate based electrolyte at very positive potentials, Electrochim. Acta 55 (17) (2010) 4964–4969.
- [277] S. Miyoshi, et al., Dual-carbon battery using high concentration LiPF 6 in dimethyl carbonate (DMC) electrolyte, J. Electrochem. Soc. 163 (7) (2016) A1206–A1213.
- [278] H. Fan, et al., Hexafluorophosphate anion intercalation into graphite electrode from sulfolane/ethylmethyl carbonate solutions, Electrochim. Acta 189 (2016) 9-15
- [279] H. Fan, L. Qi, H. Wang, Hexafluorophosphate anion intercalation into graphite electrode from methyl propionate, Solid State Ion. 300 (2017) 169–174.
- [280] Y. Huang, et al., Facilitating BF4— intercalation into graphite electrode from ethylmethyl carbonate-based solutions, ChemElectroChem 6 (2019) 2931.
- [281] H. Fan, et al., Hexafluorophosphate intercalation into graphite electrode from ethylene carbonate/ethylmethyl carbonate, Solid State Ion. 304 (2017) 107–112.
- [282] Z. Zhang, et al., Fluorinated electrolytes for 5 V lithium-ion battery chemistry, Energy Environ. Sci. 6 (6) (2013) 1806–1810.
- [283] L. Hu, Z. Zhang, K. Amine, Fluorinated electrolytes for Li-ion battery: an FEC-based electrolyte for high voltage LiNi 0.5 Mn 1.5 O 4/graphite couple, Electrochem. Commun. 35 (10) (2013) 76–79.
- [284] O. Borodin, W. Behl, T.R. Jow, Oxidative stability and initial decomposition reactions of carbonate, sulfone, and alkyl phosphate-based electrolytes, J. Phys. Chem. C 117 (17) (2013) 8661–8682.
- [285] T. Achiha, et al., Electrochemical behavior of nonflammable organo-fluorine compounds for lithium ion batteries, J. Electrochem. Soc. 156 (2009) A483–A488.
- [286] N. Noritoshi, et al., Polar effect of successive fluorination of dimethyl carbonate on physical properties, Bull. Chem. Soc. Jpn. 80 (7) (2007) 1302–1306.
- [287] A. von Cresce, K. Xu, Electrolyte additive in support of 5 V Li ion chemistry, J. Electrochem. Soc. 158 (3) (2011) A337–A342.
- [288] L. Xue, et al., Sulfone-carbonate ternary electrolyte with further increased capacity retention and burn resistance for high voltage lithium ion batteries, J. Power Sources 295 (2015) 190–196.
- [289] A. Abouimrane, I. Belharouak, K. Amine, Sulfone-based electrolytes for high-voltage Li-ion batteries, Electrochem. Commun. 11 (5) (2009) 1073–1076.
- [290] N. Shao, et al., Electrochemical windows of sulfone-based electrolytes for high-voltage Li-ion batteries, J. Phys. Chem. B 115 (42) (2011) 12120–12125.
- [291] J. Xia, J.R. Dahn, Improving sulfolane-based electrolyte for high voltage Li-ion cells with electrolyte additives, J. Power Sources 324 (2016) 704–711.
- [292] X. Wang, et al., Maintaining structural integrity of 4.5 V lithium cobalt oxide cathode with fumaronitrile as a novel electrolyte additive, J. Power Sources 338 (2017) 108–116.
- [293] C. Wang, et al., 3,3'-(Ethylenedioxy)dipropiononitrile as an electrolyte additive for 4.5 V LiNi1/3Co1/3Mn1/3O2/graphite cells, ACS Appl. Mater. Interfaces 9 (11) (2017) 9630–9639.
- [294] Y. Xu, et al., γ-butyrolactone and glutaronitrile as 5 V electrolyte additive and its electrochemical performance for LiNi0.5Mn1.5O4, J. Alloy. Comp. 698 (2017) 207–214.
- [295] A. Heckmann, et al., Towards high-performance dual-graphite batteries using highly concentrated organic electrolytes, Electrochim. Acta 260 (2018) 514–525.
- [296] S. Miyoshi, et al., Dual-carbon battery using high concentration LiPF6 in dimethyl carbonate (DMC) electrolyte, J. Electrochem. Soc. 163 (7) (2016) A1206–A1213.
- [297] C.Y. Chan, et al., Designing high-power graphite-based dual-ion batteries, Electrochim. Acta 263 (2018) 34–39.
- [298] K.V. Kravchyk, et al., High-energy-density dual-ion battery for stationary storage of electricity using concentrated potassium fluorosulfonylimide, Nat. Commun. 9 (2018) 4469.
- [299] K. Yoshida, et al., Oxidative-stability enhancement and charge transport mechanism in glyme-lithium salt equimolar complexes, J. Am. Chem. Soc. 133 (33) (2011) 13121–13129.
- [300] T.M. Pappenfus, et al., Complexes of lithium imide salts with tetraglyme and their polyelectrolyte composite materials, J. Electrochem. Soc. 151 (2) (2004) A209–A215.
- [301] T. Liu, et al., A high concentration electrolyte enables superior cycleability and rate capability for high voltage dual graphite battery, J. Power Sources 437 (2019) 226942.
- [302] K. Matsumoto, et al., Suppression of aluminum corrosion by using high concentration LiTFSI electrolyte, J. Power Sources 231 (2013) 234–238.
- [303] Y. Yamada, et al., Corrosion prevention mechanism of aluminum metal in superconcentrated electrolytes, ChemElectroChem 2 (11) (2015) 1687–1694.
- [304] S. Rothermel, M.P. Schmuelling, et al., Dual-graphite cells based on the reversible intercalation of bis(trifluoromethanesulfonyl)imide anions from an ionic liquid electrolyte, Energy Environ. Sci. 7 (10) (2014) 3412–3423.
- [305] A. Lewandowski, A. Swiderska-Mocek, Ionic liquids as electrolytes for Li-ion batteries: an overview of electrochemical studies, J. Power Sources 194 (2) (2010) 601–609.
- [306] G.B. Appetecchi, et al., Lithium insertion in graphite from ternary ionic liquid-lithium salt electrolytes: I. Electrochemical characterization of the electrolytes, J. Power Sources 192 (2) (2009) 599–605.
- [307] G.A. Elia, et al., Exceptional long-life performance of lithium-ion batteries using ionic liquid-based electrolytes, Energy Environ. Sci. 9 (10) (2016) 3210–3220.

- [308] F. Wu, et al., A safe electrolyte with counterbalance between the ionic liquid and tris(ethylene glycol)dimethyl ether for high performance lithium-sulfur batteries, Electrochim. Acta 184 (2015) 356–363.
- [309] H. Zhang, et al., Ionic liquid electrolyte with highly concentrated LiTFSI for lithium metal batteries, Electrochim. Acta 285 (2018) 78–85.
- [310] M. Nádherná, et al., Lithium bis(fluorosulfonyl)imide–PYR 14 TFSI ionic liquid electrolyte compatible with graphite, J. Power Sources 196 (18) (2011) 7700–7706.
- [311] T. Placke, et al., Dual-ion cells based on anion intercalation into graphite from ionic liquid-based electrolytes, in: Zeitschrift f
 ür Physikalische Chemie, 2012, p. 391.
- [312] M.P. Rothermel S, O. Fromm, et al., Study of the electrochemical behavior of dual-graphite cells using ionic liquid-based electrolytes, Ecs Trans. 58 (14) (2014) 15 25
- [313] T.E. Sutto, T.T. Duncan, T.C. Wong, X-ray diffraction studies of electrochemical graphite intercalation compounds of ionic liquids, Electrochim. Acta 54 (24) (2000) E648. E655.
- [314] G.H. Lane, et al., The electrochemistry of lithium in ionic liquid/organic diluent mixtures, Electrochim. Acta 55 (28) (2010) 8947–8952.
- [315] Y. Fu, et al., Vinyl ethylene carbonate as an additive to ionic liquid electrolyte for lithium ion batteries, J. Appl. Electrochem. 39 (12) (2009) 2597–2603.
- [316] I.A. Profatilova, et al., Electrochemical and thermal properties of graphite electrodes with imidazolium- and piperidinium-based ionic liquids, J. Power Sources 192 (2) (2009) 636–643.
- [317] H. Zheng, et al., Compatibility of quaternary ammonium-based ionic liquid electrolytes with electrodes in lithium ion batteries, Electrochim. Acta 52 (4) (2006) 1556–1562.
- [318] H. Ota, et al., XAFS and TOF-SIMS analysis of SEI layers on electrodes, J. Power Sources 119 (119) (2003) 567–571.
- [319] E.G. Leggesse, J.C. Jiang, Theoretical study of the reductive decomposition of ethylene sulfite: a film-forming electrolyte additive in lithium ion batteries, J. Phys. Chem. 116 (45) (2012) 11025–11033.
- [320] Y. Fang, et al., Reversible interaction of 1-butyl-1-methylpyrrolidinium cations with 5,7,12,14-pentacenetetrone from a pure ionic liquid electrolyte for dual-ion batteries, Chem. Commun. 55 (57) (2019) 8333–8336.
- [321] N.G. Connelly, W.E. Geiger, Chemical redox agents for organometallic chemistry, Chem. Rev. 96 (2) (1996) 877–910.
- [322] L. Cosimbescu, et al., Anion-tunable properties and electrochemical performance of functionalized ferrocene compounds, Sci. Rep. 5 (2015) 14117.
- [323] C. Yang, et al., 4.0 V aqueous Li-ion batteries, Joule 1 (1) (2017) 122-132.
- [324] C. Yang, et al., Aqueous Li-ion battery enabled by halogen conversion-intercalation chemistry in graphite, Nature 569 (7755) (2019) 245–250.
- [325] S. Yang, et al., Lithium metal extraction from seawater, Joule 2 (9) (2018) 1648–1651.
- [326] R. Schmuch, et al., Performance and cost of materials for lithium-based rechargeable automotive batteries, Nat. Energy 3 (4) (2018) 267–278.
- [327] J. Xu, et al., Recent progress in graphite intercalation compounds for rechargeable metal (Li, Na, K, Al)-Ion batteries, Adv. Sci. 4 (10) (2017) 1700146.
- [328] Q. Zhao, et al., Oxocarbon salts for fast rechargeable batteries, Angew. Chem. 128 (40) (2016) 12716–12720.
- [329] Y. Xu, et al., Highly nitrogen doped carbon nanofibers with superior rate capability and cyclability for potassium ion batteries, Nat. Commun. 9 (1) (2018) 1720.
- [330] Y.H. Zhu, et al., High-energy-density flexible potassium-ion battery based oatterned electrodes, Joule 2 (4) (2018) 736–746.
- [331] N. Xiao, W.D. McCulloch, Y. Wu, Reversible dendrite-free potassium plating and stripping electrochemistry for potassium secondary batteries, J. Am. Chem. Soc. 139 (28) (2017) 9475–9478.
- [332] B. Ji, et al., A dual-carbon battery based on potassium-ion electrolyte, Adv. Energy Mater. 7 (20) (2017) 1700920.
- [333] W. Zuo, et al., Bismuth oxide: a versatile high-capacity electrode material for rechargeable aqueous metal-ion batteries, Energy Environ. Sci. 9 (9) (2016) 2881–2891.

- [334] H. Pan, et al., Sodium storage and transport properties in layered Na2Ti3O7 for room-temperature sodium-ion batteries, Adv. Energy Mater. 3 (9) (2013) 1186–1194.
- [335] F. Xie, et al., Na2Ti3O7@N-Doped carbon hollow spheres for sodium-ion batteries with excellent rate performance, Adv. Mater. 29 (24) (2017) 1700989.
- [336] S. Anwer, et al., Nature-inspired Na2Ti3O7 nanosheets-formed three-dimensional microflowers architecture as a high-performance anode material for rechargeable sodium-ion batteries, ACS Appl. Mater. Interfaces 9 (13) (2017) 11669–11677.
- [337] R. Ma, et al., Offset initial sodium loss to improve coulombic efficiency and stability of sodium dual-ion batteries, ACS Appl. Mater. Interfaces 10 (18) (2018) 15751–15759.
- [338] L. Fan, et al., Potassium-based dual ion battery with dual-graphite electrode, Small 13 (30) (2017) 1701011.
- [339] K. Beltrop, et al., Alternative electrochemical energy storage: potassium-based dual-graphite batteries, Energy Environ. Sci. 10 (10) (2017) 2090–2094.
- [340] Q. Wang, et al., Reaction and capacity-fading mechanisms of tin nanoparticles in potassium-ion batteries, J. Phys. Chem. C 121 (23) (2017) 12652–12657.
- [341] S.W.F.Z.Y. Tang, A novel calcium-ion battery based on dual-carbon configuration with high working voltage and long cycling life, Adv. Sci. 5 (8) (2018) 1701082.
- [342] N. Kuperman, et al., High performance Prussian Blue cathode for nonaqueous Caion intercalation battery, J. Power Sources 342 (2017) 414–418.
- [343] A. Ponrouch, et al., Towards a calcium-based rechargeable battery, Nat. Mater. 15 (2) (2015) 169–172.
- [344] S.K. Das, S. Mahapatra, H. Lahan, Aluminium-ion batteries: developments and challenges, J. Mater. Chem. 5 (14) (2017) 6347–6367.
- [345] T.K.A. Hoang, et al., Corrosion chemistry and protection of zinc & zinc alloys by polymer-containing materials for potential use in rechargeable aqueous batteries, RSC Adv. 5 (52) (2015) 41677–41691.
- [346] K. Wippermann, et al., The inhibition of zinc corrosion by bisaminotriazole and other triazole derivatives, Corros. Sci. 32 (2) (1991) 205–230.
- [347] S. Wang, et al., A novel aluminum-ion battery: Al/AlCl3-[EMIm]Cl/Ni3S2@ Graphene, Adv. Energy Mater. 6 (13) (2016) 1600137.
- [348] Q. Li, N.J. Bjerrum, Aluminum as anode for energy storage and conversion: a review, J. Power Sources 110 (1) (2002) 1–10.
- [349] G. Torsi, G. Mamantov, Acidbase properties of the systems aluminum chloridemetal chloride (metal = lithium, sodium, potassium, cesium), Inorg. Chem. 11 (6) (1972), 1439-1439.
- [350] K.V. Kravchyk, et al., Efficient aluminum chloride–natural graphite battery, Chem. Mater. 29 (10) (2017) 4484–4492.
- [351] X. Yu, et al., Graphene nanoribbons on highly porous 3D graphene for highcapacity and ultrastable Al-ion batteries. Adv. Mater. 29 (4) (2017) 1604118.
- [352] J. Zhu, et al., Defect-engineered graphene for high-energy- and high-power-density supercapacitor devices, Adv. Mater. 28 (33) (2016) 7185–7192.
- [353] R. Narayanan, et al., Modulation of the electrostatic and quantum capacitances of few layered graphenes through plasma processing, Nano Lett. 15 (5) (2015) 3067–3072.
- [354] E. Zhang, et al., Unzipped carbon nanotubes for aluminum battery, Energy Storage Mater. 23 (2019) 72–78.
- [355] Z. Liu, et al., Carbon nanoscrolls for aluminum battery, ACS Nano 12 (8) (2018) 8456–8466.
- [356] Q. Zhang, et al., Low-temperature synthesis of edge-rich graphene paper for highperformance aluminum batteries, Energy Storage Mater. 15 (2018) 361–367.
- [357] Y. Wu, et al., 3D graphitic foams derived from chloroaluminate anion intercalation for ultrafast aluminum-ion battery, Adv. Mater. 28 (41) (2016) 9218–9222.
- [358] H. Chen, et al., Ultrafast all-climate aluminum-graphene battery with quartermillion cycle life, Sci. Adv. 3 (12) (2017) eaao7233.
- [359] G. Wang, et al., Polarity-switchable symmetric graphite batteries with high energy and high power densities, Adv. Mater. 30 (39) (2018) 1802949.
- [360] B. Heidrich, et al., Unravelling charge/discharge and capacity fading mechanisms in dual-graphite battery cells using an electron inventory model, Energy Storage Mater. 21 (2019) 414-426.
- [361] D. Lisbona, T. Snee, A review of hazards associated with primary lithium and lithium-ion batteries, Process Saf. Environ. Prot. 89 (6) (2011) 434–442.
- [362] L. Zhang, et al., Flame-retardant electrolyte solution for dual-ion batteries, ACS Appl. Energy Mater. 2 (2) (2019) 1363–1370.